DEVELOPMENT AND APPLICATION OF TOOLS FOR THE CHARACTERIZATION OF THE OPTOGENETIC STIMULATION OF THE COCHLEA

Dissertation

for the award of the degree
"Doctor of Philosophy, PhD"
Division of Mathematics and Natural Sciences
of the Georg-August-Universität Göttingen

within the doctoral program
"International Max Planck Research School for Neuroscience"
of the Georg-August University School of Science (GAUSS)

submitted by
Carlos Javier Duque Afonso

born in
Santa Cruz de Tenerife, Spain

Göttingen 2019

Thesis Committee

Prof. Dr. Tobias Moser
Institute for Auditory Neuroscience
University Medical Center Göttingen

Prof. Dr. Alexander Flügel
Institut für Neuroimmunologie und Multiple-Sklerose-Forschung
University Medical Center Göttingen

Dr. Katrin Willig
Nanoscale Microscopy and Molecular Physiology of the Brain group
Max Planck Institute of Experimental Medicine, Göttingen

Members of the Examination Board

Referee: ***Dr. Camin Dean***
Trans-synaptic Signaling group
European Neuroscience Institute, Göttingen

2nd Referee: ***Prof. Dr. Frauke Alves***
Translational Molecular Imaging group
Max Planck Institute of Experimental Medicine, Göttingen

3rd referee: ***Prof. Dr. Martin Göpfert***
Dept. of Cellular Neurobiology
Schwann-Schleiden Research Centre, Göttingen

Date of oral examination: ***Thursday, 29th August 2019***

Declaration

Herewith I declare, that I prepared the PhD Thesis " Development and application of tools for the characterization of the optogenetic stimulation of the cochlea" on my own and with no other sources and aids than quoted.

Carlos Javier Duque Afonso

Göttingen, 25.07.2019

TABLE OF CONTENT

ABSTRACT

Five per cent of the world population suffers nowadays from some kind of disabling hearing impairment, and 90% out of them is due to a defective functioning of the first step in the transduction of the soundwave into a neural code: the organ of Corti and the spiral ganglion neurons. The development of the most successful neuroprosthetic device, the cochlear implant, has allowed patients to accomplish fair speech comprehension, but has failed in providing speech comprehension in noisy environments, good frequency discrimination and music and prosody appreciation. The most prominent limitation of the current electrical cochlear implant is the lateral spread of the electrical stimulus in the ionic medium of the inner ear, that reduces the number of independent stimulation channels. One promising, yet experimental, alternative is the use of light and optogenetics. Since light can be better focused than the electrical pulses, the potential crosstalk between channels is smaller and the number of independent ones is potentially bigger. However, in order to be able to stimulate the auditory neurons with light, they have to express a light sensitive ionic channel, known as opsins, delivered by viral vectors injected in the inner ear. Furthermore, an optimal optogenetic stimulation of the cochlea would need very fast and sensitive channels, that allow the submilisecond precision needed to convey auditory information to the central nervous system. In the lab we have shown the feasibility of using this modality of stimulation to activate the auditory pathway. However, some questions remain to be answered, like how is the 3D illumination profile of the light sources that we use or could use in the future or how is the precise distribution of the expression levels along the cochlea. Thus, in this thesis, I will present the effort to develop and apply a series of tools to characterize the optogenetic stimulation of the cochlea. We have developed a Monte-Carlo simulation to estimate the irradiance profile of various sources (including the optical fibers used in vivo experiments, a proof of concept of an optimal one or the μLEDs that the first optical cochlear implant might carry). In addition, I have optimized a tissue clearing protocol, cDISCO, and developed a computational workflow to study the 3D distribution of GFP (as a proxy of the transduction efficiency) as a function of the tonotopic position. We expect that these tools help us to understand better our stimulation paradigm and to plan future proof of concepts.

1. GENERAL INTRODUCTION

1.1. THE AUDITORY SYSTEM

1.1.1. COMPONENTS

Sounds are defined as audible variations in the air pressure. They originate from the consecutive compression (increase of air molecule density) and rarefaction (decrease of air molecule density) of the air, originated by a moving mass. Sound properties are sensed and interpreted as percepts: frequency (number of consecutive compressions and rarefactions per second) is perceived as pitch, intensity (difference of pressure between compress and rarefacted blocks) is perceived as loudness. Thus, humans are only to perceive sounds of 20 Hz to 20 kHz, with intensities up to about a 10_6 times greater than the intensity of the softest sound that can be heard, giving a dynamic range between 0-120dB (Bear et al., 2015).

These air-borne mechanical waves propagated through air at an approximate speed of 340 m/s are captured by the auricle or *pinna* (latin for "wing"), which is the cartilaginous skin-covered, visible part of the outer ear. The auricle changes the frequency spectrum of the sound and directs it through the ear canal to the tympanic membrane, which is part of the middle ear. The middle ear is a cavity connected to the pharynx by the Eustachian tube and hosts three ossicles: the malleus, incus and stapes. The malleus is attached to the tympanic membrane and the footplate of the stapes is connected with the oval window of the cochlea in the inner ear. The ossicle chain can be stiffened by the stapedius and tensor muscles of the middle ear. The air-borne vibrations push and pull upon the tympanic membrane (also known as eardrum), trigger a complex series of movement in the ossicles, ending with the inward and outward movement of the oval window by the stapes. The cochlea, is the snail shaped hearing organ of the inner ear. It has three compartments or *scalae*: scala media, vestibuli and tympani. The two latter are interconnected in the apex by the helicotrema and filled by perilymph, a virtually non-compressive fluid with ionic composition comparable to that of the cerebrospinal fluid. The scala media is filled with endolymph, houses the sensory epithelium (known as the organ of Corti) and it is separated by the basilar and Reissner´s membrane from the scala tympani and vestibuli, respectively. The footplate of the stapes acts as a piston and moves the liquid in the scala vestibuli, increases the pressure in the scala tympani and finally ends up with the outward bending of the round window (Kandel et al., 2012). Thus, the middle ear acts as an impedance transformer, amplifying and matching the sound energy originated in a low impedance medium as the air, to the high impedance of the cochlear fluids (Pickles, 2015).

The organ of Corti rests on the basilar membrane and harbors the sensory cells of the cochlea: the inner and outer hair cells. These two epithelial cells differ tremendously in their functions and are distributed in one and three rows, respectively. Whereas the inner hair cells are the genuine sensory cells, the outer hair cells, though its electromotility, have the role of an active amplifier (Fettiplace, 2017). When the sound wave, moves the perilymphatic liquid, it causes a relative movement of basilar membrane and the tectorial membrane, to which the tallest stereocilia of the outer hair cells are attached (Kimura, 1966). The resulting deflection of the stereocilia stretches the filamentous tip links triggering the opening of the mechanotransducer channels (Pickles, 2015). While not directly connected to the tectorial membrane, the stereocilia of the inner hair cells are thought be deflected by the radial flow in the subtectorial space caused (Guinan, 2012). In either case of stereociliar deflection, the influx of potassium through the mechanotransducer channels causes graded receptor potential (i.e. a graded change of the cell potential) across the whole cell. At the level of the active zones (the presynaptic side of the IHC-SGN synapse), it opens $Ca_v1.3$ L-type channels, triggering the Ca^{2+}-dependent release of glutamate-filled synaptic vesicles. Glutamate binds the postsynaptic AMPA receptors expressed in the SGNs, triggering a depolarizing current linearly dependent on the amount of glutamate release. The generated action potentials travel through the cochlear portion of the XIII cranial nerve until the cochlear nucleus and where the signal is relayed to different circuits of the auditory pathway, until signal will is finally decoded in the auditory cortex, triggering the percept of the sound (Pickles, 2015).

This inner hair cell synapse possess the ability of being indefatigable (meaning that it can sustain tonic release with little depression) and of displaying a submillisecond temporal precision and phase constancy, allowing a precise and accurate phase locking of the neuron firing (Fettiplace, 2017). Additionally, it possess a unique presynaptic machinery, only partially shared by some other cells in the retina (photorreceptors and bipolar cells) and in the pineal gland (Reuss, 2011), which also feature synaptic ribbons. The synaptic ribbon received its name from its plate-like electrodense ultrastructural appearance in photoreceptors, initially describes in the 60s. In inner hair cells, it takes an ovoid shape surrounded by a halo of vesicles (Wichmann and Moser, 2015). Although its function is not completely understood, it seems that it is involved in vesicle replenishment and Ca^{2+} channel regulation at the active zone (Jean et al., 2018).

1.1.2. TONOTOPY IN THE INNER EAR

Pure tones are rarely found in nature. Instead, common sounds are complex, which means that they are a combination of n-number of single sinusoidal waves with different energies. The early investigations carried by Georg von Bekesy in the 1960s (Von Bekesy, 1960) revealed an elegant phenomenon through which the basilar membrane can perform a passive mechanical spectrum analyzer. It separates the different frequency components along its length (~6 mm in mouse, ~35mm in humans) and places the point of maximal deformation for a concrete frequency in a particular position, proportional to the energy of that given frequency component. The constantly instant Fourier analysis of our sound space carried by the basilar membrane is achieved by its different mechanical properties (Mann and Kelley, 2011). In the base is narrow and thick, whereas in the apex is wider and thinner (Burda et al., 1988). Stiffness also change with position being stiffer in the base and more flexible in the apex. Furthermore, it is constructed by fibrillar collagen fibers and proteoglycans, and with a radially (medial-to-lateral) changing structure that give name to its two parts: part arcuata (meshwork of collagen beneath the pillar cells) and pars pectinata (radially oriented fibers in a bilayered structure beneath the outer hair cells and Claudius' and Hensen's cells) (Tsuprun and Santi, 1999).

The arrangement of different frequencies sensitivities along the basilar membrane represents a tonotopic map (also named tonotopic axis throughout this dissertation) and this map is preserved along the whole auditory pathway. The relation of frequency and place along the tonotopic axis is distributed logarithmically and it is generally described in most mammals by the so-called Greenwood´s function (Greenwood, 1961, 1990, 1991):

$$f = A(10^{\alpha x} - k)$$

Where f, is frequency; A is the frequency-offset; α is the gradient or slope of the map in its high frequency region; x is the normalized distance from the apex; k is a constant, or warp factor, that introduces curvature to fit the low frequency data (LePage, 2003; Müller et al., 2005).

The mechanical properties of the basilar membrane are not the only parameter that shows a tonotopic gradient. Differential expression of ion channels, Ca^{2+} binding proteins and other protein result in graded physiological and morphological features of hair cells and spiral ganglion neurons (SGN), allowing them to be specialized in signaling and encoding different and specific aspects of the sound´s properties (Fritzsch et al., 2015; Mann and Kelley, 2011).

Sound encoding strategies differ for low and high frequency stimuli. The membrane time constant of the inner hair cell produce a low pass filter of the incoming stimulus. The receptor potential of the inner hair cells have a DC (continuous) and an AC (periodic) component. Since the AC component is inversely proportional to the frequency, when the AC components is predominant over the DC, that is, for low frequencies, the receptor potential follows the sinusoidal waveform of the basilar membrane velocity. Above 1kHz, the DC component predominate and the receptor potential follows just the amplitude of the stimulus (Russell and Sellick, 1983). The decline in the AC/DC components ratio correlates with the degree of phase-locking of the SGN. For low frequency, SGNs fire phase-locked to the individual cycles of the stimulating waveform in a probabilistic manner. Above 1 kHz the phase locking is progressively lost and the neuron can fire randomly at any phase of the waveform, encoding the frequency of the sound in the tonotopic location and the timing of its action potential (Pickles, 2015).

The intensity of the sound is encoded both at the SGN level and at the population level. At the SGN level, the firing rate increase, triggered by the higher amplitude of the basilar membrane vibration and underlying stronger depolarization of the IHC. At the population level, the stronger basilar membrane vibration activates a larger number of IHCs, recruiting more SGNs (Bear et al., 2015). Moreover, the spontaneous firing rate (in the absence of sound), the sound threshold and the dynamic range differ among SGNs even if their characteristic frequency suggests that they receive presynaptic input from the same IHC. Interestingly, the active zones of a given IHC differ in the voltage-dependence and maximal amplitude of Ca^{2+} influx and of glutamate release. This suggests IHC decompose sound-born cellular signals, i.e. the receptor potential, into different neural codes via functionally distinct active zones (Frank et al., 2009; Ohn et al., 2016).

1.2. HEARING LOSS AND THE COCHLEAR IMPLANT

1.2.1. HEARING LOSS

Hearing loss typically is defined as increases in the hearing threshold to sinusoids between 0.5 to 4 kHz above 20-34 dB (mild hearing loss) until 95 or more dB (complete loss), considering disabling losses above 35 dB increment (Wilson et al., 2017). The WHO has estimated that 6.1%

of the world´s population suffer from disabling hearing loss (432 million of adults and 34 million of children) and that by 2050, this quantity will increase to one in every ten (around 900 million people)(WHO, 2019). Congenital hearing loss is most often caused by genetic factors (including syndromic and non syndromic forms), craniofacial abnormalities or congenital infections. In most developed countries, with universal neonatal hearing screening, the estimated prevalence are 1.33 per 1000 live births, 2.83 per 1000 children in primary school age and 3.5 per 1000 adolescent (Korver et al., 2017). Hearing loss is the fourth leading cause of years lived with disability, since it does not only affect the ability of perceiving sounds but also can affect at different levels both in early and later developmental stages. In children, it hampers or at least delays the acquisition of language and affects the cognitive development. In adults, it often has psychological and social consequences, affecting one's self-esteem, leading to social isolation, decrease their job opportunities and even higher risk of developing dementia (Wilson et al., 2017).

The etiology of hearing loss is vast and diverse, and can be differentiated as genetic and acquired forms. Genetic mutations can either affect the production and maintenance of endolymph (e.g. GJB2, DFNB73, CLDN14) or the normal functioning of the mechanosensation (e.g. KCNQ4, ESPN, TRIOBP, OTOF). Acquired congenital hearing loss can be caused by maternal infections transfer to the newborn either before or during birth (e.g. Zika virus, CMV, Rubella, Toxoplasma gondii). Other acquired reasons include otitis media, exposure to damaging loud sounds, trauma, measles and mumps, ototoxic effect of certain drugs, solvents and industrial chemicals (Korver et al., 2017; Wilson et al., 2017).

There are two types of peripheral hearing loss: conductive and sensorineural. Conductive hearing loss affects primarily the outer and middle ear. It can be diagnosed by audiometric differences for auditory stimulus originated in the air (standard sound) and those conducted through bone (vibrations in the scalp that can elicit less efficiently stimulation of the cochlea). The main forms of conductive hearing loss can be classified as: immobilization of the tympanic membrane or the ossicles by the presence of fluid or scar tissue from an middle ear infection; occlusion of the ear canal by wax or foreign objects; ossicular interruption with intact tympanometry; loss or perforation of tympanic membrane; otosclerosis (arthritic ossification of the and underlying deprivation of free movement of the ossicle chain); atelectasis (collapse of the tympanum into the middle ear; the immobilization of the tympanic membrane or the ossicles by the presence of fluid or scar tissue from an middle ear infection (Eggermont, 2017; Kandel et al., 2012; Purves et al., 2004). It can be successfully treated by microsurgery of the ear often including reconstruction of the ossicles or use of middle ear prosthesis, as well as by

conventional or bone-anchored hearing aids. (Kandel et al., 2012; Korver et al., 2017; Purves et al., 2004)

The sensorineural hearing loss finds its origin in the alteration of the normal functioning of the cells in charge of the transduction and encoding of the sound stimulus: the hair cells and the SGNs. Mid-to-severe sensorineural hearing loss is normally treated with conventional hearing aids. For higher threshold shift, the cochlear implant typically provides a more efficient hearing restoration and allows patient meaningful speech comprehension (Korver et al., 2017). It is worth noting that the cochlear implant has become the most successful neuroprosthetic device – in 2008, approximately 172000 patients were using it worldwide (Peters et al., 2010), in 2013, 300000 (O'Donoghue, 2013) and nowadays it is estimated to be around 700000 users. In patients with relatively maintained low frequency hearing, the mixed or electroacoustic implants are the choice (Korver et al., 2017).

1.2.2. THE COCHLEAR IMPLANT

Alessandro Volta, carried one of the first attempts to electrically stimulate the cochlea, by inserting two cables connected to his recently developed batteries, which were providing 50V. He defined the experience as dangerous and disagreeable, since he experienced a shock in the brain after the sensation of a sound similar to that of a crunching or effervescent boiling paste (Volta, 1800). Despite there were other attempts, it can be considered that the first true CI was implanted by William House and John Doyle in California in winter of 1961. After several years of improvements and patient tests, with the advent of the place theory by Von Bekesy (Von Bekesy, 1960), the multichannel electrode array from which the current CI ascent, was designed by Simmons and White and implanted by Michelson´s and, some years later, Clark´s team. This design exploited the tonotopic distribution of the cochlea, permitting simultaneous local stimuli of different intensities performed by the electrode arrays of the cochlear implant. After this, the venue for its commercialization was opened (Mudry and Mills, 2013). All in all, it is important to highlight that the first clinically useful devices were developed relatively in parallel between the 60s and 80s by several teams around the world, including Michelson and Merzenich, Simmons and White, and Eddington in the USA, Chouard in France, Peeters and Offeciers in Belgium; Burian and the Hochmairs in Austria and Clark in Australia (Wilson and Dorman, 2008)

Despite that the fundamental design of the implants have stayed relatively constant, the perceptual performance has being improved because of the advances in the speech processor electronics and algorithms. However, the cochlear implant seem to reach asymptotically to its maximum performance with the current electrode technology and its associated current spread (O'Leary et al., 2009), limiting the maximum pitch discrimination possible (now 3 times lower than normal hearing persons (Kang et al., 2009). Experiments in the end of the 90s, revealed that the maximum number of perceptual channels was eight, regardless the number of electrode contacts (Dorman et al., 1998). In normal hearing subjects it was determined that 20 perceptual channels would be needed to understand speech in noisy environments and that a minimum of 32 perceptual channels are needed for music appreciation. Pitch is fundamental to define melody and harmony in music, represent prosody in speech by its contour, clarify meaning of words in tonal languages (such as Mandarin or Cantonese) and help to differentiate simultaneous sounds in complex acoustic scenarios (Oxenham, 2012). Being aware of it, the current goal of the cochlear implant professionals is to increase the number of perceptual channels of the implant (O'Leary et al., 2009). In addition, up to 4kHz, normal hearing people are able to use the temporal cues to perceive pitch (Oxenham, 2012). In cochlear implant user, this is limited to 300 – 800 Hz (Duran et al., 2012; Zeng, 2002). Poor intensity discrimination is another caveat that cochlear implant user have to face and it is likely contributing to the limited speech comprehension in noisy environments (Jeschke and Moser, 2015). Although it seems that this could be alleviated by bilateral implantation, improving together hearing, sound localization and quality-of-life scores, there is a lot of room for improvement.

Some of the strategies to bring the next generation of the cochlear implants include 1) decreasing the gap size between the electrodes and the neural elements, 2) controlling the number and configuration of the electrodes at a given time, 3) reducing the volume of cochlear fluid available to conduct the electrode currents (O'Leary et al., 2009) and 4) the use of novel stimulation strategies that can be better focused, such as light (Jeschke and Moser, 2015).

1.3. OPTOGENETICS AND HEARING RESTORATION

Light has been successfully used for stimulating the auditory periphery, however, using two very well separated strategies: infrared stimulation and optogenetics (Jeschke and Moser, 2015). Infrared stimulation has been used by the laboratory of Claus Peter Richter to stimulate the auditory nerve of different species and depicts certain place-selectivity. However, given

that it mechanism of action is not very well elucidate and could include heating waves or an optoacoustic effect, its usability in a clinical setting is still a matter of debate (Richter and Tan, 2014).

Karl Deisseroth, one of the pioneers of modern optogenetics, define Optogenetics as "the combination of genetic and optical methods to evoke or inhibit well-defined events in specific cells of living tissue and behaving animals" (Deisseroth, 2015). Although some place the start of optogenetics, as we know nowadays, back in 2002 with the optical control of neurons by the expression of a light-activated channel chARGe (Adamantidis et al., 2015; Zemelman et al., 2002), it can be considered that the description of the channelrhodopsin (ChR) 1 and 2 (Nagel et al., 2002, 2003) and, then, the Boyden et al., 2005 paper set the kick off of this revolutionary approach.

As presented in Deisseroth and Hegemann, 2017, the first descriptions of phototaxia in the algae Chlamydomonas spp. by Andrei Sergeyevich took place in 1876. More than hundred years later, ChR 1 and 2 were found to be the responsible light-gated ion channel for this type of behavior (Braun and Hegemann, 1999; Foster et al., 1984; Nagel et al., 2002, 2003). In between, and without being aware what it would mean to the future of neuroscience, other light-gated channels were described in their respective system: Bacteriorhodopsins (Oesterhelt and Stoeckenius, 1971, 1973) and halorhodopsins (Matsuno-Yagi and Mukohata, 1977). Thus, the rhodopsin family of interest for optogenetics can be split in three branches: 1) Bacteriorhodopsins, 2) Halorhodopsin and 3) Channelrhodopsin. The two first are inhibitory (hyperpolarize) since they pump protons out of the cells or chloride into the cell, respectively. The channelrhodopsin family allows the flux of cations, having generally a depolarizing, and thus, excitatory, effect. Nowadays, all of the branches have been enriched with naturally-occurring and lab-engineered novel variants, providing researchers with a plethora of channels suitable for each specific application with different light sensitivities, different ionic permeabilities and different kinetics (Deisseroth, 2015). In addition, under the umbrella of term optogenetics, we find not only the design and application of the opsin but also of the targeting methods to bring the opsin-expression to the desired cell population and of the light delivery and control devices (Deisseroth, 2015).

The application of optogenetics in the auditory system is quite demanding. It needs an opsin that offers fast kinetics and high light sensitivity (for a low power consumption of the implant). It needs a light source that can be miniaturized and that provide certain degree spatial confinement (for a better frequency discrimination). Finally, it needs a gene delivery system

that probe to be safe and efficient and that provides certain degree of expression variability within one specific tonotopic region (for intensity coding) (Jeschke and Moser, 2015).

1.3.1. OPSINS

We and others have been exploring the suitability of the different opsins available in the various animal models.

In 2014 (Hernandez et al., 2014), cochlear optogenetics kicked off with ChR2 in transgenic mice and rats and the Ca^{2+} permeable, ChR2 mutant, CatCh (Kleinlogel et al., 2011)in mouse, prenatally delivered by transuterine otocyst injections of AAV2/6 viruses. Among other findings, we showed for the first time the possibility of using light to stimulate the peripheral auditory system, which was transmitted along the auditory pathway up to the inferior colliculus. Using the tonotopic organization of the inferior colliculus as a read-out, (Hernandez et al., 2014) showed a promising increase in frequency resolution, when compared to electric stimulation. Furthermore, it was shown that light-evoked activity of SGNs was achievable in deaf mice, displaying its translational potential. However, the kinetics of the opsins used at these early stages were far away from supporting the high temporal requirements of the auditory system. The optically-evoked Auditory Brainstem Response (oABR) is an electrophysiological measurement of far-field synchronized neural population responses along the auditory pathway. For both opsins, it showed a decreased synchronized activity above 20 Hz, being detectable up to 70 Hz. On the other hand, single Catch-expressing SGNs were shown to follow up to at least 60 Hz.

We observed an increased synchronized activity, up to 200 Hz, of Catch-expressing neurons four years later in the cochlea of the Mongolian gerbil (Wrobel et al., 2018). In this occasion, we decided to use gerbils instead of mouse and rats, for having a hearing range more similar to that of humans. We also took a step forward and were able to record light-evoked activity in the auditory cortex, following light stimulation through the round window. Furthermore, we showed how the optogenetic stimulation of SGNs could be used by the gerbils to perform an avoidance behavior. Gerbils, chronically implanted with a single-channel, fiber based optical CI displayed an excellent learning in a shuttlebox paradigm of negative reinforcement, that could be even transferred to acoustic stimulation. At this point, cochlear optogenetics was not only able to activate auditory neurons with light, but it was providing a percept that the animal could use for learning. We also used Monte Carlo simulation to study the 3D light spread in the

gerbil cochlea and modelled how an ideal emitter, of reduced size and low numerical aperture, when optimally positioned, could provide enough light irradiance to presumably activate the neurons in the spiral ganglion with very low power requirement and extremely narrow lateral spread of the stimulation. We continued our investigations with this model to investigate the aspect of spectral resolution using a multi-site stimulation approach, to coarsely mimic the future multi-channel optical cochlear implant (Dieter et al., 2019). Thus, using an electrode array to tonotopically study the elicited activity in the inferior colliculus, we found a more confined spread of excitation when compared to both electrical monopolar and bipolar stimulation, but worse than sound stimulation, as expected. The improved spectral resolution was seen in the three positions used for light stimulation. In this occasion, we also used Monte Carlo simulation to estimate where the fibers were placed, and how different positions of the fibers could drastically change the stimulation pattern. Thus, we could provide support for future translation of cochlear optogenetics, given its better spectral resolution, which we hope will boost the ability of patients to perceive speech, music and prosody.

Given that amount of scattering, at least for scales smaller than the wavelength of the incident light (Rayleigh scattering, further explained in the introduction of chapter I), is inversely proportional to the forth power of the incident wavelength, red-shifted light would be less scattered in tissue resulting in deeper penetration and potential lower power requirements (Welch and van Gemert, 2011). In addition, it is less phototoxic than blue light (Douthwright and Sluder, 2017). Thus, we investigated the possibility of using a red-shifted opsin, fast-Chrimson (Mager et al., 2017). The oABR show synchronized activity up to 200 Hz, and individual putative neurons could follow at least 250 Hz (similar to the physiological steady state firing rate of the SGN). However, the slow kinetics and resulting limited spike probability and temporal precision might make it not totally suitable to encode high frequency stimulations, although it might be recovered at the auditory nerve population level.

We then explored and characterized Chronos (Keppeler et al., 2018), the fastest blue-shift opsin to date (Klapoetke et al., 2014). We found that at 36°C, its *in vitro* kinetics were in the submilisecond range (activation constant, τ_{on}: 0.58 ms, deactivation constant, τ_{off} =0.76 ms), where exceeding 3.9 fold to those of ChR2(τ_{on} = *2.3 ms,* τ_{off} = 3 ms, comparable to kinetics of Chronos at 22°C) and allow a bandwidth of several hundred Hz, with a cutoff value of 150 Hz at this temperature. We further showed that our gene delivery strategy was improved incorporating a new AAV serotype (PHP.B) and a membrane targeting sequence (ES/TS) and achieve high expression rates in the membrane of mouse SGNs. We found the synchronized SGN activity as reflected by the P1-N1 peak in the oABR to be sustained up to 1 kHz with Chronos-ES/TS , which is the highest rate observed among the various ChRs we have tested in

the auditory system. At the level of single putative SGN, it was shown that the neurons could follow with high, yet variable, temporal precision, light pulses up to rates of several hundred of Hz, reaching occasionally 1 kHz. However, the spike precision and probability were decreasing beyond 100 Hz, which probably compensated at the population level. Furthermore, the output dynamic range was above 10dB, outperforming the standard dynamic range of electrical cochlear implants (Zeng et al., 2008). Overall, it seemed that the combination of the potent AAV-PHP.B vector with the ultrafast Chronos-ES/TS it is a promising candidate and will probably nurture more investigations. The team of Daniel Lee also demonstrated the ability of stimulating the auditory periphery with this fast blue-shifted opsin (Duarte et al., 2018). Chronos-EGFP under the CMV promoter was delivered using an Anc80L65 virus, a predicted AAV ancestor, at p4, through the round windows. They were able to elicit optical ABR and light-evoked activity in the inferior colliculus (although synchronized only up to 28 pulses/s), demonstrating an activation of the auditory pathway. However, the fact that some hair cells in the organ of Corti, that were not quantified, also were GFP positive rise the possibility that the auditory response might have been mediated by the light-evoked release of glutamate from the inner hair cells and subsequent spiral ganglion activation.

Some opsins remains to be fully tested in the SGN, like very fast-Chrimson (Mager et al., 2017) or ChroME (Mardinly et al., 2018).The Chrimson mutant K176R/Y261F/S267M, known as very fast-Chrimson, provides faster deactivation kinetics than the tested mutant (3.2 vs 1.6 ms, at 34° C, 5.7 vs 2.7 ms at room temperature), although shows a reduction in the current density. The Chronos mutant, ST-Chronos-M140E, also known as ChroME, although with relative slower off kinetics (3 ms vs 1.7 ms, likely at room temperature), provides a bigger current amplitude than ST-Chronos, which could be beneficial for the power consumption of the future implants. Furthermore, given the ongoing growing of the new discoveries and developments in the field of optogenetics, it would not be unexpected that novel opsins will outperform even the currently most promising ones.

1.3.2. LIGHT SOURCES

Most of our in vivo experiments relay on light delivery through a laser-coupled optical fibers. Although for our current experimental work, it is good enough, for future multiple channel miniaturized illumination, the design has to be different. Thus, we can separate future designs for cochlear implant as passive or active implants (Jeschke and Moser, 2015).

The passive implants transport the light from an external source to the stimulation site, e.g. using miniaturized optical fibers or waveguide arrays. In case of a multichannel optical cochlear implant the need of addressing individually each of the fibers is a must. Different strategies include, but are not limited to, digital μ-mirror arrays coupled to μ-lense array, galvanometric mirrors with special lenses or tapered optical fiber with optical windows milled along the its length addressable by the modification of the angle of coupling at the opposite end. However, the current technology would require to fix the animal to an optical bench to avoid misalignment and the underlying crosstalk of channels, apart from the limited implantability of the current bulky designs and the high-power requirement to correct for the coupling losses (Pisanello et al., 2016)

The active implant refers to those devices that can generate light directly inside the cochlea, such as the recently developed multi μLED array based cochlear implant (Goßler et al., 2014; Klein et al., 2018). Given that the emission profile of the LED is Lambertian, the light spread is bigger than optical fiber-based solution, and if it is too far from the ganglion, the promised bigger perceptual frequency resolution could be missed. Thus, sources with better beam-profile are desired. Using μ-lenses in combination with optical concentrators and reflectors shows promising improvement of the emission profile (Bi et al., 2016; Klein et al., 2019). However, their incorporation to the optical cochlear implant would increase its bulkiness (e.g. the height of the μLED Cree2227 would become 400 μm, in comparison to the 150 μm alone) and might reduce it usability in the cochleae of small animals as used in the lab. Future miniaturization technologies might solve these issues. Another promising tool that generates a low divergent circular beam are vertical cavity emitting laser. However, the main drawback is that they were designed to operate in the near infrared range. Nevertheless, efforts are being made and many are working on the development of this devices in the wavelength meaningful for current optogenetic channels (Kasahara et al., 2011; Mei et al., 2017; Shang et al., 2017)although they are not yet commercially manufactured.

All in all, advances in micro-electro-mechanical system (MEMS) fabrication will more likely bring an implantable, addressable, low divergent and efficient way of delivering focused light in the cochlea that will bring us closer to the promised spectral resolution increase.

1.3.3. GENE DELIVERY VECTORS

In order to render SGN sensible to light, they need to be manipulated to express the opsin gene. Gene delivery in the inner ear using viral vectors have been achieved using different types: herpes simplex type I virus and vaccinia virus, lentiviruses, retroviruses, adenoviruses and adeno-associated virus (AAV) (reviewed in (Luebke et al., 2009)). AAV is a nonpathogenic human parvovirus that infects approximately 85% of humans within the first decade of life, has not been associated with tumors and can remain as extrachromosomal DNA (Jeschke and Moser, 2015; Luebke et al., 2009). We have shown efficient transfection of SGN in both mice and gerbil using AAV-2/6 (Dieter et al., 2019; Hernandez et al., 2014; Keppeler et al., 2018; Mager et al., 2017; Wrobel et al., 2018) and AAV-PHP.B (Dieter et al., 2019; Keppeler et al., 2018, this work (Results part of Chapter II)). In all the cases, the opsin was downstream to the human synapsin promoter and no other cell apart from neurons expressed the transgene. Thus, these serotypes of AAV seem to provide efficient transduction performance in the spiral ganglion. Using the term AAV in the clinical trial search engine of the NIH, filtering the results by those trials that are "Recruiting", "Not yet recruiting", "Active, not recruiting", "Completed", "Enrolling by invitation Studies", revealed approximately 162 studies using AAV for gene therapy in humans, in different countries (mostly in USA and EU) and for a wide variety of conditions (clinicaltrial.gov). Because of their safety, even for translational applications, these seem to be the most promising ones.

Other strategies such as liposomes, cationic polymer, polymersomes, cell-penetrating peptides, inorganic nanoparticles (Yin et al., 2014) or close-field electroporation using an electric cochlear implants (Pinyon et al., 2014) seem to be a seductive idea, specially the last one considering that more likely the first generation of optical cochlear implants would be combined with anelectrical cochlear implant. They are not so limited regarding the maximum length of DNA that can be carried and some have been included already in clinical trials (Yin et al., 2014). However, their applicability in our approach need to be explored, as for example the electroporation was most efficiently transducing cells in the immediate vicinity of the CI.

2. AIMS

In the *in vivo* experiments carried out in our lab in gerbils, rats and mice there is some degree of variability among the response of different animals. Many factors, which are not experimentally easy or even feasible to address, could underlie such variability. Some examples include differences in the expression levels of the opsins, in the transduction efficiency of the viral vectors, in the position and orientation of the light delivery device, in the irradiance received by the cells, in the presence of scar for chronic experiments or in the number of remaining cells. Furthermore, in a continuously and fasting growing field like optogenetics, it is not possible in economical, logistic or even bioethical terms, to test every new tool published.

For these reasons, we planned to build a model of the light sensitive cochlea, that integrates optical and neuronal modelling, weighted by the expression levels and tonotopic position, were different light sources and opsins could be tested to predict *in silico* a neuronal outcome. This will provide a platform for a better experimental design, for a more complete explanation of experimental unresolved questions and for testing novel and different optical implant designs and stimulations paradigms.

This long-shot interdisciplinary goal is far from being completed in the time course of a single PhD. Thus, in the following pages, I will present our advances in the development of tools for the characterization of the optogenetic stimulation of the cochlea, concentrated in the creation of an optical model and in the study of the expression levels and cell counts in the cochlea.

In first place, I, together with Dr. Kai Bodensiek, have developed a Monte-Carlo ray tracing simulation using realistic reconstructions of the cochlear parts and approximated optical values for them, that allows estimating the light distribution along the tonotopical axis. In addition, I have used it to explore different illumination settings, both experimental and theoretical. In second place, I have adapted a tissue clearing protocol to be able to study the viral transduction efficiency in the whole intact cochlea. It allows exploring the distribution the transduction process and allows to estimate the relative amount of expression of the channel of interest along the tonotopical axis. It is worth mentioning that in future work, we aim to combine these models with a third one, a single-compartment model of an opsin-expressing SGN.

CHAPTER I: DEVELOPMENT OF AN OPTICAL MODEL OF THE COCHLEA TO STUDY THE LIGHT SPREAD

1. INTRODUCTION

In the following chapter, I will introduce our strategy to study and estimate how the light spreads in the cochlea and how much light is projected onto the spiral ganglion. I will present our implementation of Monte Carlo simulations in different illumination paradigms using the gerbil and the marmoset cochlea, to obtain the light density distribution along the tonotopic axis.

1.1. LIGHT-TISSUE INTERACTION

Light can be considered either as a stream of particles (photons) or an electromagnetic wave, that oscillates at a given frequency defining its color. Both theories are interrelated by the formula $E = hv$ (E, photon energy; h, Planck´s constant, v: frequency of the wave, related to its wavelength (λ) by the speed of light, $v = c/\lambda$), which shows how the photon energy is inversely proportional to its wavelength. However, to understand the dynamics of the light propagation, the wave theory is more useful. The electrical component, orthogonal to the magnetic one, is responsible of its tissue interactions. Propagating light, with a given direction, inside of a given tissue, can transfer some of its energy to a given atom, specifically to its more external electrons. This energy can either be absorbed or not. When it is absorbed it can drive chemical reactions, be-remitted as light or converted into heat. If it is not absorbed, it can be reflected, refracted or scattered. The behavior of light propagating through a given material depends on the features of the incident light and the optical properties of the medium. The main light parameters include its: wavelength, power, spot size, spatio-temporal-spectral profile (including its spot size and duration) and polarization state. The spatio-temporal-spectral profile address how the irradiance varies across the beam, during the pulse and as a function of the wavelength. The optical properties of the medium (normally wavelength dependent, but also might be dependent on temperature, pressure, and polarization) include the absorption

coefficient (μ_a), the scattering coefficient (μ_s), the scattering anisotropy (g) and the refractive index. The first refers to the probability of a photon of being absorbed by the medium per unit of the path length. The rest define how the path traced by the photons is. The scattering coefficient defines the probability of light scattering in a medium per unit of the path length. Scattering anisotropy is the mean of the cosine of the scattering angle, and describes the variation in direction in which the scattered light is propagated (Periyasamy and Pramanik, 2017; Welch and van Gemert, 2011). The definition of the refractive index is a bit more complex and it is further developed as following.

In a very simplistic way, we could imagine charged particles within a material as masses attached to the surrounding by a spring, which has a natural resonant frequency. If the frequency of the propagating wave is equal to this frequency, the energy is absorbed. If it is different, the transfer of energy to the material is poor (Welch and van Gemert, 2011). For most interactions, the energy received is not enough to trigger a fluorescence (re-emit that energy with a lower energy) or ionizing (removal of the electron, which can be trigger by heat) event, but it causes the oscillation of that electron. The energy associated with that oscillation is released in the form of another light wave. This newly generated light wave, also called wavelet, propagates in all directions, as an expanding spherical wave. Furthermore, the electron cloud-light wave interaction very briefly stops the progression of the wave, causing a phase delay (in the range of a femtosecond, 10^{-15}s, for visible light). The sum of several of this "slowing down" events, after consecutive interactions with several molecules within the material, causes an important reduction in the velocity of the light as it propagates and is what we call the refractive index. Thus, the refractive index is defined as the ratio between the speed of light in vacuum and in the medium (Richardson and Lichtman, 2015). Although the mismatch of the refractive index at the interface between two different media is commonly known as scattering, it would be more accurate to define scattering as the inhomogeneous distribution of the amount of scattering between different regions in the material. Homogenous materials (e.g. air, water, glass) have a high density of scatterers of dimensions much smaller than any wavelength of light, that are very close to each other (3 nm in the air, 10 nm in the water). If we imagine light travelling as a plane, when it enters in any of this example medium, it sets all the molecules in that plane into a brief excited state that when relaxed generate densely packed spherical waves. Given that this event occurs simultaneously in a single plane, a nearly complete destructive interference is generated, avoiding the propagation of light in the lateral directions. In the forward direction, the wavelet propagates with a phase delay. The scatterers that are in the following plane experience the same phenomenon. Thus, all the phase-delayed forward-moving wavelets constructively sum their amplitudes, allowing the light propagation. In biological tissues, the inhomogeneity in the

scatterers present in the different components (e.g. in the intracellular space, in the membrane and in the extracellular matrix) would cause that the destructive interference will not happen totally and light will propagate also in the perpendicular direction. The tissue, then, will behave as if it would contain many small light sources propagating light of all wavelength in all directions, causing the characteristic whitish translucency of tissues (Richardson and Lichtman, 2015).

The inhomogeneity of scatterers can happen at different spatial scales. If it happens at scales much smaller than the wavelength of the travelling wave, short wavelengths have a greater probability of being scattered (e.g. Membranes, cells sub compartments, collagen fibrils). This is due to the fact the fractional intensity of the scattered light is inversely proportional to the forth power of the wavelength of incident light. This type of scattering, known as Rayleigh scattering, is more prominent for short wavelength light. This is the foundation, for example, of two-photon microscopy, that achieves deep fluorescence imaging in the tissue, or the reason why the sky is blue (the blue component of the white light is scattered more efficiently than red component by the molecules in the air). If it happens for particle larger than the wavelength of the propagating light, like big protein complexes or organelles, the scattering is mostly in the forward direction, the wavelength dependence of scattering is not significant and it follows the so-called Mie scattering. One example is why the clouds are white (when the concentration of water in the atmosphere is high enough, water droplets form and scatter all the wavelengths equally). To summarize, propagating light through a tissue can be scattered isotropically (Rayleigh) or dominantly forward (Mie) if the incident wavelength is smaller or bigger than the dimensions of the scatterers, respectively. Since the scattered light has the same wavelength as the incident one, both types of scattering are termed elastic, and both can affect the light propagation in tissue. Inelastic scattering, also known as Raman scattering, in which the scattered wavelength is different, is generally too weak in tissue and can be neglected (Richardson and Lichtman, 2015; Vo-Dinh, 2003; Welch and van Gemert, 2011).

Since we consider light as substitute of electric pulses in order to achieve a more spatially confined stimulation of the spiral ganglion, estimating how the tissue-light interaction alters the available light is crucial for the design and choice of suitable light sources in optical CIs. Although there are many alternatives to obtain an approximation of the light distribution both in 2D and 3D, we considered Monte Carlo simulation to be the most suitable method to study light propagation from our intracochlear light sources in combination with realistic reconstructions of the cochlear tissues.

1.2. MONTE CARLO MODELLING OF LIGHT SPREAD

Light rays after a scattering event produces a continuous distribution of light. Despite the fact that the radiative transfer equation and other analytic functions can be used to study simple cases of light propagation in tissue, they are extremely limited if a combination of realistic media, with a complex array of scattering effects shall be studied in 3D. One very computationally expensive solution would be to calculate the propagation of light exactly by propagating this distribution by the next interface until the irradiance can be neglected. As the Monte Carlo method is normally used to compute the outcome of random processes, it can be used to model quantum-mechanical processes than can only be described by their statistics (as the light propagation). With this purpose, this kind of numerical simulation techniques provides a more probabilistic and computationally efficient solution that can be used to study light propagation in tissue (Periyasamy and Pramanik, 2017; TracePro User´s Manual)

As proposed in the first Monte Carlo simulation used for light propagation in multilayered tissue (MCML, Wang et al., 1995) and described by (Periyasamy and Pramanik, 2017), in this type of simulation, a large package of photons or rays is launched from a source. Then, photons are then propagated (following a random walk) and tracked through the tissue of interest, that can be modelled as infinite or semi-infinite geometry. One can divide the processes as follows for clarity:

1) Initialization: The launched photons are assigned with unit weight (w) with the direction cosines along the z-axis.
    a. If there is refractive index mismatch between the propagating and the launch media, the square of the amount of light reflected back towards the source, also known as specular reflectance and defined by $R_{SP} = \left(\frac{n_0 - n_1}{n_0 + n_1}\right)^2$, where n is the refractive index of the media 0 and 1, is deducted ($w = 1\text{-}R_{sp}$) and the photon is refracted.
    b. If the boundary conditions are matched, the weight is 1 and the photon is transmitted.

2) Photon moves: The photon takes a random step size, s, defined by the scattering and absorption coefficients of the tissue and a random number, ξ, in the formula: $s = \frac{-\ln \xi}{\mu_a + \mu_s}$
    a. If the step size is greatest than the distance to the nearest boundary, the photon moves to this position and check again for reflection or transmission (Step 1)

b. If the step size is smaller than the distance:
    i. The photon is translated by *s* to the new location
    ii. A new weight is assigned and calculated from: $\Delta W = \frac{\mu_a}{\mu_a + \mu_s} W$
    iii. For scattering, the polar angle, θ, and azimuthal angle, $\emptyset$, are randomly sampled based on the direction of the recomputed cosines:
        1. θ is calculated using the Henyey-Greenstein function:

$$p(\cos\theta) = \frac{1 - g^2}{2(1 + g^2 - 2g\cos\theta)^{3/2}}$$

        2. $\emptyset$ is calculated as $\emptyset = 2\pi\xi$

3) Step 2) is repeated till the photon is dead, that is, *w = 0.*

Given the facilities that the commercial solution TracePro provides in terms of importing reconstructions, importing optical properties libraries, defining light sources or importing them from the manufacturer datasheet if available, graphical user interface and powerful performance, we decided to use this software. The algorithm that is used by TracePro simulates the scattering and diffraction of light, and sample the distribution of rays being radiated from light sources. It treats diffraction and scattering as random processes and the distribution of the latter is used as a probability density, to randomly choose the sampled rays. Likewise, the direction of rays is randomly chosen, highlighting the need of tracing a high number of rays. Thus, the simulation consists in 5 steps: 1) Creation of a solid model; 2) Definition and application of properties; 3) Ray Tracing and 4) Analysis (TracePro User´s manual). Whereas for step 1), we counted with the 3D reconstructions from X-Ray tomography data done by Dr. Daniel Keppeler provided as .stl files (also known as Stereolithography, Standard Tessellation Language or Standard Triangle Language), the rest of the steps are further developed in the Methods section of this chapter.

2. METHODS

2.1. GENERAL PROCEDURE

To study the light spread in the cochlea of different animal species of interest using different illumination paradigms we used Monte Carlo ray tracing simulation, in the software TracePro® Standard 7.8.1 (Lambda Research Corporation).

I would like to remark that the original workflow was initially designed and implemented by Dr. Kai Bodensiek in other preliminary models, during his stay in our lab in 2015-2017. My contribution to it was 1) the inclusion of the scala vestibuli and media to correct for a possible underestimation of the interturn stimulation; 2) the implementation of the query points at the level of the dendrites in the marmoset model; 3) the design and application of the light sources of the different gerbil´s model (although he also assisted in the initial steps of the experimental position model); and 4) analysis after irradiance calculation and some modifications in the original scripts. I implemented all of it to study the light spread in the marmoset and gerbil cochlea, presented in this thesis.

2.1.1. 3D RECONSTRUCTION OF COCHLEAR TISSUES

Three different cochlear compartments were reconstructed from X-Ray tomography by Dr. Daniel Keppeler in Avizo and imported as meshes in .stl files with less than 10000 triangles (to keep a good relation between structure resolution and computational load). This cochlear compartments were: Scala Vestibuli and Media, Scala Tympany, Rosenthal´s canal (RC) and modiolus.

In Autodesk Inventor Professional 2017 (student license) with the plugin Inventor Mesh Enabler 1.0.6, the meshes were repaired using the “Repair bodies” function and exported them as a .sat file. This files were imported to Trace Pro and scale was checked and corrected, if need it.

To account for the bone, a solid cube was created and scaled to cover the rest of the cochlear structures.

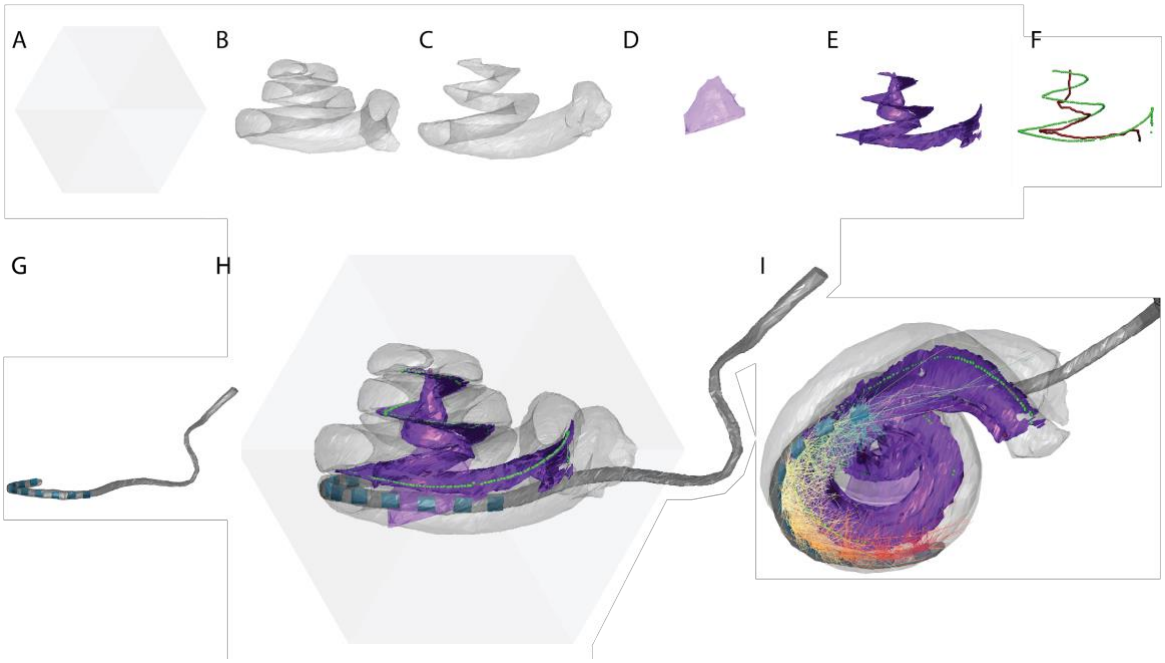

Figure 1. Marmoset model components. A. Solid cube to account for the bone. B. Scala vestibuli and media. C. Scala tympani. D. Modiolus. E. Rosenthal´s canal and neuronal peripheral processes. F. Query points (enlarged for a more clear display, r = 25µm – original r = 5 µm). Green, query points at the edge of the peripheral processes. Red, query points along the centerline of the Rosenthal´s canal. G. Optical cochlear implant. Grey, flexible substrate. Blue, µled. H. Model components assembled. I. Close-up of the bottom view displaying a portion of the rays traced. Every LED´s ray is displayed with a different color.

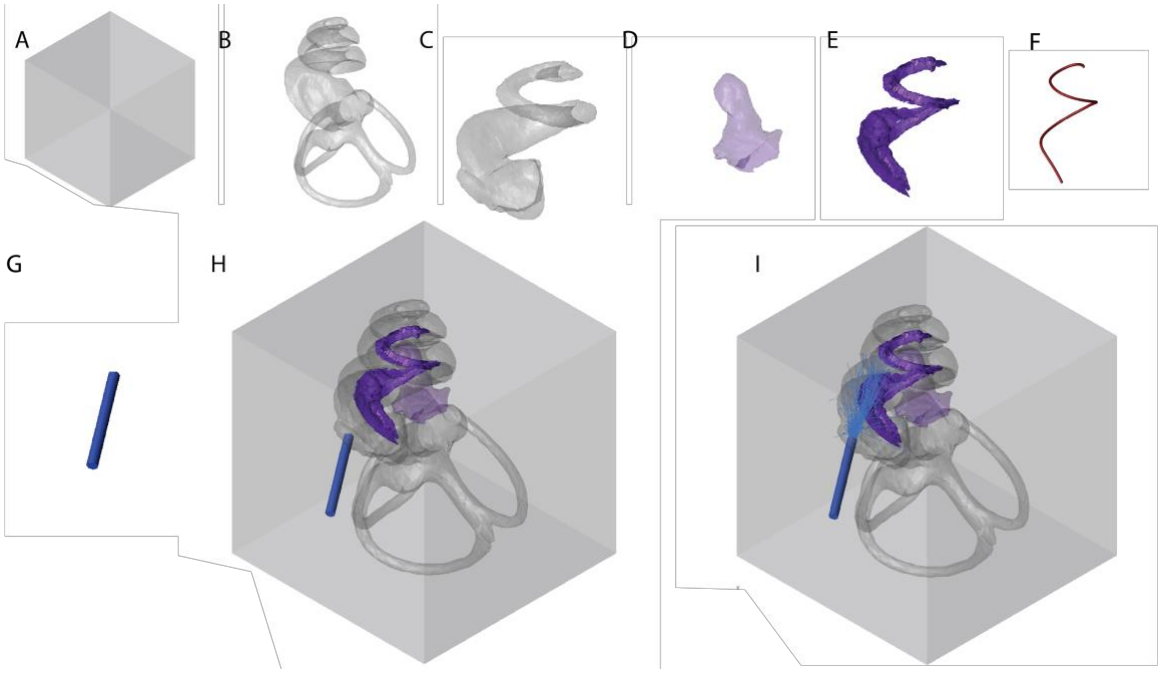

Figure 2. Gerbil model components. A. Solid cube to account for the bone. **B.** Scala vestibuli and media, together with the Semicircular canals. **C.** Scala tympani. **D.** Modiolus. **E.** Rosenthal´s canal and neuronal peripheral processes. **F.** Query points along the centerline of the Rosenthal´s canal (enlarged for a clarity, r = 25µm, original r = 5 µm). **G.** Optical fiber. **H.** Model components assembled. **I.** Model displaying a portion of the rays traced.

2.1.2. QUERY POINTS

2.1.2.1. ROSENTHAL´S CANAL

In order to mine the values of radiant flux, 300 query points, in the form of a 5μm diameter sphere were placed in a series of coordinates provided by Dr. Daniel Keppeler. The coordinates were obtained by fitting a spline along the centerline of the mesh corresponding to the Rosenthal´s canal in Avizo and the tonotopical organization was mapped by the use of the Greenwood´s function (Greenwood, 1961).

For the Gerbil, two different tonotopic maps were used. For the model done to study the experimental scenario and the optimal sources, published in (Wrobel et al., 2018), we fit the tonotopy-place map by using the hearing ranges described in (Müller, 1996)(ie. 32.1 - 0.25 kHz):

$$f = 0.255(10^{2.1x} - 0.01)$$

For the model accounting for translational and rotational variations at three different cochlear positions, published in (Dieter et al., 2019), since it was needed to fit the full hearing range of the Gerbil as 50-0.195 kHz, the following function was used:

$$f = 0.39(10^{2.1x} - 0.5)$$

For the marmoset, for a hearing range of 36.34-0.14 kHz, the following Greenwood´s function was used:

$$f = 0.29(10^{2.1x} - 0.57)$$

2.1.2.2. DENDRITES

For the marmoset model, we probed the amount of light reaching the peripheral processes of the SGN. 600 query points were obtained from fitting a spline to a series of points manually registered along the edge of the peripheral processes. However, most of these initial query points provided were not embedded inside the mesh (condition needed). In order to correct the location, the following steps were taken (**Figure 3**):

1. An array of approximated 23.5M points, spaced in 5 μm, was created.

2. All those that were outside the reconstructed peripheral processes were removed (435K points)
3. All those that were more than 100 µm away from the original query points were removed (70K points)
4. In each of the remaining ones, an sphere with 400 points in its surface was generated. I check the percentage of these points that were inside of the mesh. All those that did not have 100% of the points inside were discarded (45K points)
5. From these remaining ones, only 1 per original query point was kept: the one that had the minimal distance to the initial query points (600 points)

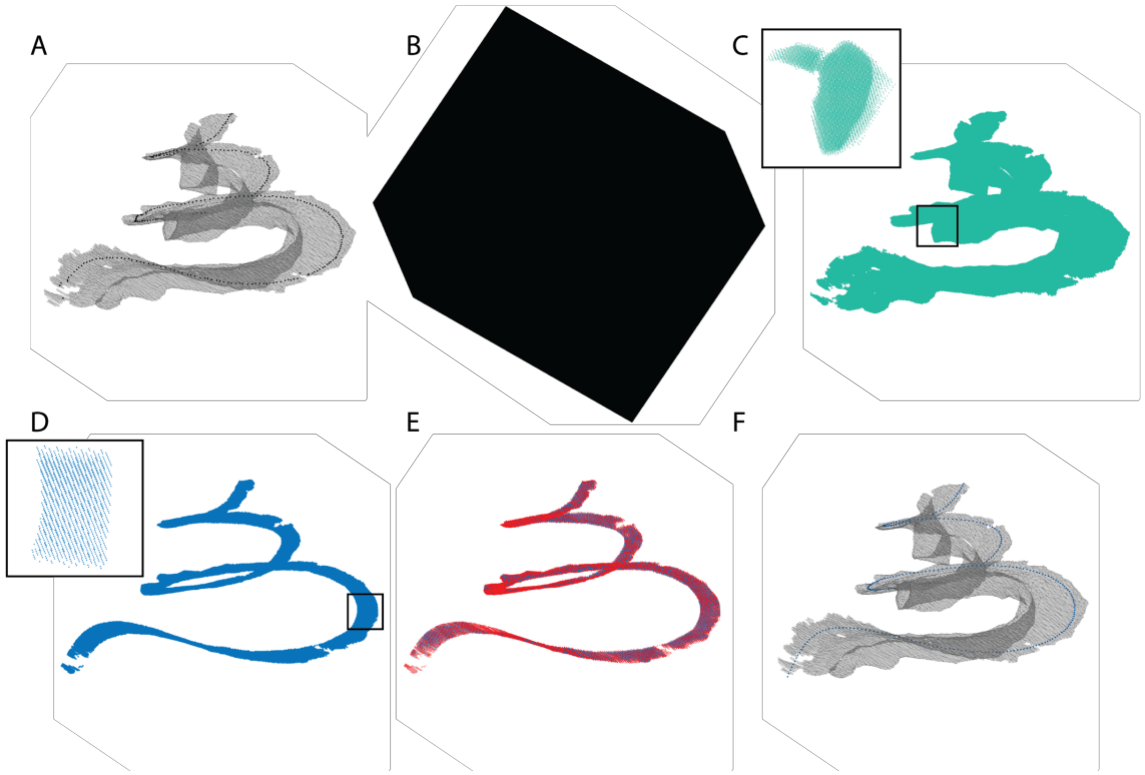

Figure 3. Calculation of query points at the peripheral processes of the marmoset cochlea. A. grey, mesh corresponding to the Rosenthal´s canal and the peripheral processes query points. Black, initial query points (600). **B.** Array of points spaced by 5 µm (~23.5m points). **C.** Array of points from b inside of mesh from a (~435k points). **D.** Array of points closer to 100µm from any query points(~70k points). **E.** Points that can (blue, ~45.5k) or cannot (red, ~24.8k) have the center of a 5 µm sphere embedded in the mesh. **F.** Nearest neighbor to initial query points (600 points)

2.1.3. DATA RETRIEVAL

Radiant flux from every sphere was retrieved from each sphere programmatically. Then, irradiance was calculated as radiant flux/4*pi*radius$_2$ and used for further analysis.

2.2. OPTICAL TISSUE PROPERTIES APPROXIMATION

The optical properties were mined from the literature, averaged and provided by Dr. Kai Bodensiek, then TracePro libraries for bulk scatter and material properties were also generated by him.

2.2.1. ANISOTROPY FACTOR, G

A. BONE

Value	Sample	Publication
0.6	Guinea pig, Cochlear bone, @633nm	(Okamoto Ugnell and Öberg, 1997)
0.87	Skull bone, @488nm	(Niemz, 2007)
0.92	Skull bone, @950nm	(Firbank et al., 1993)
0.94	Skull bone, @950nm	(Firbank et al., 1993)
0.92	Skull bone, @400-600nm	(Jacques, 2013)
0.83	Mean	

B. BRAIN

Value	Sample	Publication
0.82	White matter, @632nm	(Tuchin, 2015)
0.9	White matter, @488nm	(Jacques, 2013)
0.8	Gray matter, @488nm	(Jacques, 2013)
0.74	Brain, @633	(Yavari et al., 2005)
0.88	Gray matter, @460	(Bernstein et al., 2008)
0.89	Gray matter, @590	(Bernstein et al., 2008)
0.84	Mean	

C. PERILYMPH

Value	Sample	Publication
0.9		(Heiskala et al., 2005)

2.2.2. REFRACTIVE INDEX, N

A. BONE

Value	Sample	Publication
1.5	Skull, @532nm	(Niemz, 2007)
1.45	Dentine, @633-750nm	(Ye et al., 2011)
1.55	Bone, @VIS	(Ye et al., 2011)
1.5	Mean	

B. BRAIN

Value	Sample	Publication
1.36	Gray matter, @585nm	(Tuchin, 2015)
1.3847	Neuron, @658nm	(Rappaz et al., 2005)
1.3751	Neuron, @658nm	(Rappaz et al., 2005)
1.36	Human gray matter, @456/514/630/675/1064nm	(Gottschalk, 1992)
1.36	Rabbit gray matter, @456/514/630/675/1064nm	(Gottschalk, 1992)
1.368	Mouse brain slice, @633nm	(Lue et al., 2007)
1.37	Mean	

C. PERILYMPH

Value	Sample	Publication
1.355	Extracellular liquid, @585nm	(Tuchin, 2015)
1.35	Interstitial fluid	(Tuchin, 2015)
1.35	Mean	

2.2.3. SCATTERING COEFFICIENT, μ_S

A. BONE

Value	Sample	Publication
14.5	@460	(Jacques, 2013)
13.9	@488	(Jacques, 2013)
12.1	@594	(Jacques, 2013)

B. BRAIN

Value	Sample	Publication
17.1	@460	(Jacques, 2013)
15.6	@488	(Jacques, 2013)
11.3	@594	(Jacques, 2013)

C. LIQUOR

Value	Sample	Publication
1^mm-1		(Steinbrink, 2000)

2.2.4. ABSORPTION COEFFICIENT, μ_A

A. BONE

Value	Sample	Publication
2.69	Cochlear bone, @633 nm	(Okamoto Ugnell and Öberg, 1997)
2.28	Cochlear bone, @750 nm	(Okamoto Ugnell and Öberg, 1997)
0.022	Adult Skull, @849 nm	(Bevilacqua et al., 1999)
0.045	Pig Skull, @650-950 nm	(Firbank et al., 1993)
0.02	Human Skull, @680	(Bevilacqua et al., 1999)
1.67	Mouse skull, @488	(Soleimanzad et al., 2017)
2.29	Mouse skull, @705	(Soleimanzad et al., 2017)
1.29 mm^-1	Mean	

B. BRAIN

Value	Sample	Publication
0.04	Neonatal gray matter, @650 nm	(Van der Zee, 1992)
0.1	Adult gray matter, @700 nm	(Van der Zee, 1992)
0.0026	Pig brain. @630 nm	(Patterson et al., 1987)
0.0017	White & gray matter, @680 nm	(Patterson et al., 1987)
0.05	Mean	

C. LIQUOR

Value	Sample	Publication
0.016	@680	(Steinbrink, 2000)

2.2.5. SUMMARY

	Anisotropy, g	**Refractive index, n**	**Scattering coefficient, μ_s**				**Absorption coefficient, μ_a**
Bone	0.83	1.5	14.5	13.9	12.1	-	1.29
Brain	0.84	1.37	17.1	15.6	11.3	-	0.05
Perilymph/CSF	0.9	1.35	-	-	-	1	0.016
			460nm	488nm	594nm	680nm	

2.2.6. TRACE PRO LIBRARIES

In TracePro, the following libraries were generated:

A. MATERIAL PROPERTY

Tissue	Temperature(K)	Wavelength (μm)	Index	Absorption[/mm]	Extinction, K [μm/μm]
Bone	300	0.46	1.5	1.29	4.72e-5
	300	0.488	1.5	1.29	5.01e-5
	300	0.594	1.5	1.29	6.1e-5
Brain	300	0.46	1.37	0.05	1.83e-6
	300	0.488	1.37	0.05	1.94e-6
	300	0.594	1.37	0.05	2.363e-6
Liquor	300	0.46	1.35	0.016	5.86e-7
	300	0.488	1.35	0.016	6.21e-7
	300	0.594	1.35	0.016	7.56e-7

B. BULK SCATTER

The type of Bulk Scatter selected was Henyey-Greenstein and the parameters are described in the following formula:

$$SDF = p(\theta) = \frac{1 - g^2}{4\pi(1 + g^2 - 2\, g\, cos\theta)^{\frac{3}{2}}}$$

Tissue	Wavelength (μm)	Anisotropy (g)	Scatter Coeff (1/mm)
Bone	0.46	0.83	14.5
	0.488	0.83	13.9
	0.594	0.83	12.1
Brain	0.46	0.84	17.1
	0.488	0.84	15.6
	0.594	0.84	11.3
Liquor	0.46	0.88	1
	0.488	0.88	1
	0.594	0.88	1

2.3. LIGHT SOURCES DESIGN

2.3.1. MODEL OF THE GERBIL COCHLEA

2.3.1.1. CONSTRUCTION

A. EXPERIMENTAL FIBER: EXPERIMENTAL POSITION MODEL

The original fiber was reconstructed by Dr. Daniel Keppeler. In order to keep the consistency with the rest of the models, a cylinder of 200 μm was modelled and placed overlapping the reconstruction of the fiber (not considered any further).

B. EXPERIMENTAL FIBER: ROTATION AND TRANSLATION MODEL

Since the experimental fiber was reconstructed from X-Ray tomography of a cochlea in which the fiber was fixed with dental cement before imaging, the model of the experimental position represents a single snapshot of the experimental setting and does not account for the inherent variability of locations and angles that the fiber could have during the experiment and between experimental sessions. To account for this, and with the aim to corroborate the position of the fibers in an experiment in which cochleae of gerbils expressing Catch were stimulated in three different positions, we developed two models with three positions and 1) five different angles (0, ± 15 degrees placed in orthogonal planes - Rotational model) or 2) five different lengths from the ganglion (0, ±100, ±200 μm - Translational model).

The coordinates for the tips of optical fibers were placed on the reconstructed cochlear lateral wall in anatomically meaningful positions corresponding to fiber placement in our in vivo experiments, guided by Alexander Dieter, who performed the experiments. These coordinates were then translated following a straight line to Rosenthal´s canal to a given distance from the query points: 400, 700 and 900 μm for apical, mid-cochlear and basal stimulation, respectively. The newly calculated coordinate was defined as the origin of the radiation and the straight line as its normal vector. The origin and the normal vector of all five emitting surfaces (initial position plus 4 rotations or four translations) at the three positions were imported to TracePro.

Radiant flux was read from the 300 query points. Irradiance values were linearly scaled to 2.67 mW, which was the mean threshold for optogenetic stimulation observed in our experiments (Dieter et al., 2019). The mean irradiance profile was calculated for every position using the

irradiance profile of all emitting surfaces, and the tonotopic location to which the fiber was facing was then calculated as the peak of the mean irradiance profile.

C. Optimal source

To design an optimal source, we chose a fiber with small diameter and numerical aperture (taken from the catalogue of Thorlabs), in order to achieve the smallest illumination area and most directional source possible. The optical fiber selected was Thorlabs FG010LDA and it was modeled as a cylinder of 10 µm of diameter in Autodesk Inventor. The orientation and location were calculated as following (**Figure 4**):

- The centerline of the Scala tympani was divided in segments of 570 µm.
- The center coordinate of each of this segment was calculated and defined as the center of the emitting surface
- The orientation was defined as a vector originated in this center and pointing towards the closest Rosenthal´s canal´s query point.

A list of centers and vectors was stored and imported to TracePro including them in a custom-made script.

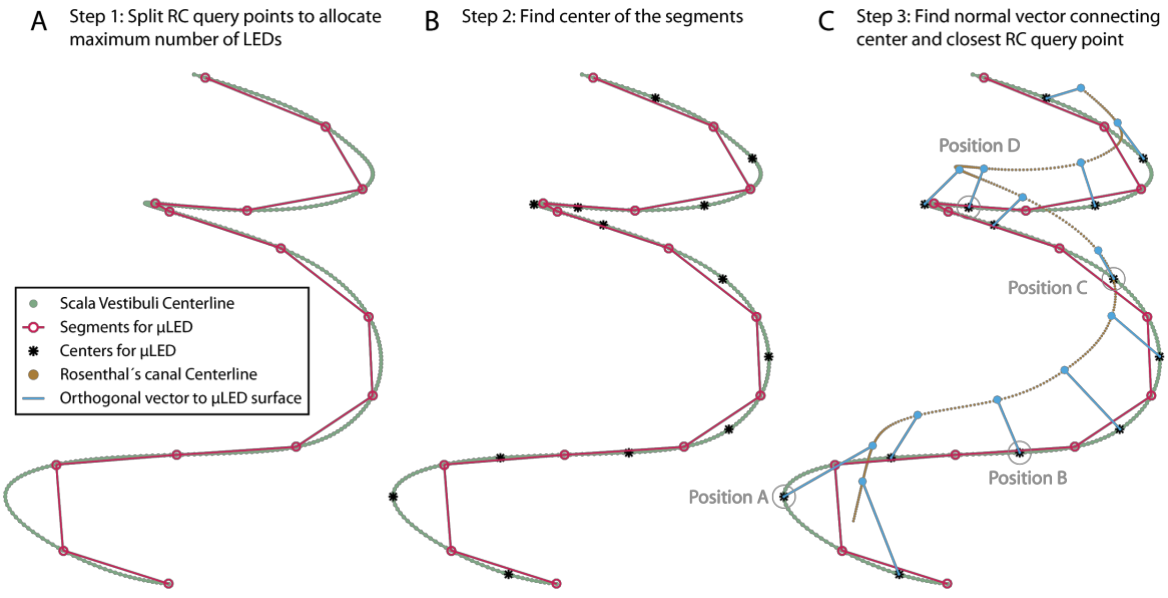

Figure 4. Schematic representation (2D projections) of the calculation of the positions of the optimal sources.

2.3.1.2. LIGHT SOURCES FEATURES

Both experimental and optimal light source were defined as grid sources exiting the modelled fiber from the face most proximal to the ganglion. The parameters for both were defined as in the **Table 1**

Table 1. Parameters of the light sources used

Model used	Gerbil, Experimental fiber	Gerbil, Optimal source
Source Name	Thorlabs FT200UMT	Thorlabs FG010LDA
NA	0.39	0.1
Diameter	200 µm	10µm
Type of source	Grid	Grid
Pattern	Circular	Circular
Number of rays (rings)	3003001 (1001)	3003001 (1001)
Ray wavelength	473	473
Uniform total density	10 mW	10 mW
Grid boundary radius	100 µm	5 µm
Spatial and angular beam distribution	Symmetric Gaussian	Symmetric Gaussian
Waist radius of Gaussian beam profile	100 µm	5 µm
Half angle profile of the beam*	16.79°	4.25°

*$\theta = \sin^{-1}(NA_{fiber}/n_{Scala\ Tympani})$ (θ: half angle; NA, numerical aperture; n, refractive index).

2.3.2. MODEL OF THE MARMOSET COCHLEA

2.3.2.1. CONSTRUCTION

The implant reconstructed contained the silicone embedding and the bonding pads at the PCB. The LEDs selected were the CREE TR2227 with a wavelength 460 nm. According to the manufacturer datasheet, the LED had the following physical specifications:

Table 2. CREE TR2227 LED description

Description	*Dimension (µm)*	*Tolerance*
P-N Junction Area	190x230	± 35
Chip Area	220x270	± 35
Chip Thickness	50	±15
Au Bond Pad Diameter Anode	80	-5, +15
Au Bond Pad Thicknesses	1	± 0.5
Au Bond Pad Area Cathode	80x80	-5, +15
Bottom Area	190x240	±35

Each LED was modelled as a rectangular prism (190x230x50µm) in Autodesk Inventor Professional 2017, creating a working plane out of 3 points in each pair of bonding pads. Each LED was individually saved as a .sat file and imported to TracePro. The flexible substrate of the oCI was included as a mesh of 3000 triangles.

2.3.2.2. LIGHT SOURCE FEATURES

The surface facing the ganglion was designated as the emitting surface (which was typically also the case in the experiments) and the emission profile defined in the datasheet was imported to TracePro by Dr. Kai Bodensiek (**Figure 5**). The light source was set at 10 mW, with 3 million rays with a wavelength of 459 nm.

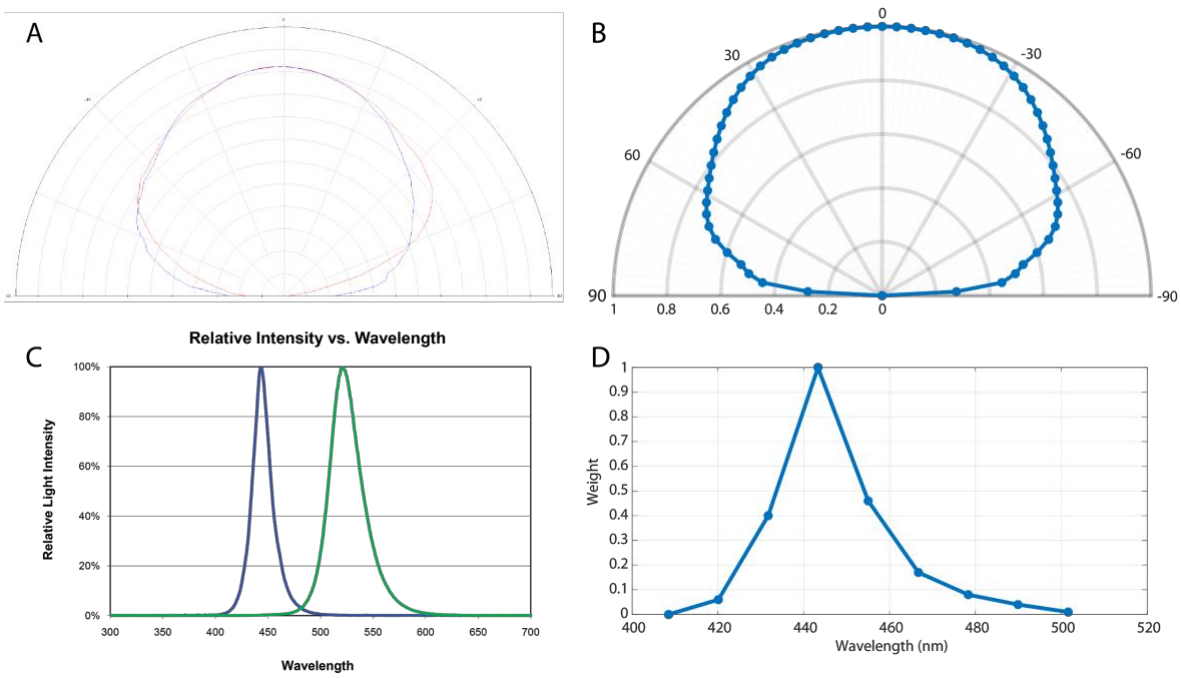

Figure 5. Angular and spectral emission pattern of µLED CREE TR2227. A. representative radiation pattern reproduced from manufacturer datasheet. **B**. Angular distribution imported to TracePro using the "Surface source property generator" app. **C.** Spectral distribution of light sensitivity from manufacturer datasheet (blue, chip modelled. Green, yellow-shifted chips also described in the same datasheet). **D.** Wavelength weights for the angular distribution imported to TracePro using the surface source property generator app.

Threshold irradiances were calculated as the minimal maximal irradiance across the 10 µLEDs, using a source radiant flux of 3 mW (PP: 1.8 mW/mm$_2$; RC: 0.87 mW/mm$_2$). Tonotopic localization corresponding to the crossing points with these threshold values were used to calculate the suprathreshold frequency range in octaves. All the data processing and analysis was done in MATLAB R2016a (The Mathworks, Inc) with custom scripts.

3. RESULTS

3.1. MODEL OF THE GERBIL COCHLEA

3.1.1. EXPERIMENTAL OPTICAL FIBER

We have demonstrated the feasibility of stimulating the Gerbil auditory system with blue light (Wrobel et al., 2018). The animals were injected with AAV2/6 virus carrying Catch, a calcium permeable ChR2 variant, under the human Synapsin (hSyn) promoter. After successful registration of activity at different stations of the auditory pathway and being able to elicit behaviorally relevant responses, the question of how was the spread of excitation as a function of the tonotopic position remained elusive. Given the obvious spatial constrains, the direct experimental measurement of the light spread is virtually impossible. We ought to answer the question of how light spreads within the cochlea using a Monte Carlo ray tracing model based on an x-ray imaged gerbil cochlea with the 200 µm optical fiber implanted into scala tympani via the round window and fixed with dental cement (**Figure 6**). We modeled 3 million rays, with a wavelength of 473 nm, to investigate the spread of excitation at the center of Rosenthal's canal, where the somata of SGNs are housed. With a fiber output of 1 mW (chosen from the thresholds for most sensitive neurons recorded in the primary auditory cortex in the range around 10 kHz), we estimated the threshold for neuronal excitation in Rosenthal's canal to be 0.06 mW/mm$_2$ and the bandwidth of excitation to range from 10 to 14.7 kHz (0.56 octaves; **Figure 6B and C**). As expected, we observed an increased light spread with fiber outputs of 5 and 10 mW that reached suprathreshold irradiances at cochlear regions with best frequencies of 5.7 to 26.3 kHz (2.2 octaves) and 3.05 to 32.1 kHz (3.4 octaves), respectively (**Figure 6B and C**). For these stronger light intensities, additional peaks of excited SGNs were observed: 0.51 to 0.87 (5 mW) and 0.39 to 1.34 kHz (10 mW; **Figure 6B and C**).

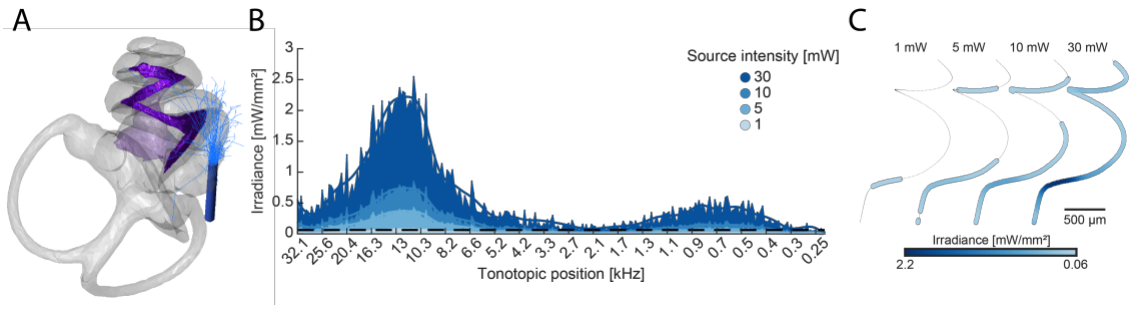

Figure 6. Model of an experimental optical fiber. Monte Carlo ray tracing simulation from a 200µm optical fiber in a gerbil cochlea (λ = 473nm), comparable to the one used in the in vivo experiments (THORLABS FT200UMT, 0.39 NA). **A.** Morphologically realistic 3D model reconstructed from x-ray tomography. Purple: Rosenthal's canal,

neuronal peripheral processes; light purple: modiolus; grey: scala tympani, media and vestibuli as well as semicircular ducts; blue: modelled optic fiber. For illustrative purposes, rays with an intensity 50% above minimum from 7351 rays (out of 3 million used for the simulation) are displayed. **B.** Iirradiance profile obtained from 300 query points placed along the centerline of the Rosenthal's canal and their corresponding smoothed traces at four different intensities covering the range employed during in vivo experiments. Dashed line represents threshold, considered as the smoothed irradiance value at 10 kHz. **C.** XY projection of the query points. Color of the query points is displayed as function of the irradiance normalized to the maximal value obtained at 30 mw for suprathreshold values. Black points represent positions with subthreshold irradiance. Reproduced with permission from (Wrobel et al., 2018)

3.1.2. Optimal light source

Given the wide profile, the projection of light from the round window does not represent the appropriate optical stimulation strategy for a future oCI. We wanted to estimate the spread of an light source with optimal emission properties and position in Scala tympani. Therefore, we also modeled the spread of excitation for light delivered by a small optical fiber (10 µm of diameter with a 0.1 NA) as an ideal light emitter placed at four different locations in the center of scala tympani along the tonotopic axis each facing Rosenthal's canal that houses the SGN somata (**Figure 7B and C**). Our simulations revealed narrow light spread and indicated that excitation of distinct populations of SGNs can be achieved using optogenetic stimulation at emitter intensities in the range of microwatts (**Figure 7B and C**).

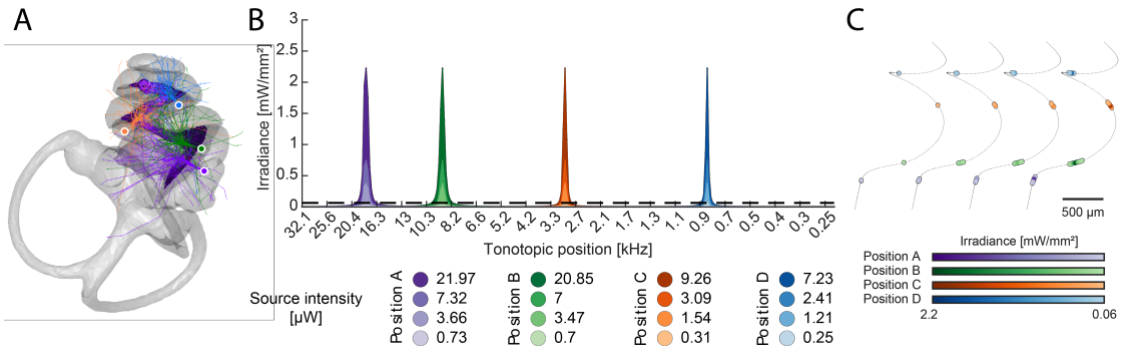

Figure 7. Model of an ideal light source placed in different positions along the cochlea. Monte Carlo ray tracing simulation from a THORLABS FG010LDA optical fiber (0.1 NA, λ = 473nm) at four different positions. These simulations show narrower spread of light using optimal conditions of position and beam divergence. Black points represent positions with subthreshold irradiance **A.** The origin of the sources were placed at the centerline of the scala tympani facing the Rosenthal's canal perpendicularly. Purple: Rosenthal's canal, neuronal peripheral processes; light purple: modiolus; grey: scala tympani, media and vestibuli as well as semicircular ducts; blue: modelled optic fiber. For illustrative purposes, rays with an intensity 50% above minimum from 7351 rays (out of 3 million used for the simulation) are displayed. FG010LDA optical fiber output at position a (slate blue), b (green), c (red) and d (blue). For illustrative purposes, rays with an intensity 50% above minimum from 7351 rays (out of 3 million used for the simulation) are displayed for every position. **B.** Irradiance profile obtained as in Figure 6B in

four independent simulations (one for each source position). For every source position, the maximum intensity was scaled to the maximum of Figure 6B. The total source intensity needed to achieve comparable irradiances as in Figure 6A is roughly 3 orders of magnitude lower. C, Merged XY projection of the query points from the four simulations. For each source position, color intensity of the query points is displayed as function of the irradiance normalized to the maximal value obtained at highest source output for suprathreshold values. Black points represent positions with subthreshold irradiance. Reproduced with permission from (Wrobel et al., 2018)

3.1.3. EXPERIMENTAL OPTICAL FIBER: ROTATION AND TRANSLATION MODEL

In another set of experiments (Dieter et al., 2019), we studied the spread of the light at the level of the inferior colliculus by placing the fiber at three different positions, one the round window and two through cochleostomies in the mid- and low frequency-ranges of the cochlea. In this occasion, we used our Monte Carlo model to estimate where the fibers were placed. Our initial model was a snapshot: we only considered one single position for the fiber: the one it had when it was fixed by dental acrylic before the imaging. This however does not take into account the inherent experimental variability of the fiber position within a range in terms of angle of illumination and distance of the plane of emission from Rosenthal's canal. To calculate more accurately the mean location of the fiber's tip for each of the insertion positions, we generated two more realistic model: One with five different angle per position and other with five different separations from the ganglion. The averages from both models retrieved comparable target location: the rotational model pinpointed that the target tonotopic locations were 1.01, 6.9 and 22.89 kHz (**Figure 8A and B**), respectively, whereas the translational model yielded 1.02, 6.34 and 21.81 kHz (**Figure 8C and D**).

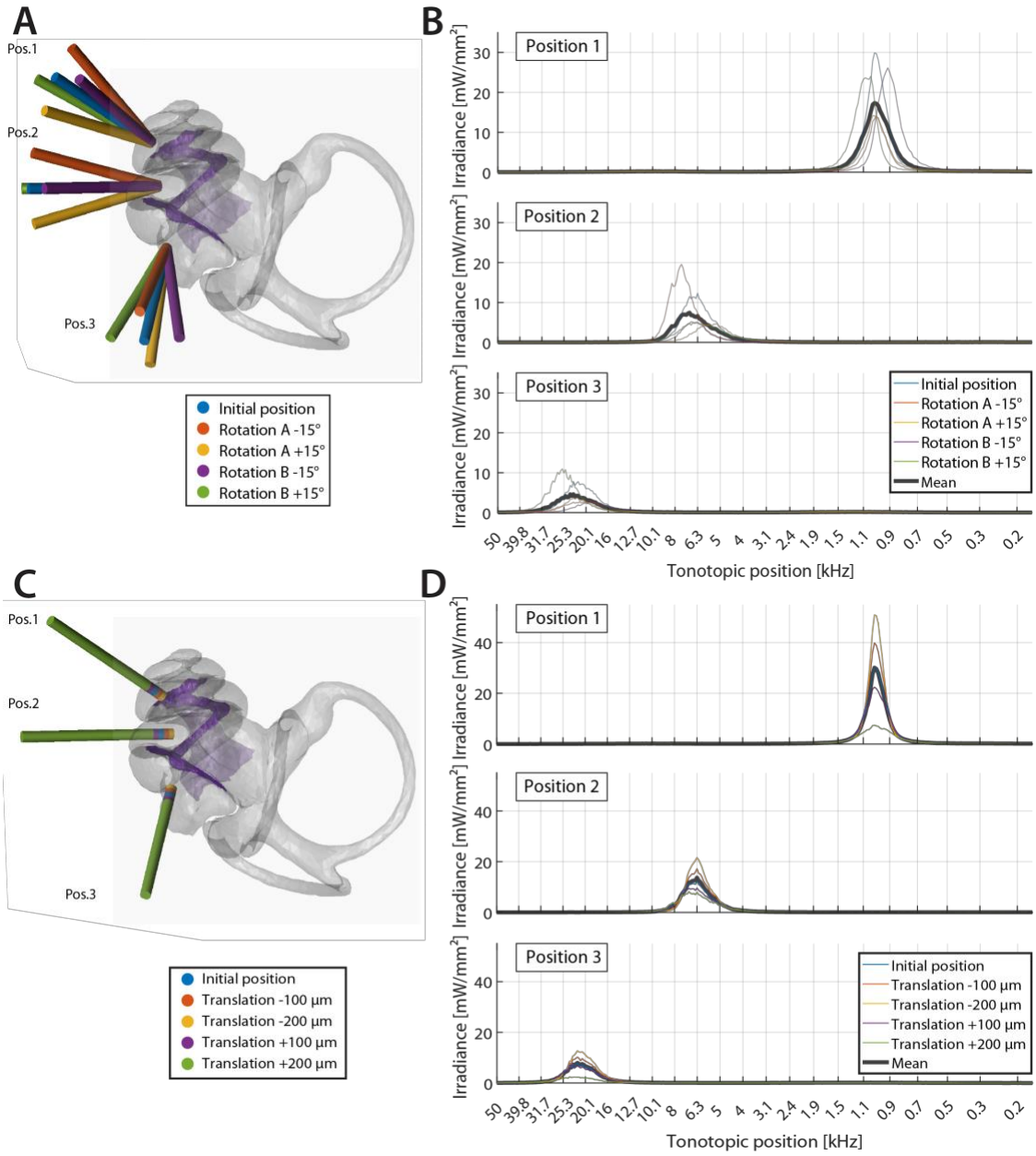

Figure 8. Verifying fiber positions by Monte Carlo ray tracing. 3D model reconstructed from x-ray tomography including fiber positions (pos. 1-3), roughly corresponding to the ones used in physiological experiments. In the model, original positions as well as their respective rotation in two orthogonal planes (a and b, panel **A.**) and four different coaxial translations (**C.**) have been used to account for variability in fiber placement. Light grey: bone; grey: scala media, vestibuli and tympani, as well as semicircular canals; purple: peripheral processes and Rosenthal's canal that houses the spiral ganglion neuron's somata; fiber position and their corresponding rotations and translations, respectively, are indicated by different colors (see legend). (**B. and D.**) irradiance profiles obtained from 300 query points located along the tonotopic axis, defined in the centerline of the Rosenthal's canal, upon Monte Carlo ray tracing from the three different fiber positions using a source radiant flux of 2.67 mw. Peak irradiances of the mean traces indicate that fibers from these different positions were stimulating areas around 1.01, 6.9 and 22.89 kHz, according to the rotation model in panel b, and 1.02, 6.34 and 21.81 khZ according to the translational model in panel d.. Reproduced from (Dieter et al., 2019)

3.2. MODEL OF THE MARMOSET COCHLEA

Finally, for late preclinical work in non-human primates, we wanted to study a marmoset cochlea implanted with an oCI (constructed with an array of μLED embedded in a flexible biocompatible substrate). We also included query points not only in the Rosenthal´s canal but also at the level of the peripheral SGN processes, to also consider the spread of excitation in case of surviving fibers.

I defined threshold irradiances as the minimal maximal irradiance across the 10 μLEDs, using an arbitrary source radiant flux of 3 mW. The irradiance threshold values were are 1.81 mW/mm^2 for the query points at the peripheral processes and 0.87 mW/mm^2 for those at the Rosenthal´s canal. To measure the spread in suprathreshold octaves (ie. tonotopic regions that have irradiance values above threshold), I retrieved the tonotopic localization corresponding to the crossing points of the irradiance profile with these threshold values.

For every light source at 10 mW, a different peak can be identified covering in total 2.3 octaves (2.35-11.55 kHz). The irradiance profiles show certain degree of overlap and spreads ranging from 0.91 to 1.19 octaves at the Rosenthal´s canal and from 0.29 to 0.53 at the peripheral processes. For every source, a slight shift, between 0.09 to 0.47 octaves, in the peak of activation can be observed when the profiles from the Rosenthal´s canal and those from the peripheral processes are compared. However, it cannot be discarded to be an artifact of the tonotopy map calculation and its extrapolation to the Rosenthal´s canal.

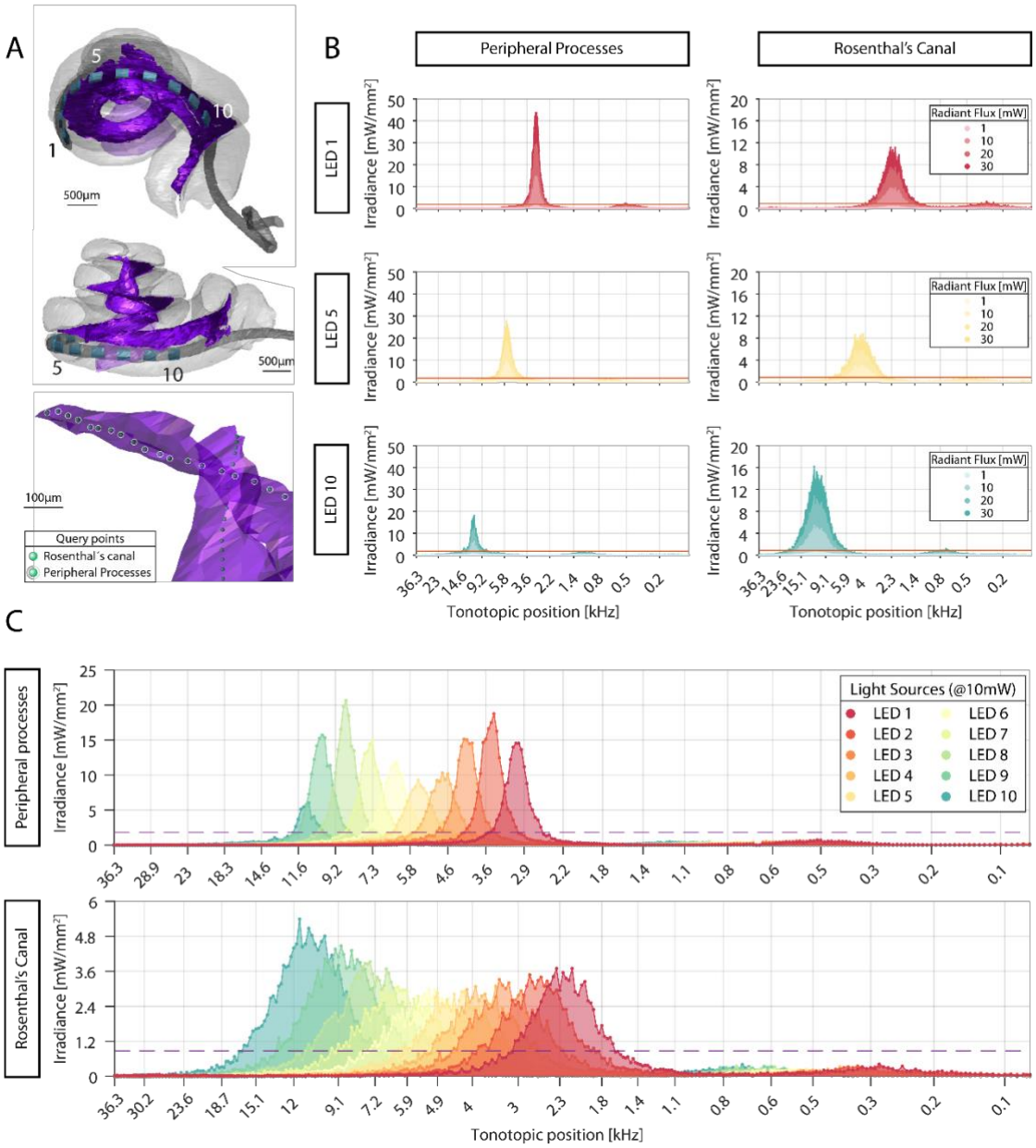

Figure 9. Model of marmoset cochlea with an optical cochlear implant containing the µLEDs CREE 2227. A. Upper and mid panel, Different views of the reconstructed volumes from X-Ray tomography used in the simulations, depicting a Marmoset cochlea with a oCI implanted. Lower panel, Close-up displaying the localization of the query points in the apical turn. Purple, Rosenthal´s canal and peripheral processes; light gray, Scalae vestibuli, media and tympani; oCI: Blue, µLED; Dark grey, flexible substrate. The light sources are numbered 1-10 from the most apical one. **B.** Light irradiance profiles obtained from µLED 1, 5 and 10 at the query points placed in the Rosenthal´s canal and the outermost edge of the peripheral processes. Orange line displays irradiance threshold values (1.81 mW/mm2 for peripheral processes; 0.87 mW/mm2 for Rosenthal´s canal). **C.** Light irradiance profiles from all the light sources interrogated at a radiant flux of 10 mW. The suprathreshold illumination area ranges from 0.91 to 1.19 octaves at the Rosenthal´s canal and from 0.29 to 0.53 at the peripheral processes. Dashed lines displays irradiance threshold values (1.81 mW/mm2 for peripheral processes; 0.87 mW/mm2 for Rosenthal´s canal)

Table 3. Summary of Monte Carlo simulation of the light spread in the Marmoset cochlea from modelled µLEDs. For every LED, the suprathreshold octaves (area with irradiance values higher than the threshold value expressed in octaves) for every radiant flux considered, the shift between the peaks at the peripheral processes and the Rosenthal´s canal and the tonotopic positions in which the irradiance profile is maximum are displayed Irradiance threshold values are 1.81 mW/mm2 for query points place at the peripheral processes; 0.87mW/mm2 for those at the Rosenthal´s canal. Note that for high radiant fluxes, interturn stimulation is possible, according to this model.

LED	Query Points	Peak [kHz]	Peak Shift (octaves)	Radiant Flux [mW]				Suprathreshold Octaves
				1	10	20	30	
1	*RC*	2.35	0.33	-	0.92	1.33	1.51; 0.12	
	PP	2.96		-	0.48	0.66	0.78; 0.08	
2	*RC*	2.77	0.32	-	1.02	1.31	1.52; 0.38	
	PP	3.45		0.02	0.45	0.64	0.85	
3	*RC*	3.35	0.31	-	0.99	1.32	1.47	
	PP	4.15		-	0.53	0.73	0.91	
4	*RC*	3.42	0.47	-	0.96	1.36	1.49; 0.05	
	PP	4.75		-	0.50	0.78	1.00	
5	*RC*	4.16	0.41	-	1.00	1.29	1.53	
	PP	5.52		-	0.52	0.77	0.99	
6	*RC*	5.18	0.28	-	01.04	1.36	1.62	
	PP	6.31		-	0.52	0.73	1.00	
7	*RC*	6.28	0.22	-	01.09	1.43	1.63	
	PP	7.32		-	0.49	0.73	0.83	
8	*RC*	7.46	0.21	-	1.16	1.51	1.74	
	PP	8.63		0.06	0.53	0.70	0.87	
9	*RC*	8.93	0.16	-	1.18	1.51	1.7479; 0.09	
	PP	10.01		-	0.40	0.68	0.87	
10	*RC*	11.55	0.09	-	1.20	1.54	1.73	
	PP	10.87		-	0.29	0.48	0.73	

*RC, Rosenthal's canal; PP. Peripheral processes

4. DISCUSSION

In the last pages, we have introduced a series of Monte-Carlo simulations of the light spread in the cochleae of different animal species and with different light sources. They included several models of the Mongolian gerbil cochlea to study the light distribution from an optical fiber similar to the one use in our in vivo experiments. The first model was developed using a fixed experimental position, obtained from µCT imaging. The others used three different positions, considering the rotational and translational movements to address the inherent variability present between experimental sessions. We also used the gerbil's cochlea to study a proof-of-concept of an optimal light source: a thin optical fiber, with narrow NA and facing directly the SGNs somas. To address a more translational aspect of the optical cochlear implant, we simulated a realistic optical cochlear implant with real emission profile of commercial µLED in the cochlea of the marmoset and studied the irradiance not only at the level of the Rosenthal's canal but also the peripheral processes of the SGN.

In our *in vivo* experimental setting the only measurement that we can do to characterize our light stimulus intensity is the optical power or radiant flux, obtained with a digital handheld power meter. In vacuum, the irradiance would depend only on the area that the light is projected (and therefore only on the NA of the fiber). However, in biological tissues, the irradiance will be affected by the different optical properties of the elements that the light would find on its way, and this cannot be measure experimentally in the cochleae of small animals, as the ones we use in the lab. In the literature the attempts to model the light spread in the cochlea has been limited either to relatively simple analytic calculations (Weiss et al., 2017, 2016) or to 2D simulations (Hernandez et al., 2014; Thompson et al., 2012). Albeit they are useful for preliminary estimates, they fail at addressing the complex cochlear morphology. This led us to work on more realistic models, as the ones presented here, all of which have helped us to estimate two fundamental questions that remain to be difficult to answer from an experimental viewpoint: which is the light irradiance that the neurons exposed to and what is the light profile along the tonotopic axis. In addition, they helped to verify the tonotopic places of the light projected from the optical fiber in the experiment with three fiber positions and to estimate the light profile of a source not yet used before in any experiment. Thus, it can be considered a useful tool to understand and plan our experiments and to explore novel excitation strategies.

In the first model of the gerbil cochlea, the actual position of a fiber was used to position the light emitting surface. Based on the minimum light radiant flux that elicits activity in the primary auditory cortex, we approximated an irradiance threshold value as the irradiance value at a given frequency in which the stimulation with minimum radiant flux was achieved (in terms of cortical activity) (Wrobel et al., 2018). However, it has to be considered that the position of the fiber realized in this model is representative of the one experiment after which the cochlea was subjected to X-Ray tomography and does not reflect the variability of fiber positions inherent to the experiments. Thus, slight displacements of few degrees and/or μm can have a drastic effect in the illumination profile, given the high coherence and relative low NA of an optical fiber. Therefore, these estimated parameters should be considered with caution, since deviations from the true threshold value are possible. Being aware of that, in the model of the gerbil cochlea used to corroborate the experimental position of the fibers, we used average profiles using different angles and positions to obtain more realistic values.

As described in Hernandez et al., 2014, the increase in the size of the stimulation upon increasing the radiant flux of the light source (either with the realistic μLED or with the optical fiber) could be used to increasingly recruit neurons upon sound stimuli of increasing intensity.

For the model of the optical cochlear implant and the marmoset cochlea, we wanted to address not only the light projection along the tonotopic axis, but also to compare the stimulation at the level of the peripheral processes to that at the level of the ganglion. In a translational scenario, the peripheral processes would probably show a more or less severe degeneration (Pfingst et al., 2011). However, since the surviving ones would likely feature AP generation near the organ of Corti, it is relevant for the study of the optogenetic stimulation. This model showed that the spread of excitation was smaller at the level of the peripheral processes, having some effect not only on the frequency resolution but also on the energy requirements of the future optical cochlear implant. It can be hypothesized that this is due to the smaller distance from the emitting surface and the absence of bone in between the emitter and the neuronal structure. There was also a small shift of the excitation maximum along the tonotopic axis for excitation of the peripheral processes vs. the somata in Rosenthal's canal. This spectral shift could be an artifact of our tonotopic projection strategy, and it suggests that a more detailed description of the correspondence of the tonotopic map at the level of the basilar membrane/IHC/peripheral processes with the tonotopic map at the level of the SGN somas is indeed needed, as we further comment on in the discussion section of next chapter. The study of the light spread at the level of the peripheral processes could be also useful for the development of new stimulation paradigms. The length ratio between the Rosenthal´s canal and the basilar membrane in the mouse cochlea was 0.4, meaning that the basilar membrane

is 2.5 fold longer (see Results of next chapter). Adding it to the lower spread of light at the level of the basilar membrane, the achievable frequency resolution at the level of the peripheral processes might be, at least in theory, higher than the one in the ganglion, providing more space for independent stimulation channels. If that was confirmed by experiments, the optical cochlear implant could be complemented with axon regenerative therapies, combining axonal guides and soluble factors, to promote the organized growth of the axon towards the implant, as it has been suggested for the electric cochlear implant (Cai et al., 2016; Mattotti et al., 2015; Pinyon et al., 2019). With a gapless contact between the neuron and the light source, the light interactions with the perilymph and bone would be reduced, decreasing the energy requirements and the light spread, and allowing for a higher number of stimulation channels.

All the models presented here represent an oversimplification of a much more complex system. We reduced the geometric and optical complexity of the cochlea to a 3D reconstruction and only considered the mean optical properties of the three main tissues: perilymph, bone and ganglion. Furthermore, for computational efficiency the number of triangles of the 3D reconstructions had to be reduced (as for example those models used for morphological descriptions) losing some spatial resolution. Even then, to our knowledge, this is the first time that this kind of approaches are used to estimate in 3D the light spread in the cochlea and it seems to be a valid approach. However, to achieve a more realistic picture, the following considerations might be useful to take into account.

One of the main contributors to light absorption in the visible range in biological tissues, is blood, reaching approximated mean values of around $\mu_a = 16$, and $\mu_s = 118.93$ at 473 nm for oxygenated blood with a hematocrit of 45% (Bosschaart et al., 2014). With the cochlea being a well vascularized organ (for some examples see Hoshino and Ishioka, 1982; Jiang et al., 2019 or lectin stainings in the Result section of next chapter), we consider it highly beneficial to include a reconstruction of the cochlear vascular system. The absence of vascular elements in our current model could have led us to 1) overestimate the irradiance values at the Rosenthal´s canal centerline (given the presence of vessels in the medial cochlear wall and inside the ganglion), and 2) overestimate the inter-turn stimulation (which already have shown to be rather limited with our optogenetic approach even at high radiant flux values). The vascular tree could be 3D reconstructed using lightsheet and cochlea clearing with a vessel staining, either for the wall of the vessel (vg. Lectin (see Results of next chapter of this thesis), or other vascular markers, such as CD31 (Lee, 2015)) or the lumen, which has been shown to render a higher segmentation performance (Di Giovanna et al., 2018; Jiang et al., 2019). Other approaches using a contrast agent and other imaging modalities, such as μCT (Zagorchev et al., 2010), could be similarly used.

In the current model, our irradiance values are obtained from a series of query points placed at the centerline of the Rosenthal´s canal and provide an estimation of the light irradiance along the tonotopic axis. The increase in the size of the stimulation upon increasing the radiant flux of the light source (either with the realistic μLED or with the optical fiber) could be used to encode the increasing recruitment of neurons upon sound stimuli of increasing intensity, as described in (Hernandez et al., 2014). Nevertheless, the irradiance across the ganglion in a specific tonotopic region (ie. Along the "intensity" axis (Kawase and Liberman, 2004; Leake and Snyder, 1989; Leake et al., 1992)) remains to be studied. The development of volumetric strategies would help answering that question, although they are extremely computationally expensive and limited to small regions. Approximations using other sets of query points distributed radially to the query points of the centerline could provide a computationally efficient solution, at the cost of reduced spatial resolution as compare to the volumetric model.

CHAPTER II:

ESTABLISHMENT OF A COCHLEAR-ADAPTED CLEARING PROTOCOL, cDISCO, AND DESIGN OF A COMPUTATIONAL PIPELINE FOR ITS ANALYSIS

1. INTRODUCTION

In the previous chapter, I have presented my work on the estimation of the light distribution in the cochlea from a given light source. Knowing how much light irradiates a given cell is critical to estimate its response. However, the neuronal activity upon a given light stimuli is highly dependent to the levels of membrane expression of a given opsin.

In the following chapter, I will present my work related to the evaluation of the transduction efficiency of a viral gene vector in the rodent cochlea, in order to address how the expression of a given opsin takes place along the tonotopic axis. For this purpose, I established and tailored a protocol for clearing and staining the cochlea and a computational pipeline to analyze the transduction levels as a function of the tonotopic position. Along this path, I have screened a number of labelling in different species and used the clearing protocol to quantify SGN and IHCs and map the tonotopic axis.

1.1. TISSUE CLEARING AND LIGHSHEET MICROSCOPY

As I presented in the previous chapter´s introduction, biological tissues contain a mix of elements with different refractive indexes. Lipids and proteins, the dry portion, have an average n_{dry} = 1.5, whereas, the interstitial and intracellular liquids, have an average n_{water} = 1.33. This inhomogeneity of scatterers of high refractive index floating in a low refractive index medium is what make tissues opaque and relatively white, in absence of any pigment or blood (Silvestri et al., 2016).

Here it is important to introduce another concept that of the 'mean free path' (MFP). It is defined as the mean distance between two consecutive scattering events, after which the obtained images becomes blurrier as the photons move away from the source. It is formulated as MFP = $1/\mu_s$ (given that in biological tissues $\mu_s >> \mu_a$). In most biological tissues, the MFP is about 100 μm, which had limited optical sectioning of biological samples to thin slices (e.g. with confocal microscopy) or to superficial layers (e.g. with 2 photon microscopy) (Ntziachristos, 2010).

In 1911, Walter Spalteholz, an anatomist based in Leipzig, found a way to "trick" this phenomenon. He studied the different refractive indexes of anatomical specimens and how to modify them. He embedded the samples in a mix of 5 parts of methyl salicylate with three parts of benzyl benzoate (MSBB), with a refractive index of 1.556, making them transparent after dehydration (Spalteholz, 1911). He was creating what we know today as tissue clearing. Thus, tissue clearing has been in the histology and anatomy toolbox since more than a century, but it was waiting for the right imaging technologies to flourish.

The principle in which most of the Lighsheet microscopes (also known as Single Plane Illumination Microscope) was developed back in 1902 for a completely different problem. An inorganic chemist, Zsigmondy, and a Carl Zeiss physicist, Siedentopf, developed the first ultramicroscope to image gold particles in a solution, using a single plane illumination orthogonally to the acquisition path(Siedentopf and Zsigmondy, 1902). Although it was commercially available, its target market was no other but colloidal chemistry (Keller and Dodt, 2012). It was not until the pioneer work of Voie et al. in 1993 that the lightsheet microscopy met biology (Voie et al., 1993). Voie and colleagues combined the method developed by Spalteholz with a microscope that used the same principle as the one of Zsigmondy and Siedentopf to image the cochlea of the guinea pig and even achieved a very coarse reconstruction of the scala tympani and some associated structures. Some years later, Huisken et al. set of the starting point of what would be termed the lightsheet revolution (Huisken et al., 2004). They combined the same principle as Voie with the rotation of the specimen (fixed and live transgenic Medaka fish embryos expressing GFP, embedded in agarose) to generate a multiview reconstruction of the sample. Nowadays, we can found a humungous variety of strategies to image big specimens (either naturally transparents or cleared), with sophisticated techniques of beam shaping to increase the resolution (see (Power and Huisken, 2017) for a detailed and extensive overview), although they are custom made and normally not easily available. Thus, one of the most used commercial solutions, as LaVision Ultramicroscope II, is based in the simple principle applied by Voie with some improvements

in the illumination and acquisition aspect (including double side illumination or dynamic horizontal focus).

After the work of Voie et al, there were investigations using the method developed by Spalteholz or slight modifications of it (e.g. using Benzyl Alcohol instead of Methyl Salicylate (Dodt et al., 2007; Jährling et al., 2009). The method did not evolve very much up until 2011 with the publication of the Scale paper (Hama et al., 2011) and its most mediatic peak after the work of Karl Deisseroth and his CLARITY method in 2013 (Chung et al., 2013). These advances came from the need of imaging fluorescent proteins natively in their tissue context. During these years, a vast variety of different methods and protocol has thrived, tailored to the particular needs of every experimental setting. In general terms, we could split the clearing methods in four big groups, according to the nature of the clearing procedure in which they are based on: Organic Solvents, High refractive index aqueous solution, Hyperhydration methods, and Tissue transformation. Some of the techniques, under this classification, are summarized in **Figure 10** (Richardson and Lichtman, 2015; Silvestri et al., 2016).

The family of the high refractive index solution were developed in order to extend the analysis of endogenous fluorescence of GFP. They are based on hydrophilic solution, which are better suited to keep the structure of the fluorescent proteins and therefore its fluorescence. Generally, the refractive index matching solution have a refractive index around 1.42 – 1.48. In our pilot experiments, we briefly assess the usability of the SeeDB protocol (Ke et al., 2013), which uses a high concentration of sucrose in its solution, but did not display a good performance in lightsheet imaging of the cochlea.

The group of using hyperhydrating solutions combine mild lipid removal with a polyalcohol (e.g. glycerol) and a detergent (e.g. Triton X-100) with hyperhydrating the proteins components with urea, resulting in a refractive index of 1.38 (Hama et al., 2011). We also initially tested the ScaleS (Hama et al., 2015) method, that use sorbitol as the polyalcohol, but the results were far from being what we need.

The most known family probably is the one of the tissue transformation. CLARITY belongs to it, since it based on crosslinking the proteinaceous content of the tissue with a polymerized hydrogel, creating a gel-tissue hybrid, and removing the lipids with a very strong detergent, such as SDS, that could be accelerated with an electrophoretic chamber (Tomer et al., 2014).

The techniques using organic solvents are based on the substitution of water by an organic solvent to reduce the refractive index mismatch. The most commonly used in auditory research (see below) is the Spalteholz´s fluid, following ethanol dehydration. Nevertheless, the protocol

that we will used along this chapter is a modification of the original iDISCO+ (Renier et al., 2016). The cochlea-adapted iDisco+, that we take the freedom of naming it cDisco, displayed an outstanding performance, and therefore for its robustness, easiness and inexpensively is the chosen one. It uses methanol for dehydration and dibenzylether, with a refractive index of 1.56, as a clearing solution.

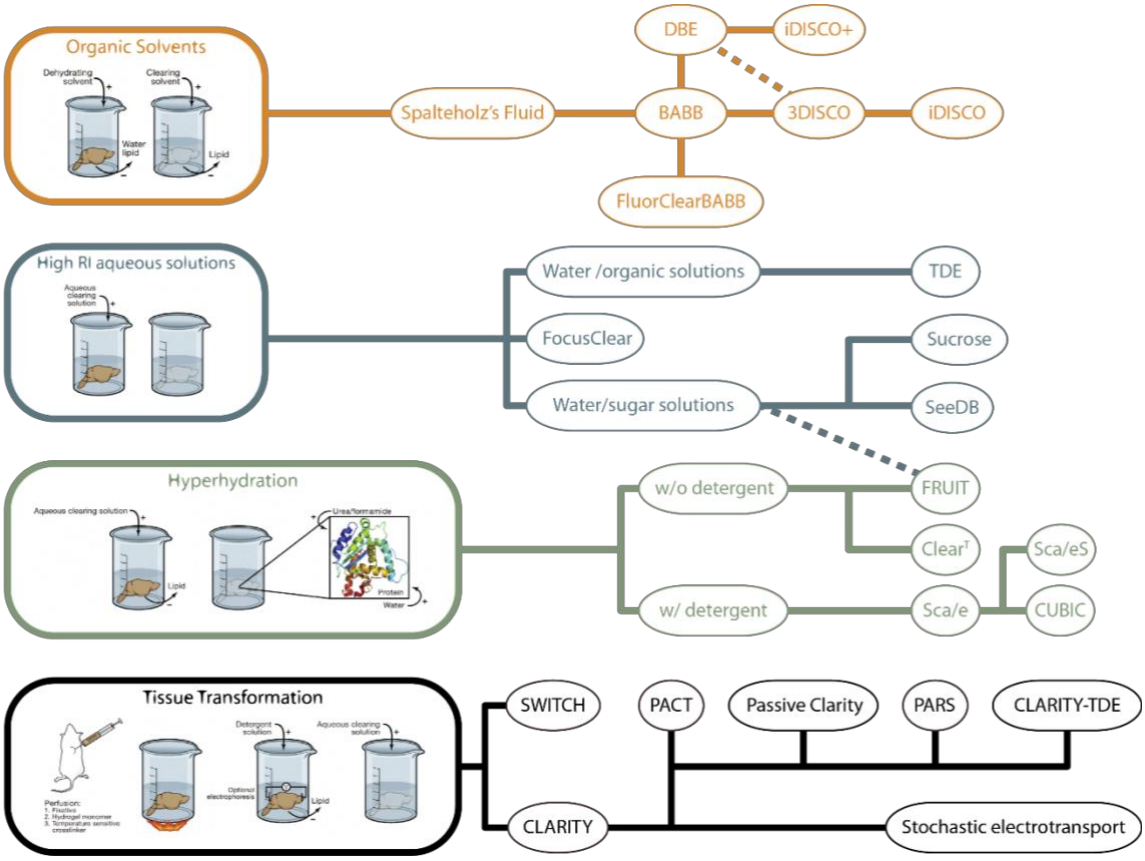

Figure 10. Tissue clearing techniques. Some examples of tissue clearing techniques classified according to their clearing principle. Modified after (Richardson and Lichtman, 2015; Silvestri et al., 2016).

1.2. TISSUE CLEARING AND THE COCHLEA

More than four centuries have passed, since the early descriptions of the inner ear by Andreas Vesalius, Bartolome Eustachi and Galen were picturing the inner ear filled with a type of purified air, "aer ingenitus" (Water, 2012). During all this time, the inner ear has become a living yearbook of the anatomist community. Profesor Cotugno termed "liquor Cotunni" what we know today as perilymph in 1775. Some years later, Professor Antonio Scarpa named the endolymph and the peripheral ganglion of the vestibular system as the Scarpa´s fluid and ganglion, respectively. Before committing to the noble life after the death of his father, the

Marquis Alphonse Corti, later Baron Corti, published the first histological description of the hearing epithelium in 1851, which later his mentor, Professor Kölliker from Wurzburg, would name the organ of Corti, containing the rods of Corti (currently known as pillar cells) and the tunnel of Corti. His work was followed up by a series of professors that described many cells and spaces in the cochlea and named after themselves: Dieters, Claudius, Hensen, Boetstscher, Nuel and Huscke (for a historical review of the inner ear histology and anatomy, see Water, 2012).

All these anatomists, and many others, contributed to the description of one of the most elegant and still intriguing organs of the human body, the inner ear and specially the cochlea. Until the advent of the of computerized techniques such as CT or MRI in the seventies, most description were limited to exquisite anatomic dissections, to describe the coarse structure of the tissue, or to histological physical sections of different thicknesses, if cellular resolution was needed.

It was not until the work of Voie in 1993, that both preparations and aims could start to merge since it orthogonal-plane fluorescence optical sectioning microscopy (OPFOS) imaging allowed to image a whole intact cochlea and achieving even cellular resolution.

After the work of (Voie et al., 1993), it seems that the cochlea clearing have not flourished in the auditory field. To my knowledge, in these almost 30 years, only 27 papers have used this technique with little or none modifications to the initials protocols. A summary of these efforts is presented in **Table 4**. Together with the axial resolution limitations inherent to the imaging technology, some of the reasons might be 1) the lack of a robust screening of antibodies, 2) the lack of an accessible, standardized, easy-to-implement analysis workflow, 3) the use of highly toxic reagents (such as BABB or MSBB, whose damages to the imaging setup are not covered by the product warranty, for example, of LaVision Ultramiscope II), 4) the lack of access to a lightsheet microscope.

Given than our estimates of transduction efficiency in our previous papers on cochlear optogenetics were based on cryosections, only a very rough location classification could be done in Apical, Mid and Basal turn. In order to increase our spatial resolution and to comprehensively study the transduction levels as a function of the tonotopy position, we wanted to have a method that would allow us to study the expression levels of GFP in the whole-intact cochlea. Given the lack of such studies in the literature, we had to gather parts of different protocols to engineer an adaptation of iDisco+ and to create an image analysis workflow that would allow retrieving numerical data from the image stacks. Since this kind of tool will not only be useful for studying the tonotopic distribution of the expression of GFP in mouse, we also screened its compatibility with other stainings and with other species.

Table 4. Cochlea clearing in the literature

Publication	Clearing method	Staining	Imaging method	Specie	Analysis	Comment
Voie et al., 1993	MSBB	RITC	OPFOS	Guinea Pig	Rough reconstruction of ST	First use of OPFOS with biological specimens
Voie and Spelman, 1995	MSBB	RITC	OPFOS	Guinea Pig	Rough reconstruction of ST, CA, RWM	-
Voie, 2002	MSBB	RITC	OPFOS	Guinea Pig	-	Whole inner ear was imaged
Valk et al., 2005	MSBB	RITC	OPFOS	Guinea Pig	-	Study of scala media, by injecting polystyrene spheres
Buytaert and Dirckx, 2007	MSBB	RITC	HR-OPFOS	Gerbil	Reconstruction of stapes and adjacent soft tissue	Development of HR-OPFOS
Hofman et al., 2008	MSBB	RITC	OPFOS	Guinea Pig	3D reconstruction of the utriculo-endolymphatic (Bast´s) valve	-
MacDonald and Rubel, 2008	MSBB	Primary Ab: PV, NF200, Acetylated Tubulin; DNA: DAPI, TO-PRO-3	LCSM	Mouse	-	Comparison with Spurr's Resin Hardie et al., 2004)
Santi et al., 2008	MSBB	Autoflourescence, RITC	OPFOS	Mouse	3D reconstruction of cochlear structures	Development of the Mouse Cochlear Database
Buytaert and Dirckx, 2009	MSBB	RITC	HR-OPFOS	Gerbil	Reconstruction of stapes and adjacent soft tissue	-
Hofman et al., 2009	MSBB	RITC	OPFOS	Guinea Pig	3D reconstruction of inner ear	Comparison with serial histological slices
Santi et al., 2009	MSBB	Autoflourescence, RITC	TSLIM	Mouse	3D reconstruction of inner ear	Development of TSLIM
MacDonald and Rubel, 2010	MSBB	Primary Ab: PV, NF200, DNA: DAPI	LCSM	Mouse	-	-
Johnson et al., 2011	MSBB	RITC	TSLIM	Mouse	3D reconstruction of cochlear structures; SGN manual counting	Cochlear morphometry; SGN count/density vs BM length;
Kopecky et al., 2011	MSBB	RITC	TSLIM	Mouse	3D reconstruction of cochlear structures	Comparison with N-Myc CKO: Cochlear morphometry
Pan et al., 2011	MSBB	RITC	TSLIM	Mouse	3D reconstruction of cochlear structures	Comparison with Atoh1 CKO: Cochlear morphometry
Buytaert et al., 2011	MSBB	RITC	OPFOS	Gerbil	3D reconstruction of inner ear	Comparison with µCT; cochlear morphometry
Kopecky et al., 2012b	MSBB	RITC	LCSM	Mouse	3D reconstruction of cochlear structures	Protocol for sample preparation, imaging and analysis
Schröter et al., 2012	MSBB	RITC	sTSLIM	Mouse	-	Development of sTSLIM
Kopecky et al., 2012a	MSBB	RITC	sTSLIM and TSLIM	Mouse	3D reconstruction of inner ear	Cochlear morphometry during development
Buytaert et al., 2013	MSBB	RITC	sTSLIM	Mouse	3D reconstruction of cochlear structures	Comparison with µCT; cochlear morphometry
Wrzeszcz et al., 2013	MSBB	Autoflourescence	LCSM	Guinea Pig	SGN density counts per mm_2;manually + ICTN plug in)	Comparison with paraffin embedded slices
Schmitz et al., 2014	MSBB	RITC, Primary Ab: Myo6a	sTSLIM	Mouse	Manual counting of IHC and SGN	Comparison with Kanamycin-Furosemide ototoxicity model
Johnson et al., 2014	MSBB	RITC	sTSLIM	Human	3D reconstruction of cochlear structures	Comparison with celloidin slices traditional histology)
Risoud et al., 2017	MSBB	Primary Ab: NF200; DNA: DAPI; Actin: Phalloidin-TRITC	LCSM	Gerbil	IHC and OHC density	-
Tinne et al., 2017	MSBB	Extinction and Autofluorescence	SLOT	Human	-	Comparison with µCT; Imaging with cochlear implant
Nolte et al., 2017	MSBB	Primary: NF200, OTOF	SLOT	Mouse	Reconstruction of neurofilament labeling	Measurement of the curvature radius along the BM lenght
Schulze et al., 2019	MSBB	Primary Ab: NF200	SLOT	Mouse	Screen for structural changes to further investigate with other techniques	Comparison with $Ca_v1.3_{-/-}$ mice
This work, 2019	DBE	Primary Ab: PV, Calr, vGlut3, GFP; DNA: 7-AAD; Vessel: Lectin	Ultramicroscope	Mouse, Rat, Gerbil, Marmoset	SGN and IHC counting, GFP distribution, tonotopy mapping	-

OPFOS: Orthogonal-plane fluorescence optical sectioning; MSBB: Methyl Salicylate Benzyl Benzoate Spalteholz's fluid; RITC: Rhodamine-B isothiocyanate; ST: Scala Tympani, CA: Cochear Aqueduct, RW: Round Window; BM: Basilar membranesTSLIM: scanning Thin-Sheet Laser Imaging Microscopy; SLOT: Scanning Laser Optical Tomography; LCSM: Laser Confocal Scanning Microscopy; Ab: Antibody for details on the concentration and manufacturer information of the antibody, see original publication

2. METHODS

2.1. COCHLEA-ADAPTED TISSUE CLEARING PROTOCOL, CDISCO

The following clearing protocol is an adaptation of the iDISCO+ (Renier et al., 2016) to the cochlea (cDISCO). It can be separated in four parts: Tissue Pre-Processing, Immunostaining, and Clearing. In **Figure 11** can be appreciated the result from the first step to the last. In section d. Solutions, a detailed description of the solutions used can be found.

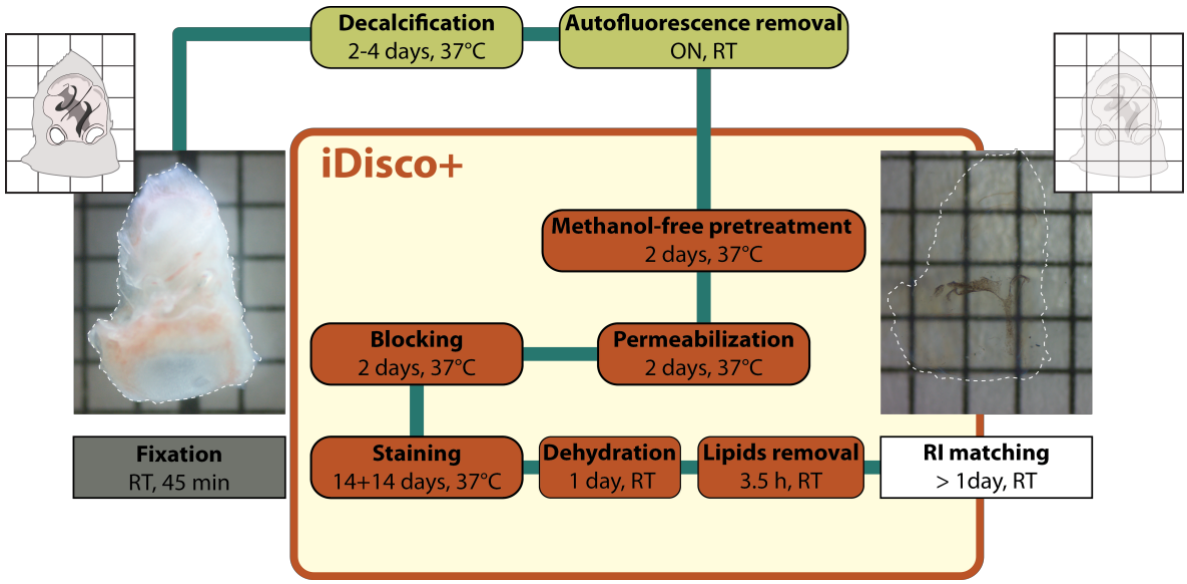

Figure 11. Cochlea-adapted clearing protocol, cDisco. After harvesting, cochlea are fixed in 4% PFA to continue the immunostaining and finishing with the clearing process. The transparency of the tissue can be appreciated in the right most panel, only disturbed by the presence of the pigmented epithelium of the vestibular system.

2.1.1. TISSUE PRE-PROCESSING

Animals were then kept in a 12 h light/dark cycle, with access to food and water ad libitum. Animals (mice, gerbils and rats of different ages) were euthanized by CO_2 inhalation and cochleae were removed in PBS. The stapes were removed and a small hole was done in the apex, in order to allow the free flow of liquid inside the cochlear compartments. The cochleae were fixed with 4% PFA, at room temperature for 30-45 minutes. Afterwards, they were decalcified in 10% EDTA until they showed enough decalcification evaluated by pressing the

sample and optically appreciating an elastic blending of the cochlear walls. At least, this process was taking 2 days at room temperature (RT) or overnight (ON) at 37°C under constant shaking, although it is recommendable to extend it up to 4 days with two exchanges of EDTA to ensure an excellent decalcification.

For marmosets, the temporal bones were dissected by veterinarians in the Deutsches Primate Zentrum and immersed in 4% PFA. After a variable amount of time, but no less than one hour, the temporal bones arrived to our lab and were roughly dissected by Dr. Vladan Ranković or Dr. Marcus Jeschke. Then, they were incubated in 10% EDTA with two-three changes per week, during two-three months.

For transduced mice cochleae, the animals were injected in the Scala tympani at p5-6 through the round window by Christiane Senger-Freitag or Dr. Vladan Ranković and were sacrificed at p14 or 3 months. The viral vector based on AAV-PHP.B serotype contained the sequence of fast-Chrimson-EYFP under the hSyn promoter.

Afterwards, given the high vascularization of the cochleae, the cochleae were incubated in 25% N,N,N′,N′-Tetrakis(2-Hydroxypropyl)ethylenediamine solution (for a description of the solutions, see below) until the remaining of blood were decolored (1-2 days, (Greenbaum et al., 2017)). The methanol-free pretreatment from the original iDisco+ protocol (Renier et al., 2016) continued. The samples were washed two times in *PTx.2*, 1 hour, at RT, under continuous shaking, then incubated in the *solution 1b and 2b* consecutively, over night, at 37°C, under continuous shaking, and finally washed again in *PTx.2.*

2.1.2. IMMUNOSTAINING

All the following steps were done at 37°C degrees under constant shaking.

The cochleae were incubated firstly, in *Permeabilization solution* for 2 days, secondly in *Blocking solution* for 2 days, thirdly in the *Primary Antibody solution* and fourthly in the *Secondary Antibody solution*, both steps for two weeks.

After every antibody solution incubation, samples were washed 4-5 times during one day in *PtwH solution*.

2.1.3. Clearing

Following immunostaining, samples were dehydrated in an increasing methanol series (20, 40, 60, 80 and 100%), 1 h each and delidipified first in 66% dichloromethane/33% methanol for 3h, and then 2 times in 100% dichloromethane for 15 minutes each. These steps were performed at RT, under continuous shaking. Finally, the samples were stored in dibenzylether (DBE), as a refractive index matching solution.

2.1.4. Solutions

Decalcification solution: 10% EDTA in PBS, pH 8

Reagent	Concentration	Manufacturer
Ethylenediaminetetracetic acid tetrasodium salt dihydrate (ED4SS)	10%	Sigma-Aldrich
Phosphate buffer saline, tablets (P4417)	1x	Sigma-Aldrich

Endogenous fluorescence removal solution: 25% N,N,N′,N′-Tetrakis(2-Hydroxypropyl) ethylenediamine in PBS

Reagent	Concentration	Manufacturer
N,N,N′,N′-Tetrakis(2-Hydroxypropyl)ethylenediamine (L16280)	25%	Alfa-Aesar
Phosphate buffer saline, tablets (P4417)	1x	Sigma-Aldrich

Methanol-free pretreatment (from iDISCO+):

PTx.2 solution

Reagent	Concentration	Manufacturer
Triton X-100 (648462)	2 %	Millipore
Phosphate buffer saline, tablets (P4417)	1x	Sigma-Aldrich

Solution 1B: 0.2% Triton X-100/20% DMSO in PBS

Reagent	Concentration	Manufacturer
Triton X-100 (648462)	2 %	Millipore
Dimethylsulfoxide (A994.1)	20%	Carl Roth
Phosphate buffer saline, tablets (P4417)	1x	Sigma-Aldrich

Solution 2b: 0.1% Triton X-100/20% DMSO/0.1% Tween-20/0.1% Deoxycholate/0.1% IGEPAL CA-630 in PBS

Reagent	Concentration	Manufacturer
Triton X-100 (648462)	0.1 %	Millipore
Dimethylsulfoxide (A994.1)	20%	Carl Roth
Tween-20 (A4974)	0.1%	ITW reagents
Sodium Deoxycholate (D6750)	0.1%	Sigma-Aldrich
IGEPAL CA-630 (I8896)	0.1%	Sigma-Aldrich
Phosphate buffer saline, tablets (P4417)	1x	Sigma-Aldrich

Immunostaining solutions :

Permeabilization solution (0.16%TritonX-100/20%DMSO/2.3% Glycine (0.3M) in PBS

Reagent	Concentration	Manufacturer
Glycine (G7126)	2.3 % (0.3M)	Millipore
Dimethylsulfoxide (A994.1)	20%	Carl Roth
PTx.2	-	-

Blocking solution

Reagent	Concentration	Manufacturer
Normal Goat Serum (S26)	6%	Millipore
Dimethylsulfoxide (A994.1)	10%	Carl Roth
PTx.2	-	-

PTwH, 0.2% Tween-20/0.001% Heparin in PBS

Reagent	Concentration	Manufacturer
Tween-20(A4974)	0.2%	ITW reagents
Heparin sodium salt from porcine intestinal mucosa (H3393)	0.01%	Sigma Aldrich
PTx.2	-	-

Heparin was added from a 10 mg/ml Heparin stock solution.

Primary antibody solution

Reagent	Concentration	Manufacturer
Normal Goat Serum (S26)	3%	Millipore
Dimethylsulfoxide (A994.1)	5%	Carl Roth
PTwH	-	-

Secondary antibody solution

Reagent	Concentration	Manufacturer
Normal Goat Serum (S26)	3%	Millipore
PTwH	-	-

Clearing Solutions

Dehydration

Reagent	Concentration	Manufacturer
Methanol ROTISOLV® HPLC (P717.1)	20, 40, 60, 80, 100%	Carl Roth, ROTISOLV
ddH_2O	-	-

Lipid extraction solutions

Reagent	Concentration	Manufacturer
Methanol ROTISOLV® HPLC (P717.1)	33%	Carl Roth, ROTISOLV
Dichloromethane (270997)	66%, 100%	Sigma Aldrich

Refractive Index matching solution

Reagent	Concentration	Manufacturer
Dibenzyl Ether (33630)	-	Sigma Aldrich

2.1.5. ANTIBODIES AND DYES LIST

Primary antibodies

Manufacturer	Antibody	Host	Concentration	Target	Animal tested
Synaptic Systems	Parvalbumin, polyclonal antiserum (195 004)	Guinea Pig	1:300	IHC, SGN	Mouse, Gerbil, Marmoset, Rat
Swant	Calretinin, polyclonal antiserum (7697)	Rabbit	1:300	IHC, subtypes SGN	Mouse, (Gerbil), Marmoset
Synaptic Systems	Calretinin polyclonal, IgY fraction (214 106)	Chicken	1:300	IHC, subtypes SGN	Gerbil
Synaptic Systems	vGlut3 polyclonal, affinity purified (135 203)	Rabbit	1:300	IHC	Mouse, Gerbil
Abcam	GFP polyclonal (ab13970)	Chicken	1:400*	GFP-expressing cells	Mouse (transduced), Rat (transgenic)

* If high expression levels are expected, I recommend using a higher concentration (see Discussion)

Secondary antibodies

Manufacturer	Antibody	Host	Concentration	Animal tested
Invitrogen	Anti-Guinea Pig 488, IgG (H+L) Highly Cross-Adsorbed Secondary Antibody, Alexa Fluor 488, A11073 ,3	Goat	1:500	Gerbil
Invitrogen	Anti-Guinea Pig 568 IgG (H+L) Highly Cross-Adsorbed,Polyclonal (A11075, 16)	Goat	1:500	Gerbil, Mouse
Invitrogen	Anti-Rabbit 568, IgG (H+L) Cross-Adsorbed, polyclonal (A11011)	Goat	1:500	Marmoset
Invitrogen	Anti-Rabbit 633, IgG (H+L) Cross-Adsorbed polyclonal (A21070, 6)	Goat	1:500	Gerbil, Mouse,
Invitrogen	Anti-Rabbit 647, IgG (H+L) Cross-Adsorbed polyclonal (A-21244, 6)	Goat	1:500	Gerbil
Invitrogen	Anti-Chicken 488 IgG (H+L) polyclonal (A11039, 27)	Goat	1:500	Mouse, Rat
Invitrogen	Anti-Mouse 488 IgG (H+L) Cross-Adsorbed Secondary Antibody, polyclonal A-11001	Goat	1:500	Marmoset

Dyes

Manufacturer	Name	Concentration	Target	Animal tested
Vector Laboratories	Dylight 594 Griffonia (Bandeiraea) Simplifolia Lectin I, isolectin B4 (DL-1207)*	1:200	Glycoproteins in vasculature	Mouse, Gerbil
Invitrogen	7-AAD	1:1000	Nuclei(DNA)	Gerbil

*kindly provided by Alejandro Restrepo, from Dr. Klaus-Armin Nave's lab (MPI for Experimental Medicine, Göttingen)

2.1.6. EXPLORING THE USE OF NANOBODIES IN CDISCO

In order to investigate the possibility of using a premix of primary antibodies and nanobodies, instead of subsequent incubation of primary and secondary antibodies, to reduce the incubation time of the protocol, we started a collaboration with Shama Sograte-Idrissi from Dr. Felipe Opazo´s lab (UMG, Göttingen). They provide us with nanobodies to carry out a pilot experiment for which the following changes were done:

The primary antibody (guinea pig antiserum anti-Parvalbumin, 195 004, Synaptic Systems) was premixed with the secondary nanobody (Nanobody anti-guinea pig Alexa 546, NanoTag Biotechnologies GmbH, fluorophore-coupled by Shama Sograte-Idrissi) using a molar ratio of 1:3 (3.3 µl of antibody (1mg/ml) plus 13.47 µl of nanobody (5µM), for 1ml solution) for 45 min, under constant rotation, at RT.

The antibody solutions contained 1.5% Bovine Serum Albumin (A7030, Sigma-Aldrich) instead of 6% Normal Goat Serum.

The primary antibody premixed with the secondary nanobodies were diluted in the same solution as the secondary antibodies.

The samples were incubated in 4 different ways (37°C, under shaking): 1) 6 days and 2) 14 days in the solution containing the primary antibody premixed with the secondary, 3) 3 days and 4) 7 days with the primary followed by a washing step of 1 day in PTwH at RT and the incubation of the secondary antibody for 3 and 7 days, respectively.

2.2. IMAGE ACQUISITION

All the light-sheet images were acquired with an Ultramicroscope II (LaVision Biotec), equipped with a white laser (super continuum) and a 2x objective with a dipping cap corrected for DBE. All the samples were imaged in DBE. Cochleae were glued to a custom-made epoxy block or glued to a magnet and then fixed to a custom-made holder. Laser intensities, sheet width and sheet NA were adapted to every cochlea, and kept consistent for each experiment.

For the nanobodies experiments, the samples were imaged between 2 and 10 days after the last cDISCO step. The laser power was constant for all the samples except for the sample incubated with primary and secondary antibody for 14 days, where it was chosen 6.75 times lower (2% vs. 13.5%). The stacks were acquired with a total zoom of 8x (2x Objective and 4x Optic Zoom microscope body), a step size of 3 µm, with a lightsheet of 30% width and a thickness of 5µm (NA: 0.148, unidirectional illumination and 11-12 steps of dynamic horizontal focus.

2.3. IMAGE ANALYSIS

2.3.1. MISCELLANEOUS

Maximal Intensity Projections (MIP) were done in FIJI (Schindelin et al., 2012). The look-up tables applied were either mpl-viridis, mpl-magma or the bone colormap (exported from Matlab). MIPs and exemplary slices were converted to RGB color and save as .tif files.

For the colormap of the tonotopic axis, the spectral colormap of the *Brewermap* function (Cobeldick, 2018), based on the color schemes designed by (Brewer, 2014).

2.3.2. INNER HAIR CELL QUANTIFICATION

The inner hair cells were optically detected and manually annotated using the point tool and the ROI manager of FIJI.

2.3.3. SPIRAL GANGLION NEURON DETECTION

2.3.3.1. PREPROCESSING

The original stack was 3D cropped, and the ganglion was manually segmented with TrakEM2 (Cardona et al., 2012). Then, to improve the sphericity of the cells (Töpperwien, personal communication) along the Z-axis and to reduce the image size, it was downsampled by a factor of 0.5x0.5x2.

Given the different intensity levels across cells, each dataset was separated in two independent datasets corresponding to high intensity pixels and medium intensity pixels (below which only background pixels remained). To do that, after defining thresholds for each, the following steps were carried out for each intensity subdataset slices by slices:

1) Get indexes of pixels above threshold and generate a binary mask
2) Dilate mask using a square structuring element of 2x2 pixels
3) Apply a median 2D filter of 5x5 pixels to the mask
4) Array multiply mask by frame
5) Apply Contrast-limited adaptive histogram equalization (CLAHE) to the resulting image (mask*raw frame) using the Matlab function *adapthisteq* and its default parameters

The resulting image stack was normalized as follows:

$$I_{norm}(x,y,z) = \frac{I(x,y,z) - I_{min}}{I_{max} - I_{min}}$$

To find the parameters for the 3D Hough Transform, only a small substack in the range of approximately 100x100x100 pixels for each of the intensity subdatasets was used.

2.3.3.2. 3D HOUGH TRANSFORM

Initially patented by Paul V. C. Hough (Hough, 1962), the genuine algorithm was developed to recognize complex patterns in pictorial representations of the tracks left by charged subatomic particles in the bubble chamber. The algorithm used in this work was provided by Dr. Mareike Töpperwein, from Prof. Dr. Tim Salditt´s lab (Institute of X-ray Physics, Göttingen), who

modified it and used it quantify the number of cells in biopsies from human cerebellum using phase-contrast X-ray tomography (Töpperwien et al., 2018). It was originally described by (Peng et al., 2007) in 2D to detect XY coordinates of spheres and implemented in Matlab as a File Exchange submission entitled "Spherical Hough Transform for 3D images" (Xie, 2014). Then, I developed a graphical user interface (GUI) (**Figure 12**) to facilitate the task of finding the parameters needed. The Hough transform used here relies on the calculation of the likelihood of a given pixel to be the center of an approximated sphere of a given radius. Although, the technical formulation of the algorithm is out of the scope of this thesis, the steps are briefly described in 2D as follows (the application to a 3D image is analogous):

Step 1) Define the parameters:

- ***Radius Range***: Minimum and maximum radii expected
- ***Gradient threshold***: Minimum value of the gradient array in which the following calculations will be performed
- ***Filter Radius***: Radius of the filter used for local maxima search in the accumulation array (vg. 3 for symmetrically spherical objects)
- ***Multi-Radius detection threshold***: Tolerance of picking up the likely radii values (if 1, only the principal will be picked up)
- ***Minimum Pixel Intensity at the object center***: Pixel intensity value in the original image above which the center will be accepted.
- ***Accumulation array threshold***: Threshold value above which local maxima will be detected as cell centers.

Step 2) Calculation of the gradient array:

$$VI(i, j) = (Vx, Vy)|(i,j) = (I(i,j)-I(i, j-1), I(i,j)-I(i-1, j))$$

where (i, j) are the pixel indices, VI(i,j) is the gradient vector at pixel (i,j) and I is the intensity at that given position. The pixels were the magnitude of the vector VI(i,j) correspond to the edge of the detected cell. Given it spherical nature, the VI(i, j) will be always pointing towards the center of the sphere or right on the opposite direction – a feature that is exploited in the step 3 (Peng et al., 2007).

Step 3) Calculation of the accumulation array: For all those pixels above the gradient threshold value, a weight value is added in a new array. If a given pixel falls in a line segment of the length defined by the radius range along the gradient vector, it receives a vote. Those pixels with higher number of votes will have a higher intensity in the

accumulation array and therefore a higher probability of the pixel of being the center of a sphere.

Step 4) Peak detection of the accumulation array: Local maxima, higher than the threshold value defined for the accumulation array, are detected using a Laplacian of Gaussian filter and accepted if the pixel intensity of the original image is above the minimum pixel intensity at the object center defined in Step 1.

If the parameters used were detecting a correct estimate of the number of cells, they were stored. Then, they were applied to the whole 3D stack. The script provided by Dr. Mareike Töpperwien separated the whole image stack into substacks to increase the computational efficiency of the whole analysis following the parameter finding. Once one intensity subdataset was complete, the following went through the same process.

Finally, the centers detected were curated, that is, all those cells with a radius estimated of 0 and all double entries (found by measuring the distance between the centers and selecting those which where closer than 2*(min(radius)-1.5)) were removed.

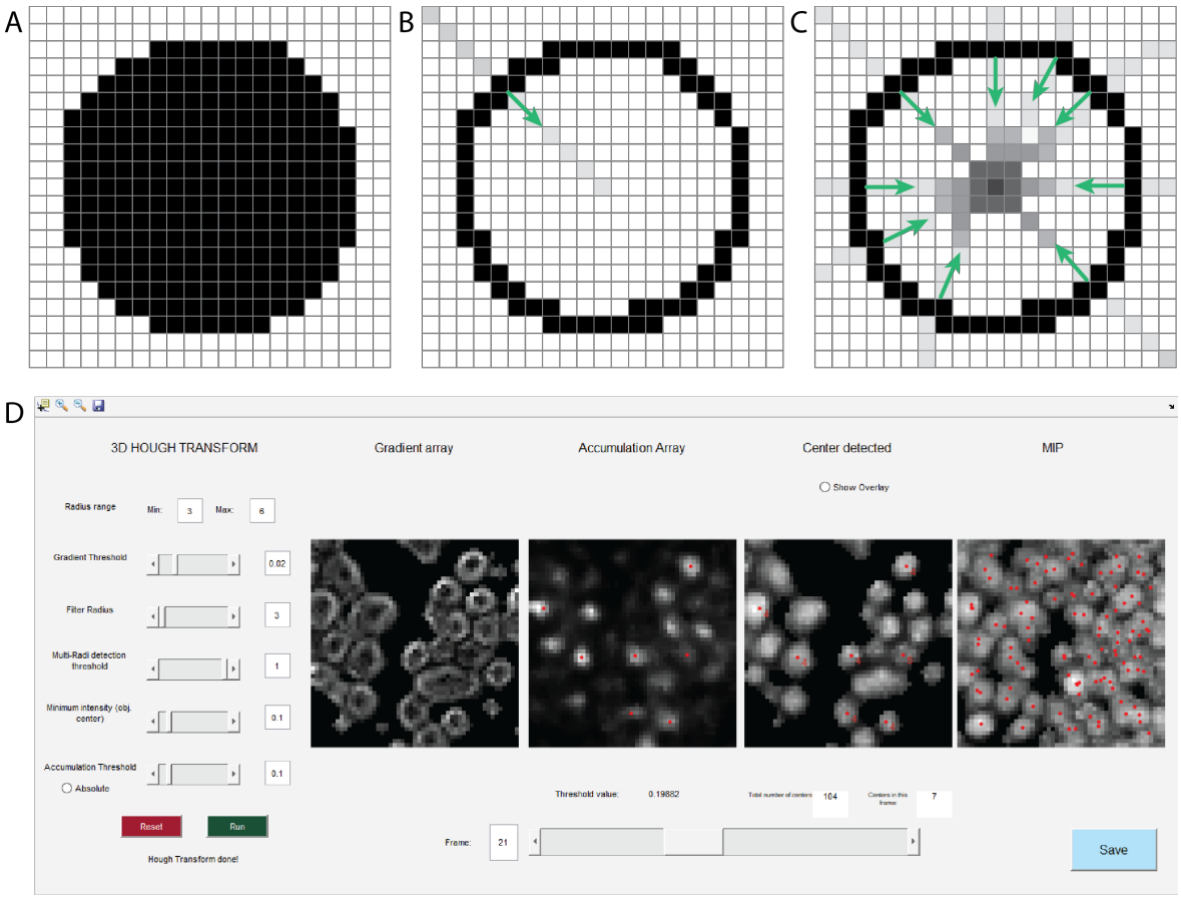

Figure 12. Hough transform: principle and user interface for parameter finding. A. Schematic representation of a cell in 2D pixel array from a raw image. **B.** the calculated gradient image displays the edge of the cell after applying a threshold. A line segment, with a length equal to the maximum diameter expected, is placed along the

gradient vector starting at the edge of cell. **C.** The accumulation array: after sequential placement of the segments lines along the gradient vectors, a maximal number of segments will intersect in the center of the sphere, resulting in a higher number of votes and therefore a higher pixel value. Panel a, b and c have been adapted from (Töpperwien, 2018). **D.** GUI used for initial parameter finding. In the left hand side, the user can enter and modify the following values (see text for a more detailed description): radius range, gradient threshold, filter radius, multi-radii detection threshold, minimum object intensity, and accumulation threshold (both as a relative value, in percentage of the maximum, or as an absolute value). The gradient and accumulation images and the raw image with the center detected are depicted in the following frames. The user can navigate through the whole stack using the slider and save the results in a .mat file. The maximal intensity projection with all the cells detected can be appreciate in the right-most frame.

2.3.3.3. ERROR QUANTIFICATION

In order to assess the error of the cell detection algorithm, three substacks of 100x100x25 pixels were defined for each dataset. In a GUI designed to facilitate the task (**Figure 13**), each of the subvolumes was imported together with the coordinates detected within the range of the substack. There, each cell detected was classified as true cell (true positive, TP) or false cell (false positive, FP) or cell that was not detected (false negative, FN).

Precision, recall and their harmonic mean (F1 score) were used as performance metrics to quantify the error of the routine and are described as follows:

$$p = \frac{TP}{TP + FP}$$

$$r = \frac{TP}{TP + FN}$$

$$F1\ score = \frac{2 * (p * r)}{p + r}$$

These parameters come from the information retrieval field and were initially implemented to describe how an information retrieval system returns the relevant document to the user (Sammut and Webb, 2017). If we consider the confusion matrix terminology, we can substitute relevant and non-relevant documents retrieved, for True or False Positive (TP or FP), total of documents retrieved for (TP + FP), and total of relevant documents in the database for (TP+FN). The F1-score is the harmonic mean of both precision and recall and is used to measure the accuracy of binary predictions in classification problems.

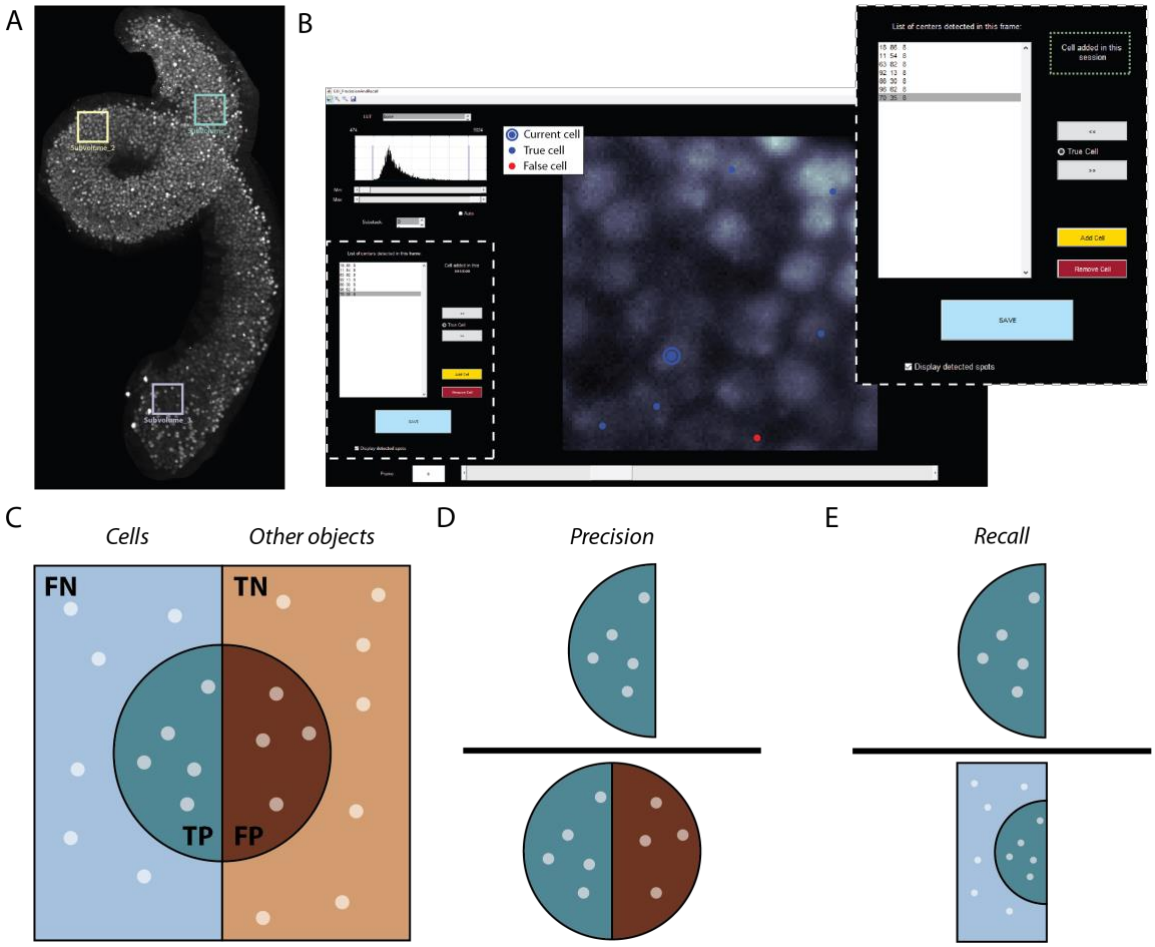

Figure 13. GUI for error quantification and graphical representation of error. A. MIP of the segmented ganglion with the subvolumes (100x100x25 pixels) selected for the error quantification (color squares). **B.** GUI and a close up of the specific module for error estimation: The GUI allows to explore all the cells detected in a given ROI (either by clicking on a given cell or using the arrows) and label them as true or no-true cells (true positive or false positive – using the push button between the left and right arrows on the right side of the coordinate list). It also allows to add non detected cells (false negatives – dotted green line delimit the message area where we can see if the cell was added manually). Finally, the output can be saved and imported to Matlab to quantify both precision and recall errors and their harmonic mean (F1 score). **C-E,** Graphical representation of precision and recall error. Pixel "blobs" are represented as white circles. Those corresponding to cells are inside the blue shapes, where as those corresponding to something else inside the brown ones. Darker shapes depict the blobs detected as cells. FN, false negatives; TP, true positives; TN, true negatives; FP, false positives.

2.3.4. TONOTOPIC CLASSIFICATION

2.3.4.1. TONOTOPIC AXIS DEFINITION

To define the tonotopic axis, first, I registered consecutive coordinates from apex to base at the level of the inner hair cells. Then, these coordinates were imported to Matlab and 1000 points were interpolated using spline interpolation by the Matlab function *interp1*. The frequencies label were created by fitting a Greenwood´s function (Greenwood, 1961, 1990):

$$f = A(10^{\alpha x} - k)$$

being f is the tonotopic label in Hz; A is a scale factor, that shifts the whole function along the log-frequency axis; α, constant that describes the steepness of the function in a logarithmic scale, which corresponds to the gradient of high-frequency end of the map; x is the normalized distance from apex [0-1] and k is a constant that accounts for the warp of the function and its seems to describe how much spatial compression occurs towards the low frequency locations (LePage, 2003; Müller et al., 2005).

To facilitate this task, I have developed a Matlab GUI named TonotopyMapping (**Figure 14**). The inputs are the image stack, the voxel size, the desired source for the Greenwood function fitting and the desired number of equally distributed points along the tonotopic axis. The output are the interpolated coordinates, its corresponding frequency label and the logarithmic frequency label defined as:

$$F_{log} = log_2(\frac{F_{min}}{F})$$

To fit the tonotopic maps, I used the Greenwood's function and the parameters fitted from other publications (**Table 5**). In the case of the marmoset, given the lack of similar studies to establish the tonotopic map using histological sections and backtracing of characterized single units, we manually found the suitable combination of values for A and k, fixing alpha to 2.1 (assuming that the marmoset have a generalist cochlea) and considering the hearing range of the marmoset approximately 36.34 -0.124 kHz (Osmanski and Wang, 2011). As shown in **Figure 15**, the developed tool is compatible with multiple stainings, species and magnifications.

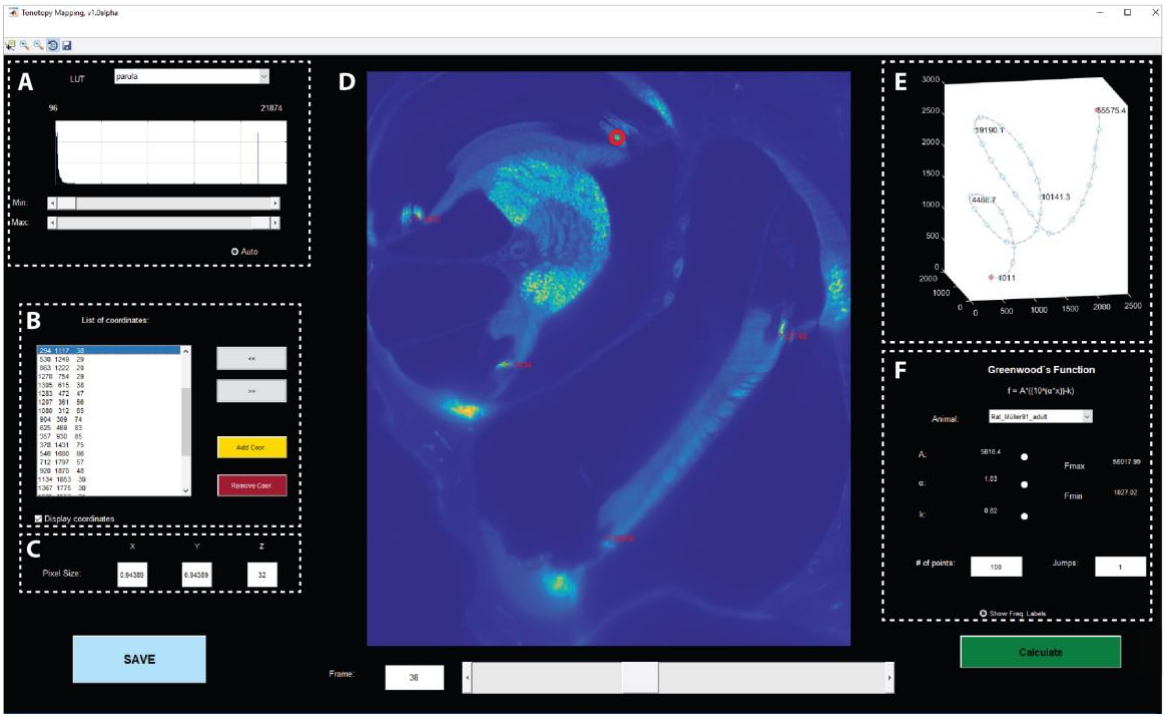

Figure 14. TonotopyMapping GUI. A. List menu with different color-maps for the look-up-table (LUT), current image histogram, and sliders to select the minimum and maximum pixel intensity value displayed. It can also be set to auto so these values are taken from the maximum and minimum of the current plane by clicking the push button. **B**. Coordinate navigator: list with all the coordinates registered, arrows that allow the user to navigate through the list and display the current coordinate as a circle with a thick line (see d), and the corresponding button to add a coordinate to the list (selected by the datatip cursor in d) or remove it (selected in the list). **C.** Fields to log the pixel size. **D.** Image display and navigator: the slider and the field box allow the user to navigate through the image stack. If the button "display coordinates" is selected the coordinates in the list corresponding to the current frame are displayed and if any of the coordinates are selected it will appear as a thick red circle. **E.** 3d view of the registered and interpolated coordinates are shown as blue empty circles and purple dots, respectively. If the push button in f "show freq. Labels" is pushed, five sparse tonotopic labels are shown. **F.** Greenwood´s function panel: the list menu allows selecting different pre-stored Greenwood´s function parameters already obtained from the literature (Table 5). The field "# of points" define the number of equally distributed interpolated points will be calculated by spline fitting and the field of "jumps" define the increment between the manually registered coordinates which will set the final number of points used for the interpolation. The "calculate" button perform the spline interpolation and the tonotopic labelling and the save button saves the variables corresponding to the manually registered coordinates, the interpolated coordinates, the Greenwood´s function parameters and the frequency labels in a designated folder.

Table 5. Greenwood´s function parameters available in the GUI TonotopyMapping

					Hearing range (Hz)		
Animal	**Name in GUI list**	**A**	**α**	**k**	**Max**	**Min**	**Publication**
Mouse	Mouse_60dB_West85	900	1.9345	0	79020.9	900	West, 1985
Mouse, CBA	Mouse_CBA_Müller05	4232	1.2790	-0.22	81384.67	5163.04	Müller et al., 2005
Mouse, C57Bl/CBA F1 Hybrid	Mouse_ C57BL/CBA F1_Ou00_Normal	2,553.00	1.4	0	64128.46	2553.00	Ou et al., 2000
	Mouse_ C57BL/CBA F1_Ou00_Edges	1,460.00	1.77	0	85971.17	1460.00	Ou et al., 2000
Gerbil	Gerbil_WrobelAndDieter18	255	2.1	0.01	32100	252.5	Wrobel et al., 2018
	Gerbil_Dieter19	398	2.1	0.5	49906.23	199	Dieter et al., 2019
	Gerbil_Müller96	398	2.22	0.631	65800.42	146.862	Müller, 1996
	Gerbil_Müller96_p11-18 (subadult)	345	1.9	0	27404.32	345	Müller, 1996
Marmoset	Marmoset_KeppelerDuqueAfonso	290	2.1	0.57	36343.54	124.7	Keppeler and Duque Afonso et al., in prep
Cat	Cat_Liberman1982	456	2.1	0.8	57042.1988	91.2	Liberman, 1982
Rat	Rat_Müller91_adult	5616.4	1.03	0.82	56017.99	1027.02	Müller, 1991

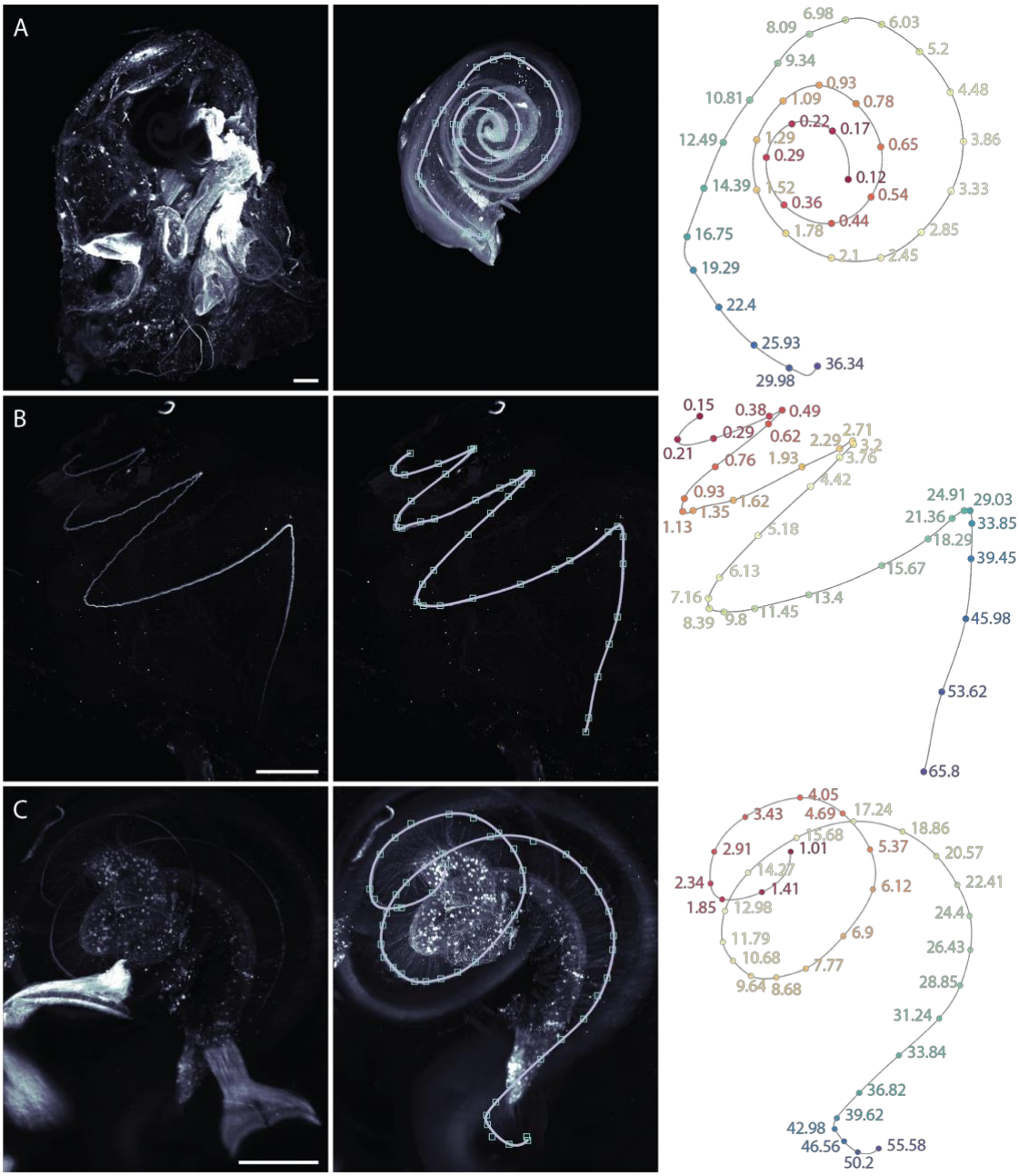

Figure 15. Tonotopic mapping in different species and stainings. Left panel shows a MIP of the sample, middle panel shows, in addition to the MIP of the sample, the manually registered points along the IHC row or peripheral processes of the SGNs (green squares) and the 1000 points equally spline-interpolated that define the tonotopic axis (purple dot line). Right panel displays the interpolated axis together with sparse tonotopic labels in kHz equally distributed with the Greenwood's function parameters for each species (Table 5). **A.** Marmoset's cochlea stained with an antibody against calretinin. The large amount of antibody absorbed by connective tissue in the outer part of the specimen that was not properly washed off masks the signal coming from the inner structures of the cochlea in the projection, revealed after manual segmentation of modiolus, Rosenthal´s canal and organ of Corti (middle panel, segmented for better visualization). **B.** Gerbil´s cochlea stained against vGlut3, a marker of the inner hair cells. **C**. Cochlea from a Venus rat, expressing ChR2-venus under the promoter Thy1.2. Staining against GFP reveals a salt-and-pepper expression pattern of the transgene. Similarly to A, the middle panel displays the organ of Corti and the ganglion manually segmented for clarity and left panel shown a MIP of the whole cochlea and partially the vestibular system.

2.3.4.2. FREQUENCY LABELLING

The next step aims to assign a frequency label to a given cell. Initial attempts using the tonotopic axis defined in the previous section resulted in a faulty labelling. To overcome this, I generate an alpha-shape with the *alphashape* function in Matlab, using an alpha radius of 40, enclosing the centers detected in a nonconvex polyhedron. Then, this object was imported as a .stl file and its centerline was calculated in VMTK (the Vascular Modelling Toolkit, Orobix Srl) and imported back to Matlab. 1000 points were equally distributed using spline interpolation and the corresponding label from the initial tonotopic axis (also 1000 points) were assigned respectively (**Figure 16A-D**).

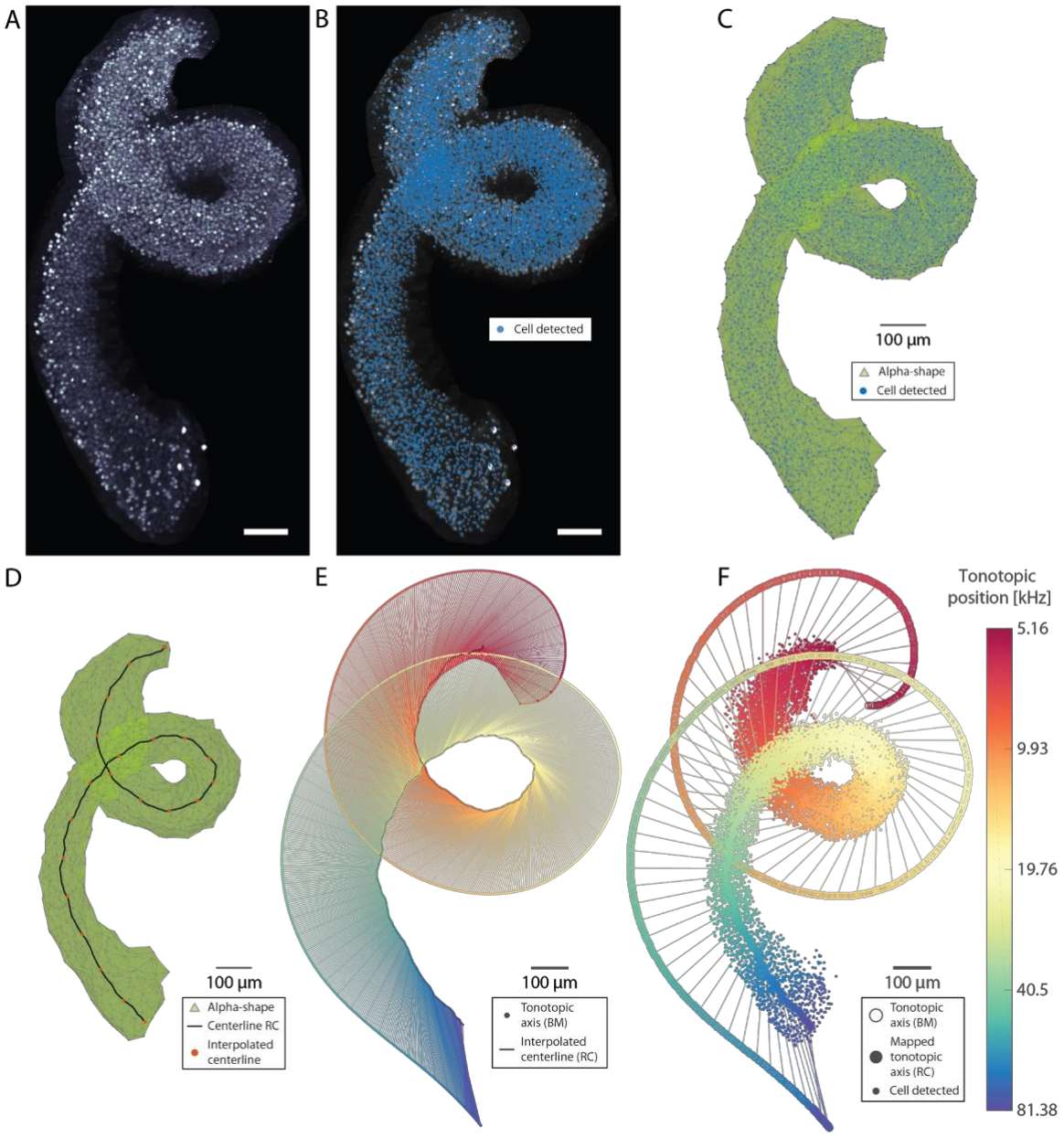

Figure 16. Tonotopy labelling routine. **A.** Manually segmented ganglion. **B.** Manually segmented ganglion with the coordinates of the cells detected after the Hough transform (blue). **C.** Alpha-shape (green) englobing the cells detected (blue). **D.** Alpha-shape (green) together with its centerline (black) and 21 out of 1000 points equally distributed (orange). **E.** The black line corresponds to the interpolated points in the centerline of the alpha-shape and the outer line of circles represents the interpolated points corresponding to the tonotopic axis defined. Radial lines depict correspondence between the tonotopic axis and the tonotopic positions mapped in the centerline. 100 out of 1000 are displayed in a darker color for clarity. **F.** Detected cells with its corresponding tonotopic label. Radial lines connect 100 out of 1000 centerline coordinates with their corresponding tonotopic axis coordinates. Scale bar for A and B: 100 µm.

Once the tonotopic axis was defined and mapped in the centerline of the ganglion/Rosenthal´s canal, each cell was assigned with a frequency label, following the algorithm described in **Figure 17**.

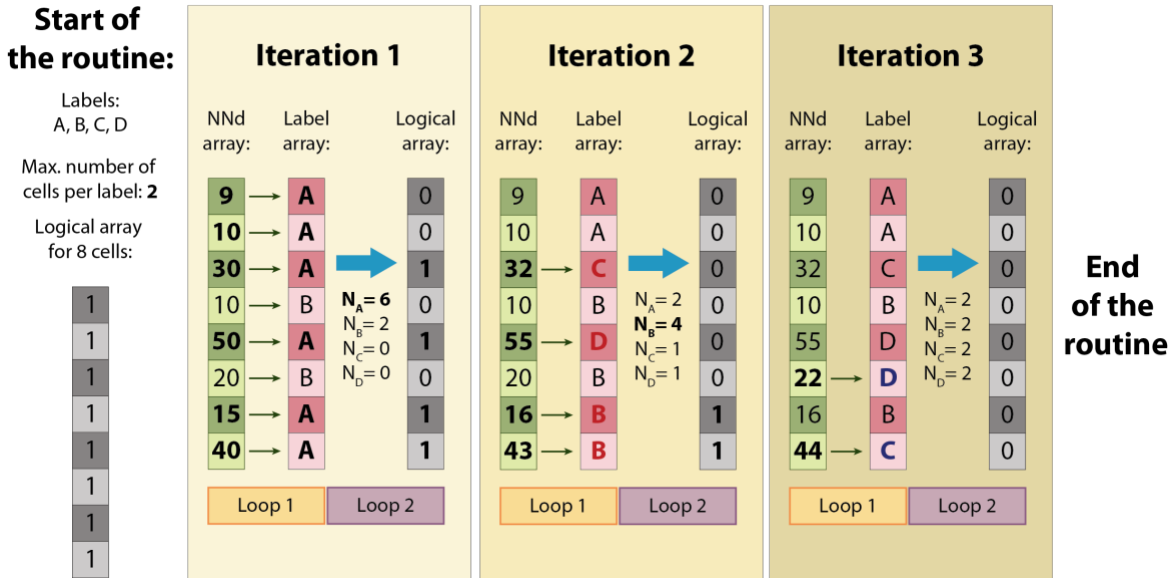

Figure 17. Example of the tonotopic labelling algorithm. The algorithm starts with the labels to be assigned, the maximal number of cells per labels (MNCpL) and with a logical array of size number of cells x 1. All the positions along the tonotopical array are set to 1, allowing the modification of all the cells. In the beginning of the iteration 1, all the distances between cell - labels are computed, and a given label is assigned to the cell when the distance is minimum. When all the cells have a corresponding label, the number of cells per label is calculated. Only the n = MNCpL cells, ordered from closer to further distance, are kept (logical array = 0), where the rest are allow to undergo another iteration of classification (logical array = 1). NNd: nearest-neighbor distances; nx; number of cells labelled as x.

To initialize the labelling routine the following variables are created:

- A maximum number of cells per label was defined as MNCpL = (number of cells/number of labels)*2.
- A logical 1D array with a size equal to number of cells was created to define which cells can have their frequency label changed in that given iteration and all its values were set to 1.

Then, for each cell, its corresponding frequency label was assigned following this iterative process:

- Iteration 1:
    - Sub-iteration A: - For every cell, whose corresponding position in the logical array is 1:
        - The distance between each cell (i) and all the frequency labels (j) was computed as

$$d = \sqrt{(x_i - x_j)^2 + (y_i - y_j)^2 + (z_i - z_j)^2}$$

        - The nearest-neighbor frequency label was assigned to each cell

    - Sub-iteration B - For every label:
        - Set the corresponding positions in the logical array to 0
        - If the number of cells with this given label is higher than the defined maximum:
        - The cells are sorted by the distance to the label
        - Only n = MNCpL are kept and the rest are set to 1 in the logical array, allowing its modification in the next iteration

- Iteration 2 until the end: Iteration 1 is repeated as many times as needed until the summation of the logical array is 0.

2.3.5. MEASUREMENT OF RELATIVE INTENSITY LEVELS ALONG THE TONOTOPIC AXIS

The GFP stacks were aligned to the PV channel with the FIJI plugin *Bigwarp* (Bogovic et al., 2016), using approximately 10 landmarks and Rotation transformation (a linear transform with 6 degrees of freedom for rotation and translation).

For every center coordinate of each cell detected, a 7x7x4 ROI was defined where the average, median, minimum and maximum value were retrieve for both channels, PV and GFP. For every sample, the mean values were normalized as:

$$I_{norm} = \frac{I}{I_{min}}$$

where I corresponds to the mean intensity of a given cell 3D ROI and I_{min} to the minimum mean intensity of all the cells in a given sample. To classify the detected cells, as positive for GFP, and therefore, as cells expressing the channel of interest (in this case Fast-Chrimson), I set a threshold equal to the mean I_{norm}+SD of the GFP channel in the non-injected ears.

2.3.6. STAINING PENETRATION QUANTIFICATION FOR NANOBODIES EXPERIMENTS

The original stack was resampled by a factor of 2.15x2.15x2 and converted to 8-bits in FIJI. Then, the ganglion was coarsely segmented manually with the FIJI plugin *TrakEM2* (Cardona et al., 2012) and imported to the open source software *3DSlicer* (Fedorov et al., 2012; Kikinis et al., 2014). There, a median filter with a kernel of 10x10x1 pixel was applied and the resulting image was threshold segmented, converted to a 3D closed surface and stored as a .stl file, as it is the input format needed for the following step. Centerlines of the ganglion were then calculated using the *vmtkcenterline* function of the open source software VMTK and then imported to Matlab for further analysis (**Figure 18**), together with the mesh and raw stack. The centerline was fitted using spline interpolation and 100 position equally spaced were retrieved. In each of this positions, 14 radius of 200 μm were positioned, 8 orthogonal to the rest. The chosen orientation was parallel to the apical-basal axis formed by the most apical and most basal coordinate of the centerline. Those radii that were inside of the mesh, checked by the function *inpolyhedron* (Holcombe, 2015), or outside of the original image space, were removed. Radii were mapped in the image space and the pixel values in their coordinates were used to obtain the line profiles. The minimum of each profiles was subtracted from itself to have a comparable baseline.

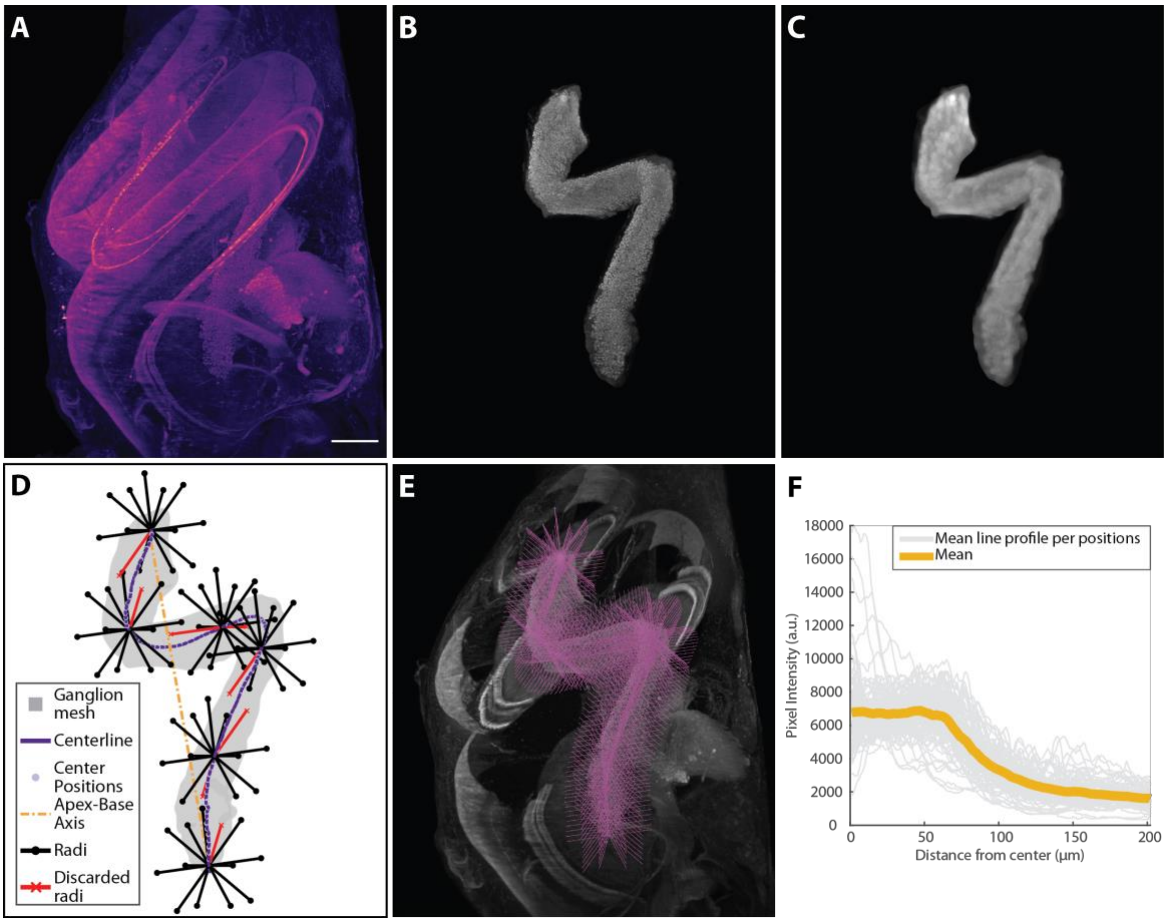

Figure 18. Method to investigate the penetration of different labelling approaches. **A.** MIP of a cleared cochlea stained with an antibody against parvalbumin premixed with a nanobody anti-guinea pig. **B.** coarse manual segmentation of the ganglion. **C.** median filtered image of the ganglion (kernel: 10x10x1). **D.** 2D projection of the mesh created from a threshold segmentation of c), its centerline, the apex-base axis, the center positions where the radii fan out and the used and discarded radii. Only six out of the 100 center positions and their corresponding radii used are displayed for clarity. **E.** MIP of a substack of the slices that contains only the ganglion. In magenta, all the radii mapped back in the image space. **F.** example of mean line profile per position (n=100 positions) and mean line profile for this sample is plotted against the distance from the center position. Scalebar for A-C and E: 200 µm.

3. RESULTS

3.1. DEMONSTRATION OF THE COMPATIBILITY OF CDISCO WITH ANTIBODIES AND DYES

In the following section, I will present an initial screening on the compatibility of some antibodies widely used in the inner ear with cDISCO. The markers of interest were two mobile calcium buffers (Parvalbumin-alpha (PV) and calretinin (CR)), vGlut3 (a protein critical in the functioning of the IHC-SGN synapse) and GFP (a proxy marker of the expression of the transduced opsins). In addition, I tested some dyes that could be of utility for further developments and experiments: 7-AAD (a fluorescent nuclear marker) and a lectin (a vascular wall dye).

3.1.1. CALCIUM BUFFERS: PARVALBUMIN-ALPHA AND CALRETININ

Calcium, together with phosphate, are two of the most universal tools in cell functioning and signal transduction, since they can trigger changes in local electrostatic field and therefore in the protein conformation. Thus, calcium is a key ion that can regulate cellular processes that range from the cell shape (by alteration of cytoskeleton structures) to metabolic/enzymatic processes. The intracellular levels of this ion are always kept low (approx. 20000-fold gradient with respect to the extracellular medium). Since low, focal changes in its concentration can trigger a wide plethora of events, cells spend most of its energy in chelating, compartmentalizing or extruding this divalent ion (Clapham, 2007).

In the cochlea, the fast nature of the stimuli that are transduced there and the high metabolic and energetic demands might have obliged the cells to adopt an army of professional calcium binding proteins, including mobile buffers (PV, CR, calbindin(CB)), signaling proteins (calmodulin, Ca^{2+}-binding proteins), protein folding (calreticulin, calnexin)(Fettiplace and Nam, 2019) or sensors (otoferlin) (Roux et al., 2006). More concretely, calcium participates in mechanotransduction (vg. maintaining the structure of the tip-links and contributing to the mechanotransduction current), synaptic transmission (vg. glutamate exocytosis from IHC presynaptic terminal requires the influx of calcium through Cav1.3 channels, or regulation of action potential activity through the calcium-activated potassium currents after hearing

onset), non-sensory cells physiology processes (vg. intracellular communication through GAP junctions, or ATP-triggered calcium waves) (Ceriani and Mammano, 2012).

In the hair cells and SGNs, the calcium-binding proteins CR, CB-D28k, PV and parvalbumin-beta (also known as oncomodulin) works as mobile cytoplasmic calcium buffers. They spatiotemporally restrict the calcium movement and whose expression is regulated differently across cells, development and species (Fettiplace and Nam, 2019) . Furthermore, all of the members of this family share EF-hand motifs of roughly 30 residues, normally present in adjacent pairs, characterized by the presence of a helix-loop-helix motif that can accommodate calcium or magnesium (Lewit-Bentley and Rety, 2000).

PV has been reported to be in IHCs (Celio, 1990; Pack and Slepecky, 1995; Soto-Prior et al., 1995), in OHCs (only in rats, and mostly in their apical turn (Celio, 1990)), in all subpopulations of type I SGNs (Petitpré et al., 2018; Shrestha et al., 2018) and in the postsynaptic terminals and fibers of type II neurons (Maison et al., 2016). In **Figure 19**, this pattern can be seen in the cochleae from mouse, rat and gerbil.

The role of PV in the SGN does not seem to be completely understood. It is thought to be involved in many levels of the adaptation to precise and rapid processing of acoustic stimuli. Taking into consideration other in vitro studies in other cell types, it has been hypothesized that it could work 1) buffering sudden increases of intracellular calcium that occur during sound induced depolarizations, 2) controlling the changes in the cytosolic calcium after depolarization in terms on rise and decay rates and amplitude, regulating the synaptic release of neurotransmitters and intracellular signaling processes and ultimately the auditory transduction (Soto-Prior et al., 1995; Yang et al., 2004).

In IHC, CR, PV and CB decrease the amplitude of the calcium conductance and attenuates its activation, in addition to their role on restricting calcium-dependent glutamate release to the active zones, generating an efficient metabolic control of the calcium-dependent sound encoding (Pangrsic et al., 2015).

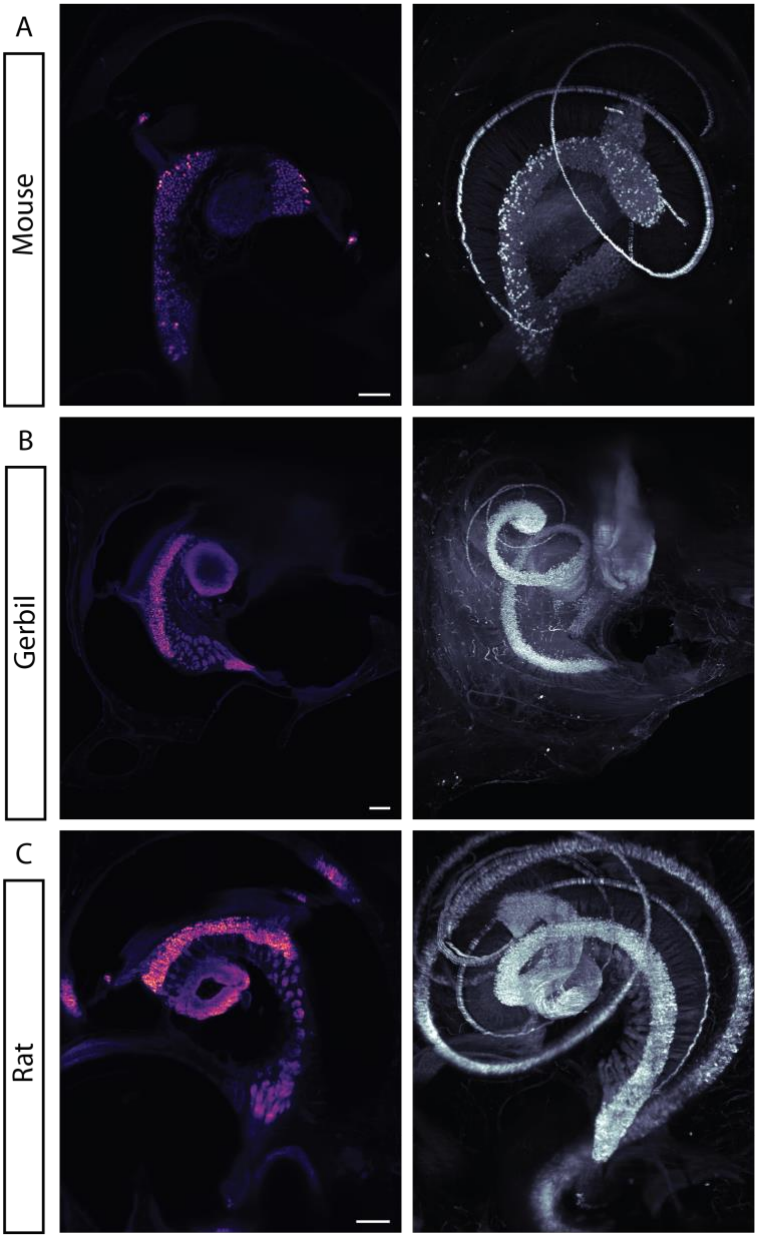

Figure 19. Type I SGN and IHC stained with PV. Left column displays exemplary single slice. They show mid-basal sections where the spiral ganglion, hair cells and auditory nerve can be appreciated. Right column shows the IHC row has been damage and three pieces can be identified outside the IHC row and that in the apical turn of the rat´s cochlea OHCs are also revealed). Background signal allows also to coarsely intuit the cochlear anatomy and occasionally other structures such as vessels (Gerbil´s) or stria vascularis (Rat´s). **A.** Mouse, **B.** Gerbil, **C**. Rat. Scalebar: 200 µm

The other calcium buffer that we considered was another EF-hand motile calcium buffer: CR.

In IHCs, it has been shown to be homogenously expressed, whereas in SGNs its expression display a gradient among the subtypes of adult type I SGN, being mostly expressed in two subsets, accounting for 35 (Ia, highest levels) and 40% (Ib, mid levels) of the type I neurons (Shrestha et al., 2018). The same study found that CR follows a gradient orthogonal to the tonotopic axis and that its levels seem to correlate with the classical classification of high

spontaneous rate (high levels of CR, closer to ST, contacting the pillar side of IHC), mid spontaneous rates and low spontaneous rate (low levels of CR, closer to SV, contacting the modiolar side of IHC). In **Figure 20**, this staining principle can be seen, the antibody anti-CR labels totally the IHC row, where the ganglion adopts an intermittent pattern, highlighting the fact that is not all the neurons that reside there expresses this calcium buffer.

In a similar fashion to PV, its precise and individual role in each of the cell types has not been fully dissected. However, Iin IHCs, it has been shown its contribution to the Ca^{2+}-nanodomain control of vesicle fusion (Pangrsic et al., 2015) . All the SGN expressing calretinin seem to be unitary accommodating neuron (Petitpré et al., 2018) and the ratio calbinidin/CR has been hypothesized to serve as an indicator of the kinetics of the SGN (when the ratio is closer 1, SGNs exhibit longer time constants) (Liu and Davis, 2014). Furthermore, the lower levels of CR in afferent fibers innervating the modiolar side of the IHCs have been related to an increase in their vulnerability to noise trauma (Sharma et al., 2018). All in all, it could be hypothesized that through its calcium buffering capabilities, it can shape the activity-dependent responses and the cells resistance to sound insults.

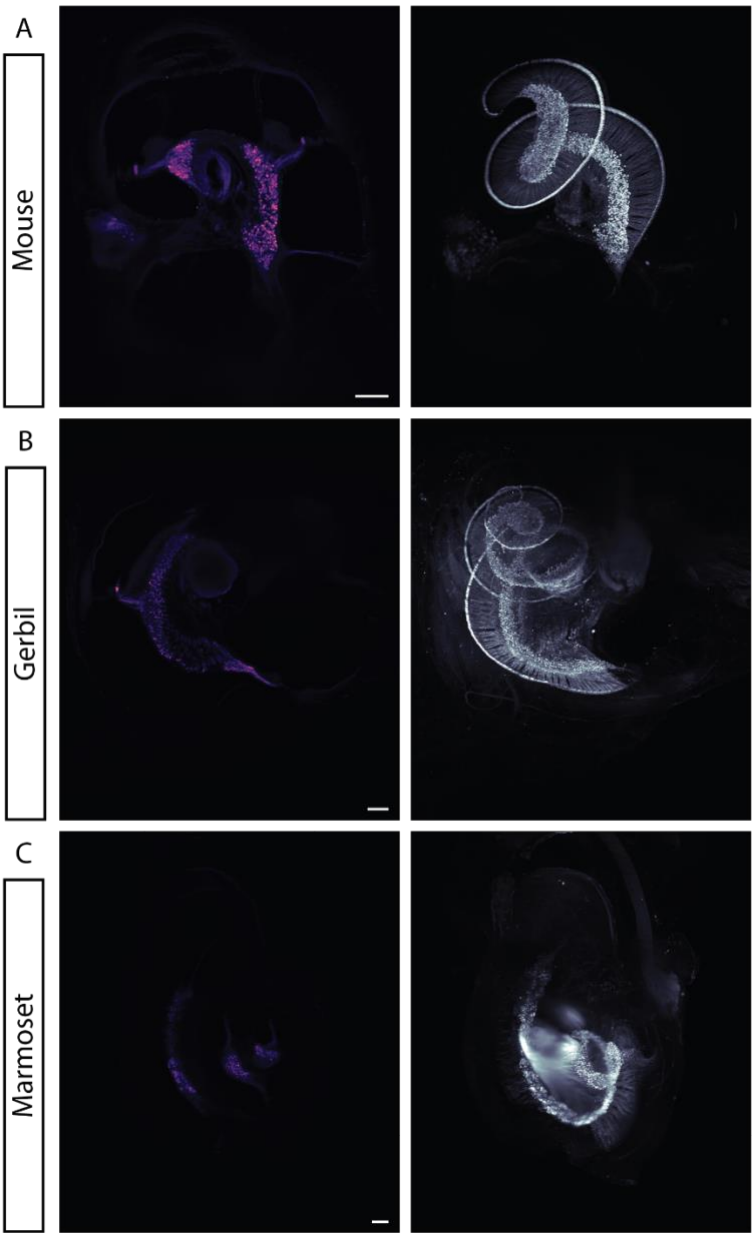

Figure 20. IHC and subtype of type I SGN revealed by CR staining. Left column depicts exemplary optical section, where the SGN and IHC can be seen. Since only a subtype of type I SGN is stained, the staining acquires a more intermittent pattern when compared to PV. IHC in the marmoset cochlea seem to be not visible, probably due to an imperfect conservation of organ of Corti after harvesting the sample. Right column displays MIP. **A.** Mouse (tissue processed in collaboration with Dr. Christian Vogl). **B.** Gerbil. **C.** Marmoset. Scalebar: 200 µm.

3.1.2. IHC MARKER: VGLUT3

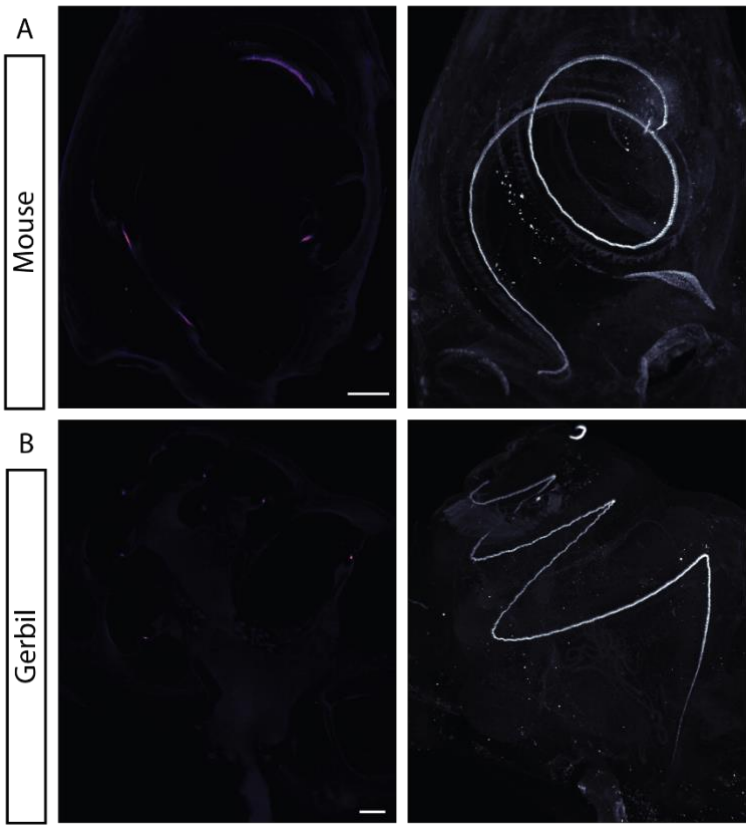

Figure 21. IHC staining by vGlut3. A. Mouse´s cochlea. **B** Gerbil´s cochlea. Left panel shows an exemplary slice (Note that the gerbil´s slice was acquired highly orthogonally to the modiolar axis and the IHCs are shown as small puncta. Right panel shows MIP where the single IHC row is beautifully spiraling down the cochlea. Note the different number of turns and the different shapes of the hook region. It can be appreciated a high signal-to-noise ratio only disturbed by small staining artifacts and little background signal. Scalebar: 200 µm.

Next, we employed the IHC marker, vGlut3 to explore the capacity of the cDISCO and light-sheet microscopy for evaluating the IHC and organ of Corti along the tonotopic axis (**Figure 21**). VGlut3 encodes the vesicular glutamate transporter 3. Although most central glutamatergic synapses expressed vGlut1 and 2 isoforms, only few neurons in some areas of the CNS express the isoform 3 and they are not glutamatergic but instead use serotonin (medial and dorsal raphe nuclei), acetylcholine (striatum and basal forebrain) or GABA (hippocampus, cortex, Purkinje cells, nucleus of trapezoid body) (reviewed in El Mestikawy et al., 2011). vGlut3 is not only limited to the brain and it has been found also in retina (amacrine vGlut3+ cells, (Haverkamp and Wässle, 2004)), cochlea (inner hair cells, (Ruel et al., 2008; Seal et al., 2008)) esqueletic muscle, kidney, heart and liver (Boulland et al., 2004; Fremeau et al., 2002; Munguba et al., 2011).

In neurons, it has been shown that target different cellular compartments. Whereas vGlut 1 and 2 can be found mainly in the axons, vGlut3 is relegated to cell body and dendrites too and

has been related to retrograde synaptic glutamate release, but it role in synaptic glutamate release was obscure for long time. In 2008, (Seal et al., 2008) reported a robust expression of vGlut3 in the cochlea only in the IHC starting at E19 and keeping constant through development. They found that although the electrophysiological behavior of the IHCs was comparable to WT, the lack of vGlut3 in a knockout was abolishing the glutamate release rendering the IHC-SGN synapse completely nonfunctional. The absence of an IHC-dependent neuronal activation and sound transduction, although with increased presynaptic Ca^{2+} current, resulted in a progressive loss of SGN (seen also by the loss of ABRs) and entirely deaf animals, presumably due to the inability of the presynaptic terminal to refill synaptic vesicles (Ruel et al., 2008; Seal et al., 2008). It is not surprising that mutations in the gene encoding for vGlut3, SLC17A8, are also involved in human diseases, as they are presumably the underlying cause of the non-syndromic human deafness, DFNA25 (Ruel et al., 2008). For its specificity targeting only IHCs in the cochlea it is an excellent marker of this cell kind. Apart from the examples here presented in mouse and gerbil, given the use of comparable stainings in other studies, it might potentially extensible to other species, such as rat (Peng et al., 2013) or guinea pig (Yu et al., 2016).

3.1.3. A PROXY MARKER OF THE EXPRESSION OF A FOREIGN PROTEIN: GFP

As mentioned before, we have shown the feasibility, advantages and also limitations of optogenetic stimulation of the cochlea in various animal models, including transgenic mouse (Hernandez et al., 2014), transgenic rats (Hernandez et al., 2014), postnatally injected mice (Keppeler et al., 2018; Mager et al., 2018) and postnatally injected gerbils (Dieter et al., 2019; Wrobel et al., 2018). All of them share that the opsin of choice it is expressed as a fusion protein with a fluorescent protein, normally GFP or similar (EYFP or VENUS), which is used as a proxy of the channel expression. Furthermore, GFP-expression is a common strategy in the characterization of gene therapy strategies, either to confirm the tropism of virus serotypes (Kim et al., 2019; Leake et al., 2011) or the expression of the transduced protein of interest itself (Atkinson et al., 2014; Praetorius et al., 2009). EYFP and Venus expressing neurons from

transduced mouse SGN and transgenic rats, respectively, were successfully stained and revealed different patterns of expression in the two different models (**Figure 22**).

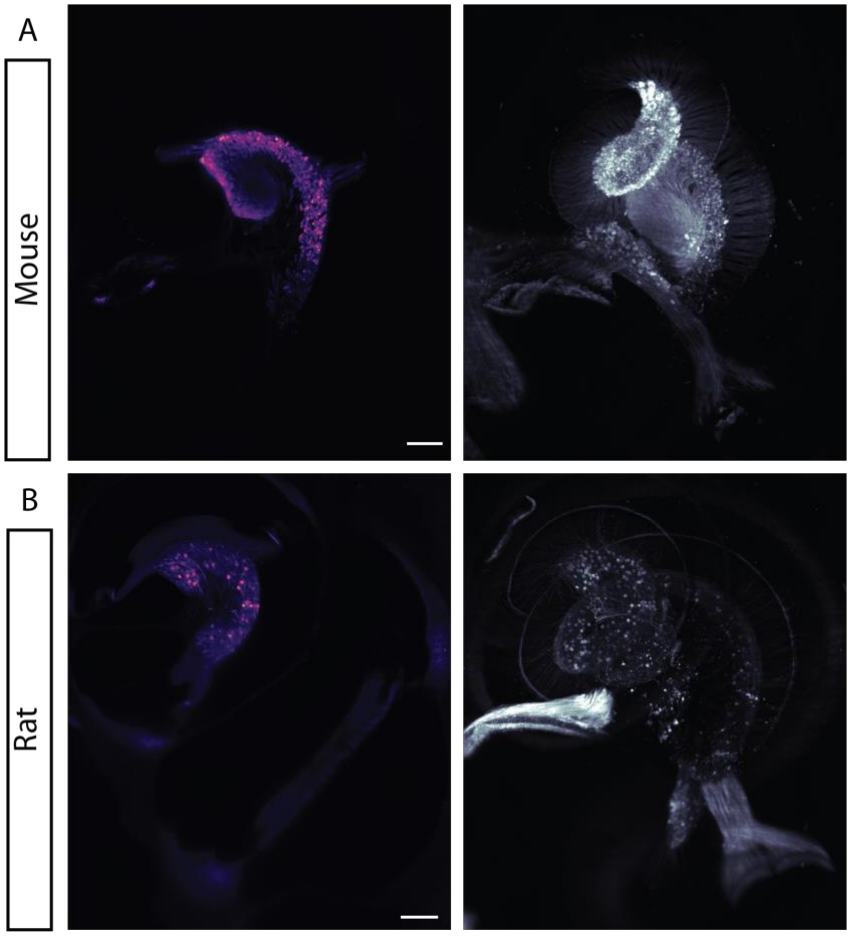

Figure 22. GFP expressing neurons. Exemplary slice and MIP of cochleae expressing GFP from **A.** Mouse expressing fast-Chrimson-EYFP under the hSyn promoter, via round window injection of a PHP.B viral gene vector; and **B.** Transgenic rat expressing ChR2-Venus under the Thy promoter. In both cochlea, the cell soma and fiber can be appreciated. In addition, the neurons harbored by Scalebar: 200 µm.

In the mouse (**Figure 22A**), fast-Chrimson-EYFP under the hSyn promoter and was carried through an injection of PHP.B virus through the round window. The expression pattern seems to have a tendency to follow an apical-basal gradient (see Section 3.3) and included not only SGNs, but also the Scarpa´s ganglion neurons (from the vestibular system) and some cells embedded in the auditory nerve, after the exit from the cochlear walls (**Figure 23**). These latter cells describe two different morphology: one type shows small somas, with highly ramified thin processes and the other a big soma with one or two thick processes that split as they move away from the soma. Although further molecular characterization should be done in order to know the cell type, they might be presumably cochlear root neurons. The cochlear root neurons (also known neurons of the acoustic nerve nucleus (Harrison and Irving, 1966) have been

described as big cells with a thick axon that runs along the auditory nerve and it is documented to be present in mouse, rats and gerbil (reviewed in (López et al., 1993)). In the rat, they have been extensively studied by the Spanish team of Lopez, Merchan, Saldana et al. They have described their numerous inputs (cholinergic inputs of the ventral nucleus of Trapezoid Body, glutamatergic inputs from auditory nerve fibers, noradrenergic inputs from locus coerelus, GABA and glycinergic contacts with an unknown origin), output (caudal pontine reticular nucleus) and its role in the primary acoustic startle reflex (Gómez-Nieto et al., 2013; Hormigo et al., 2015, 2017, 2018). The role of the small neurons still remains to be not fully understood, although have been described at the ultrastructural level (Ross and Burkel, 1971) and are presumably Glycinergic and GABAergic (Osen et al., 1991).

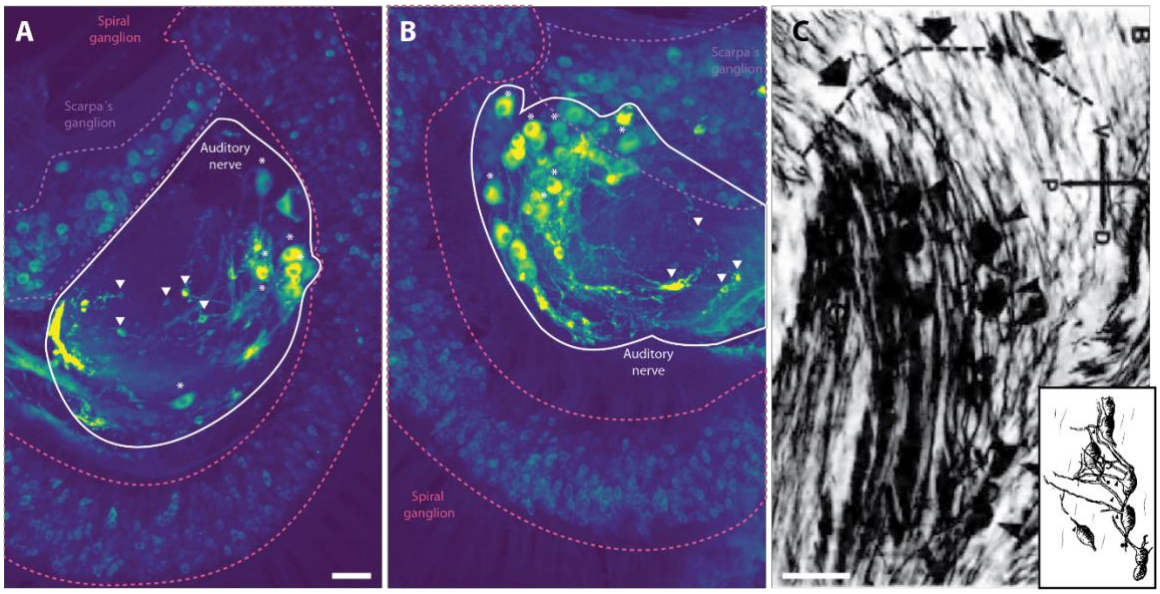

Figure 23. Cochlear root neurons. **A and B**. Maximal intensity projections of substacks corresponding to the basal part of the cochlea, where the basal turn of the Spiral Ganglion, a portion of the Scarpa´s ganglion and some different populations of cochlear root neurons, Some examples are highlighted with asterisk (cochlear root neurons), and arrowhead (small neurons). Scalebar: 50 µm. **C.** Micrograph of a reduced silver method staining of the auditory nerve root of the rat. Cochlear root neurons are indicated with arrowheads. The dashed line delimit the glial border. Insert, Camera lucida drawing (modified) of rat root neurons revealed by Golgi staining. Reproduced from López et al, 1993.

In the rat (**Figure 22B**), the Venus expression distribution is homogenous through the tonotopic axis, displays a salt-and-pepper pattern and it is presumably present in both type I and type II SGN, since fibers that crosses the IHC row are also visible (Berglund and Ryugo, 1987). As in the mouse example, the neurons harbored in the Scarpa's ganglion also show a strong expression of the transgene.

3.1.4. DYES: LECTIN-DYLIGHT 594 AND 7-AAD

Finally, I have also tested two dyes, as proof of concept, to be used potentially in further experiments.

The cochlea vasculature is fundamental for the homeostasis of the organ. Alterations of the vascular barrier and the underlying loss of the endocochlear potential is consider one of the mechanisms for hearing loss (Shi, 2011). Being able to study the vessels of the whole cochlea might be useful to study the structure and the relationship between vessels and other cellular elements, and its changes during development, aging and pathological conditions..

Lectins are glycan-binding-proteins found in all living organism involved in protein metabolism, cell adhesion and immune functions (Taylor et al., 2015). Here, I used a Lectin I, Isolectin B4, coupled to the fluorophore DyLight 594, from the plant Griffonia Simplifolia. It is specific for α-galactose residues present in glycoproteins, such as laminin, and it is a marker for endothelial cells of some species such as rat, mouse, goat and rabbit, as detailed in the manufacturer datasheet (Vector Laboratories, DL-1207).

In this experiment, I have stained the vessel walls (**Figure 24**) by immersion of the mouse cochlea in the dye diluted in the same solution as the antibodies. It provides a coarse staining of the vascular walls, without allowing an easy dissection of the vascular tree. Further experiments including injection of a combination of lectin (vessel wall) and FITC-Dextran (vessel lumen) intravenously through the retro-orbital sinus (Jiang et al., 2019) might improve the contrast and quality of the staining and allow a better identification of the microvasculature of the cochlea.

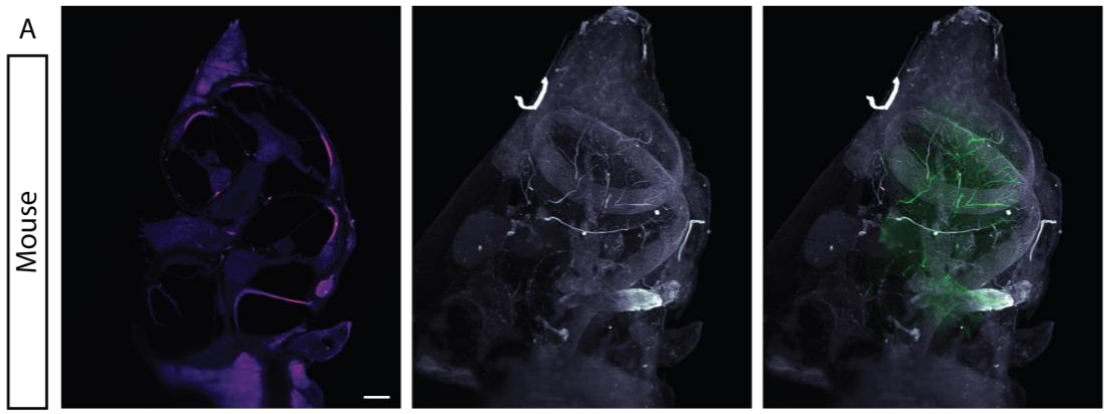

Figure 24. Vascular staining with Lectin. Cochlear vasculature from mouse revealed by lectin staining. Left panel, exemplary slices. Middle and right panel, MIP. In the right panel, the organ of Corti and modiolus were manually segmented and displayed in green for clarity. Scalebar: 200 µm.

One possibility that we would like to explore in the future is the combination of a nuclear staining with a cell specific staining, so the cell specific marker can be used as a mask to isolate the round-shaped nucleus (see Discussion). The SGN and IHC nuclei can be more easily approximated to a sphere than the cytoplasm, providing a geometrical shape more consistent and robust and less variable among cells of the same kind than the cytoplasm, potentially improving the performance of the Hough Transform for cell detection. In **Figure 25**, it can be appreciated a highly cellular cochlea, where the individual cell nuclei can be identified.

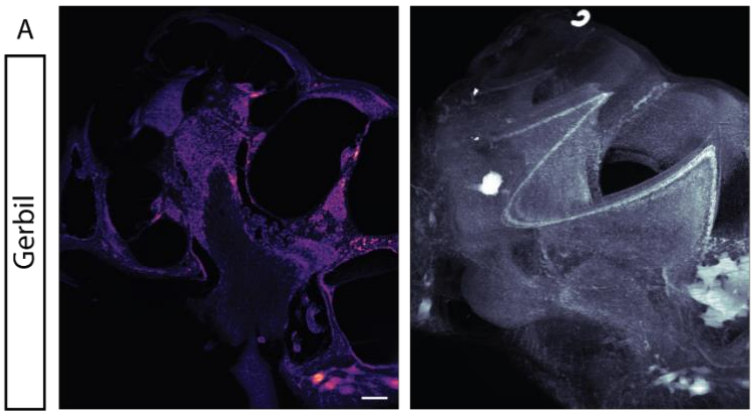

Figure 25. DNA staining with 7-AAD. 7-AAD binds DNA molecules, rendering the cell nuclei visible and displaying the high number of cells present in the cochlea, especially in the organ of Corti (stronger intensity band in B). A, Exemplary slice. B, MIP.

3.2. CELL QUANTIFICATION IN THE MOUSE COCHLEA

One preliminary step to assess the viral transduction levels as a function of the tonotopic function is to detect the cells by using some of the antibodies explained in the previous section. After processing, clearing and imaging the cochleae from injected animal, they were further analyzed. Firstly, I manually quantified the IHCs and, secondly, the neurons were semi-automatically detected.

3.2.1. INNER HAIR CELLS

In order to first evaluate whether our technique could provide enough resolution to quantify the IHCs in an intact preparation, I manually counted the IHCs by registering the position of each using the point tool and the ROI manager of FIJI. I estimated a total mean 639.54± 21.72 of IHC with no substantial differences neither among ages nor among conditions (although given the low number of samples no statistical test was performed) (**Table 6**). It is worth mentioning that the resolution was reduced in those parts of IHC row parallel to the acquisition axis (more influenced by the axial resolution) and in the hook region (the most basal part of the cochlea). In these parts, the morphological features of the IHC were not totally outlined. Nevertheless, cells could be identified along the row as pixel clouds with a higher intensity center (although it could have caused a slight deviation from the real numbers). IHC rows in the imaging plane (orthogonal to the Z axis, lateral resolution), were nicely identifiable.

Table 6. Manual count of IHCs in the mouse cochlea at postnatal day 14 (p14) and three months old (3m)

Age	Non-injected	Injected	Mean±SD
p14	677	667	672 ±7.07
p14	613	655	634 ±29.7
p14	608	659	633.5 ±36.06
Mean±SD	632.67 ±38.48	660.33 ±6.11	646.5 ±19.56
3m	620	N/A	620
3m	619	648	633.5 ±20.51
3m	645	638	641.5 ±4.95
3m	623	642	632.5 ±13.44
Mean±SD	626.75 ±14	642.67 ±5.03	631.88 ±8.9/ 634.71 ±11.25*
Total **Mean±SD**	629.29 ±24,06	651.50 ±10,89	639.54 ±21.72/ 638.14 ±15,71*

*Mean of mean by condition

3.2.2. SGNs

I applied a 3D Hough transform to the preprocessed stack corresponding to the PV staining to obtain the coordinates of the cells of the segmented ganglion. The cochleae were split by age and by condition (injected and non-injected) and the analysis yield the following average values (the individual values are displayed in **Table 7**). For post-natal day 14 (p14), the average number of SGN was 8751.67 ±1835.34 for non-injected cochleae and 12058.67 ±1290.67 for injected ones,. For the cochlea of 3 months old animals, the non-injected cochleae harbored 8820.33 ±1821.53, whereas the injected ear had 11309.33 ±2313.19 SGN. Given the low number of samples (n = 3, per condition), no statistic test was performed.

Since the analytical routine was semi-automated, it is important to be aware of the error made. For that, three regions, distributed along the cochlea (approximately in the apical, medial and basal turn) were selected and the detected objects were labelled as “true” or “false” cells (true positive, false positive). In addition, not detected cells were registered (false negative). The overall precision was 0.81 ±0.09 and recall 0.76 ±0.08. Their harmonic mean, the F1 score, also resulted in comparable values: 0.78 ±0.08. Given this numbers, it can be concluded that the semi-automatic detection of SGN works in a decent fashion. However, the high variability in cell number within the same animals and a relatively low precision and recall explicitly call for an further improvement of the detection algorithm.

Given that the precision corresponds to the proportion of true positives detected from all the objects detected and the recall to the proportion of true positives cells from all the real cells, I backcalculate the estimate number of cells as:

$$p = \frac{TP}{TP+TN};$$

$$r = \frac{TP}{TP + FN};$$

$$N_{Hough\ T.} = TP + TN;$$

$$TP_{estimated} = p * N_{Hough\ T.};$$

$$r = \frac{TP}{TP + FN};\ r = \frac{TP_{Estimated}}{N_{Estimated}};r = \frac{p * N_{Hough\ T.}}{N_{Estimated}};$$

$$N_{estimated} = \frac{N_{Hough\ T.} * p}{r}$$

Where p means precision; r means recall; TP, TN, FN stands for true positive, true negative and false negative; $N_{Hough\ T.}$ refers to the number of objects detected by the analysis; $TP_{estimated}$ is the expected True Positive back calculated from the obtained precision value and the number of detected objects; and the $N_{estimated}$ is the calculated expected cells.

The estimated N made the differences between mean value smaller and resulted in more homogenous means.

Taking advantage of the annotated tonotopic axis and the centerline calculated from the alpha-shape generated with the cells detected, some basic cochlear morphological descriptors can be extracted from the dataset, namely the length of the Rosenthal´s canal (the structure enclosing

the SGN) and the basilar membrane at the level of the IHCs. They have a mean length 2298.72 ±103.33 and 5750.92 ±207.22 µm, respectively, resulting in a ratio of 0.40 ±0.01.

In addition, I used the tonotopic labelling to assess the cell distribution along the tonotopic axis (**Figure 26**). There were no evident differences among the ages or the conditions, and all displayed a very similar pattern: a higher concentration of cells in the low frequency/more apical region that decreased progressively until the region spanning 30-40 kHz followed by a brief peak around 60-70 kHz to decrease again until the most basal region.

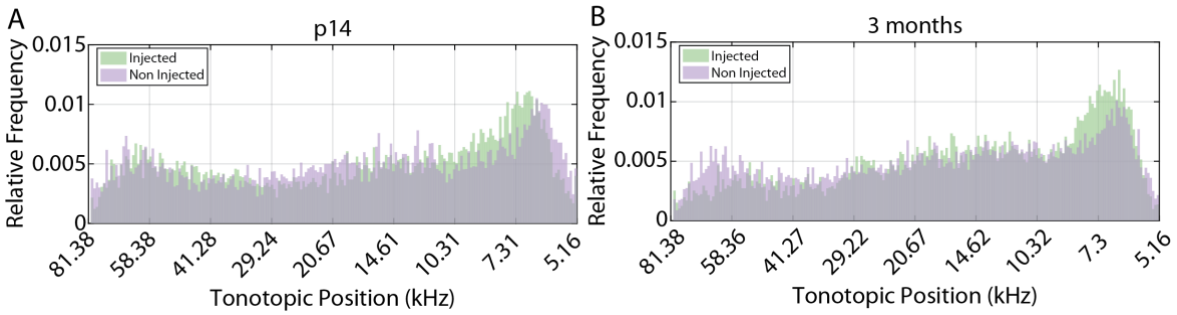

Figure 26. Distribution of type I SGNs along the tonotopic axis in injected and non-injected cochleae from animals of **A.** p14 and **B.** 3 months old.

Table 7. Spiral ganglion neuron counts and basilar membrane length estimates. N, number of SGN; RC, Rosenthal´s canal; BM; Basilar Membrane.

			Precision				Recall				F1 score		Length (µm)		
			Subvolume			Mean	Subvolume			Mean					Ratio RC/BM
	Age	N	1	2	3		1	2	3			Estimated N	RC	BM	
Non-injected	p14	9284	0.88	0.67	0.84	0.8	0.42	0.46	0.67	0.52	0.63	14302.28	2326.00	5799.70	0.40
	p14	6709	0.77	0.68	0.67	0.71	0.7	0.68	0.76	0.71	0.71	6631.02	2401.20	5898.60	0.41
	p14	10262	0.87	0.86	0.94	0.89	0.75	0.83	0.93	0.83	0.86	10985.67	2158.90	5640.90	0.38
	Mean±SD	**8751.67** ±1835.34				**0.80** ±0.09				**0.69** ±0.16	**0.73** ±0.12	**10639.66** ±3847.32	**2295.37** ±124.02	**5779.73** ±130.01	**0.40** ±0.02
Injected	p14	13294	0.68	0.74	0.95	0.79	0.85	0.77	0.94	0.85	0.82	12330.26	2287.70	5683.50	0.40
	p14	12163	0.59	0.6	0.62	0.6	0.79	0.48	0.88	0.71	0.66	10303.74	2374.20	5770.90	0.41
	p14	10719	0.77	0.88	0.96	0.87	0.85	0.63	0.95	0.81	0.84	11547.73	2223.00	5749.10	0.39
	Mean±SD	**12058.67** ±1290.67				**0.75** ±0.14				**0.79** ±0.07	**0.77** ±0.1	**11393.91** ±1021.98	**2294.97** ±75.86	**5734.5** ±45.49	**0.4** ±0.01
Age mean ±SD		**10405.17** ±2301				**0.78** ±0.11				**0.74** ±0.12	**0.75** ±0.1	**11016.78** ±2551.31	**2295.17** ±91.95	**5757.12** ±90.57	**0.4** ±0.01
Non-injected	3m	8343	0.86	0.98	0.96	0.93	1	0.83	0	1	0.82	10581.48	2383.52	5804.24	0.41
	3m	10833	0.81	0.77	0.92	0.83	0.94	0.73	0.63	0.77	0.8	11809.86	2393.70	5985.64	0.40
	3m	7285	0.74	0.77	0.9	0.8	0.68	0.63	0.86	0.72	0.76	8115.93	2202.64	5604.54	0.39
	Mean±SD	**8820.33** ±1821.53				**0.85** ±0.07				**0.74** ±0.03	**0.79** ±0.03	**10169.09** ±1881.178	**2326.62** ±107.49	**5798.14** ±190.62	**0.40** ±0.01
Injected	3m	9187	0.79	0.74	0.62	0.72	0.73	0.47	0.53	0.58	0.64	11400.6	2320.47	6117.33	0.38
	3m	10966	0.9	0.97	0.97	0.95	0.95	0.93	0.9	0.93	0.94	11202.29	2421.24	5809.44	0.42
	3m	13775	0.85	0.85	0.78	0.83	0.96	0.88	0.82	0.89	0.86	12835.76	2092.05	5147.10	0.41
	Mean±SD	**11309.33** ±2313.19				**0.83** ±0.12				**0.80** ±0.19	**0.81** ±0.16	**11812.88** ±891.37	**2277.92** ±168.67	**5691.29** ±495.79	**0.40** ±0.02
Age mean ± SD		**10064.83** ±2307.83				**0.84** ±0.09				**0.77** ±0.13	**0.80** ±0.1	**10990.99** ±1594.98	**2302.27** ±129.28	**5744.72** ±341	**0.40** ±0.01
Total mean ± SD		**10235.00** ±2070.2				**0.81** ±0.09				**0.76** ±0.08	**0.78** ±0.08	**11003.89** ±1710.04	**2298.72** ±103.33	**5750.92** ±207.22	**0.40** ±0.01

3.3. TRANSDUCTION PROFILE

The final aim of the computational pipeline presented in this work was to evaluate the distribution of the expression levels as a function of the tonotopic position of a given afferent neuron. Given that the raw PV and GFP were not properly aligned, the plugin *Bigwarp* implemented in FIJI was used to align the GFP channel to the PV. Ten landmarks were annotated in both channels and a rotation transform was applied to the GFP channel, resulting in a better alignment, although not perfect. Another aspect to consider is that a normalization of the intensity grey value is needed, since, even with identical imaging conditions, a perfect homogenous illumination is virtually impossible in the cochlea, likely due to the high geometric complexity and the high diversity of biological tissues (decalcified bone, vasculature elements, extracellular cell matrix, the organ of Corti, neurons, etc.) with refractive indexes that differ slightly from that of the dibenzylether, which might generate an accumulation of small optical aberration that degrade the overall quality of the image. Therefore, obtaining an absolute value for fluorescence intensity, using it as a readout of the expression, and comparing it across samples is a very difficult task and it might be more desirable to use other methods closer to molecular biology at the cost of loss of spatial resolution. My attempt to study the distribution of the opsin expression along the tonotopic axis might be useful in order to scale the response of a computational model of an opsin-expressing SGN to the levels of expression and tonotopic position.

To explore the distribution of the relative expression levels in both injected and non-injected cochlea along the length of the cochlea, I generated a substack or 3D ROI of 7x7x4 pixels around the coordinate for each cell, where the average value was calculated. Then, for a given sample, each mean value was divided by the minimum mean values of all the 3D ROI (**Figure 27**). For a clearer display, a box plot is also presented in **Figure 28**. In both conditions, injected and non-injected cochlea, the GFP channel displays an apical-basal gradient (which can also be visually perceived in **Figure 22A**), although in the injected ear the mean values are higher. To classify the cells as positive or negative regarding the expression of GFP, I considered as intensity threshold value the average normalized value plus 1 standard deviation from the non-injected cochlea. This value was 7.45, and resulted in 13% and 38.3% of positive cells, for the non-injected and injected cochleae respectively. Although, it might seem a relative low transduction levels, it is important to remark the fact that the animals used for this quantification were p14 and the injections took place only 8 days before. In former

experiments (Mager et al., 2018), using a different serotype, but same carried protein sequence and animal model, the amount of positive cells at 2-3 months in the injected ear were around 80% and less than 10%, in the non-injected. The choice of such early age was motivated by the fact that similar timepoints have been chosen for the preliminary *in vitro* patch clamp experiments done to characterize the light evoked responses of fast-Chrimson-expressing SGN.

I also tried to study the expression pattern in older animals (3 months), however, presumably due to an antibody depletion effect, the staining was faulty and the study could not be completed. As referred in the discussion section, I observed an intense staining in the outer surface of the ganglion whereas the inner region was almost showing no staining. In case of a high expression of the transduced protein as in our case, the used dilution of the primary antibody might have not provide enough antibodies and have caused the detection of only the more exposed antigens and resulting depletion.

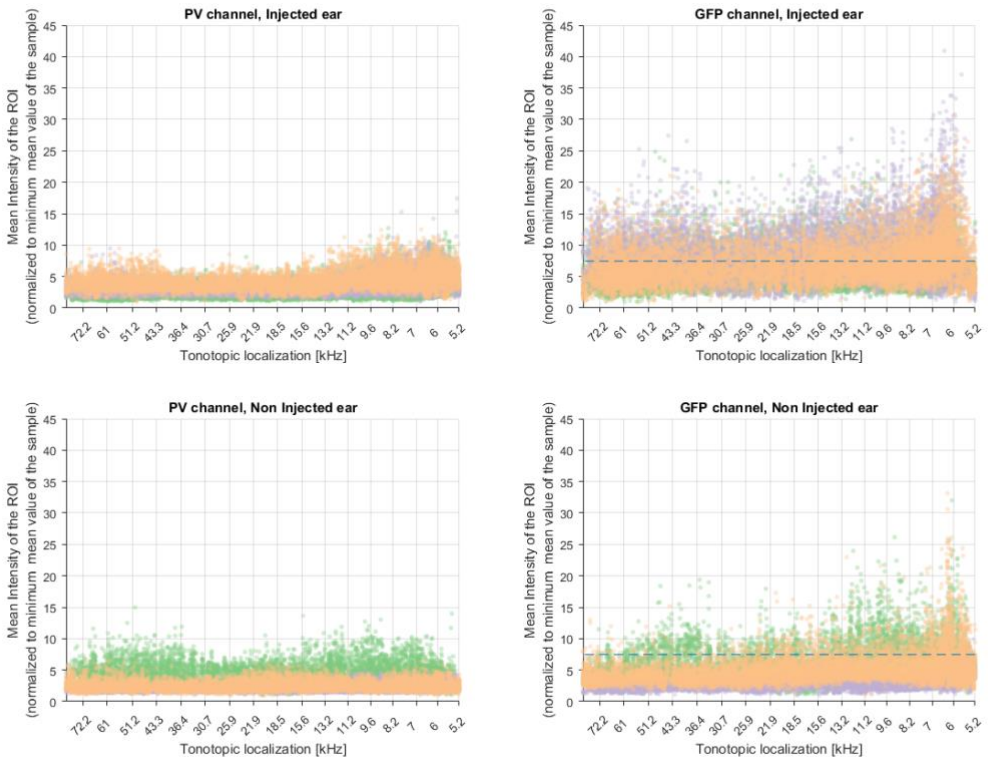

Figure 27. Normalized intensity along the tonotopic axis from p14 mouse cochleae (I). Scatter plot from three cochleae per condition (Injected and non-injected ear from three animals, shown in different color). Left panels, normalized intensity values to the minimum value of the sample of the PV channel. The expression of PV does not have a strong tonotopic dependence (apart from slightly increase of voxel intensity in the apex (low frequency region) and base. Right panel, normalized intensity values to the minimum value of the sample for GFP channel as a proxy of the opsin expression levels. The expression of GFP seems to follow an apical-basal gradient in both ears, with higher values, as expected, in the injected ear. In order to classify cells binarily as positive or negative, the threshold value (depicted as a dashed line) was calculated as the mean + SD of the non-injected ear. This yield a proportion of positive detected SGN of 13% and 38.3% in both the non-injected and the injected ear.

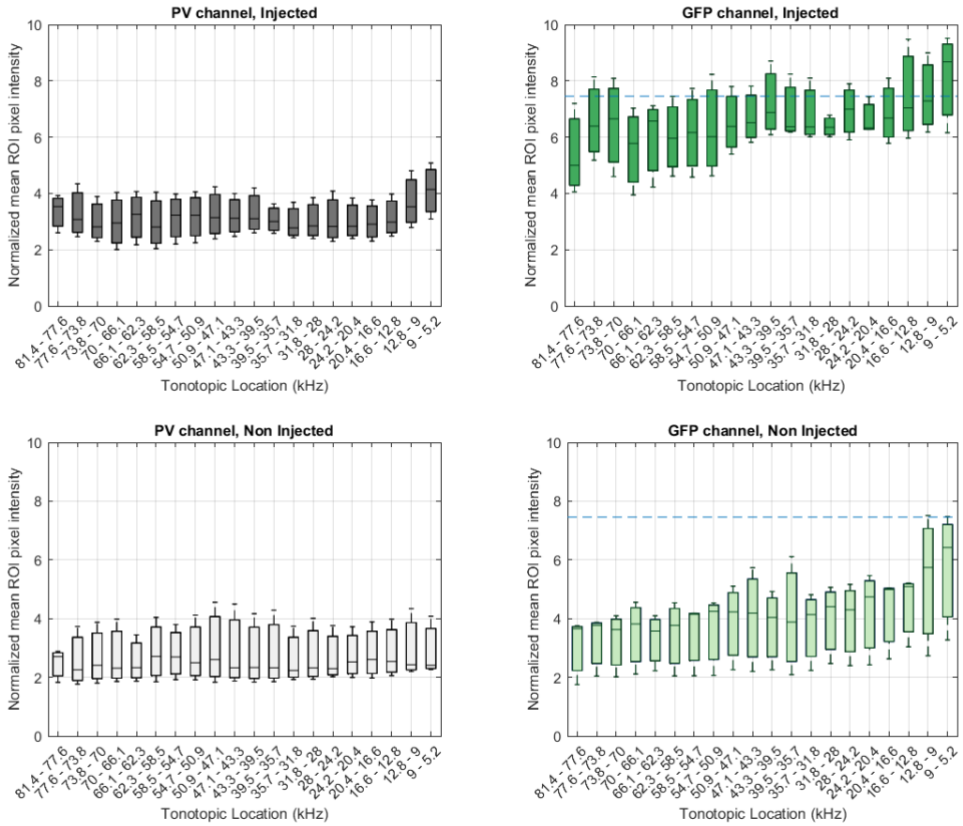

Figure 28. Normalized intensity along the tonotopic axis from p14 mouse cochleae (II). Box plot from three cochlea per condition (Injected and non-injected ear from three animals, shown in different color). The information depicted in this figure is the same as in Figure 27, grouped in tonotopic position intervals and display in a box plot. Likewise, we can perceive relative constant levels of PV intensity and a apical-basal gradient in the GFP staining. Note that in order to classify cells binarily as positive or negative, the threshold value (depicted as a dashed line) was calculated as the mean + SD of the non-injected ear. As mentioned in Figure 27, this yield a proportion of positive detected SGN of 13% and 38.3% in both the non-injected and the injected ear. Each box represents 25th and 75th percentiles (bottom and top edges), median (central mark) and most extreme data points not considered outliers (whiskers).

3.4. INVESTIGATING THE USE OF NANOBODIES TO REDUCE THE INCUBATION TIME

Although the staining and clearing protocol has produced quite promising results, there is a big room for improvement. One of these aspects is the extremely long incubation times (two weeks for each primary and secondary antibody), turning the protocol length to be around 1.5 months, from fixation to imaging. In order to decrease the incubation time, conserving decent penetrance of the staining, we teamed up with Shama Sograte- Idrissi, from Dr. Felipe Opazo´s lab, specialized in the design of probes for microscopy, and decided to explore the use of Nanobodies.

Nanobodies are the recombinant version of the variable domain of heavy chain antibodies and occur naturally in camelids (vg. camels, llamas, alpaca, vicuna) (Hamers-Casterman et al., 1993; Muyldermans, 2013). They have a small size (14–17 kDa) and their volume is 1/10th of the volume filled by standard antibodies, which provides better diffusibility (Perruchini et al., 2009). However, the availability of primary nanobodies is quite reduced in comparison to the wide array of primary antibodies that are commercially available. A recent alternative has been developed to overcome the reduced number of primary nanobodies: secondaries nanobodies targeting the Fc domain from different species (Pleiner et al., 2018). The anti-guinea pig nanobodies we used in this experiment were generated by NanoTag Biotechnologies GmbH (Göttingen, Germany) and were coupled to fluorophores (two molecules per nanobody) by Shama Sograte-Idrissi, who also characterized its advantages over secondary antibodies (i.e. reduced probe-induced clustering and linkage error). Thanks to the monovalency of this type of probes, the primary antibody could be premixed with the secondary nanobody and then, the mix can be incubated with the tissue, removing the need of second incubation step.

We compared a standard staining done with two subsequent incubation of primary and secondary antibody (guinea pig anti-PV plus goat anti-guinea pig) with a premix of the same primary antibody coupled to a secondary nanobody. We tested two different incubation times: 6 and 14 days of incubation (3+3 and 7+7 for the primary and secondary) **(Figure 29 and Figure 30**). In the samples stained with nanobodies, even at the shortest incubation time, we observed a decent and homogeneous penetration (**Figure 29C and Figure 30B**) and an overall good performance of the staining, revealing IHCs and SGNs. Radial line profiles were obtained from the center of the Rosenthal´s canal/spiral ganglion to the outside of the ganglion along the length of the cochlea to quantify the staining penetration. In the samples stained with

nanobodies (**Figure 30B**), a plateau can be observed, as opposed to the samples stained with antibodies for 7+7 days (**Figure 30A**, right panel), in which the profile retrieved had a peak, indicative of a stronger staining at the edge of the ganglion. The gradient seen in the samples stained with antibodies for 7+7 days pinpoint to an insufficient detection of target molecules. The samples stained for 3+3 days (**Figure 30A**, right panel) provided also a plateau but with very low levels, arguing for an insufficient penetration of the staining, if at all, with signals accumulated in the outer bone surface and in the edges exposed to the solution. Thus, in conclusion, the reduction in the size of the labelling molecule seem a very seductive method to shorten our incubation times (Sograte-Idrissi et al., *in prep*).

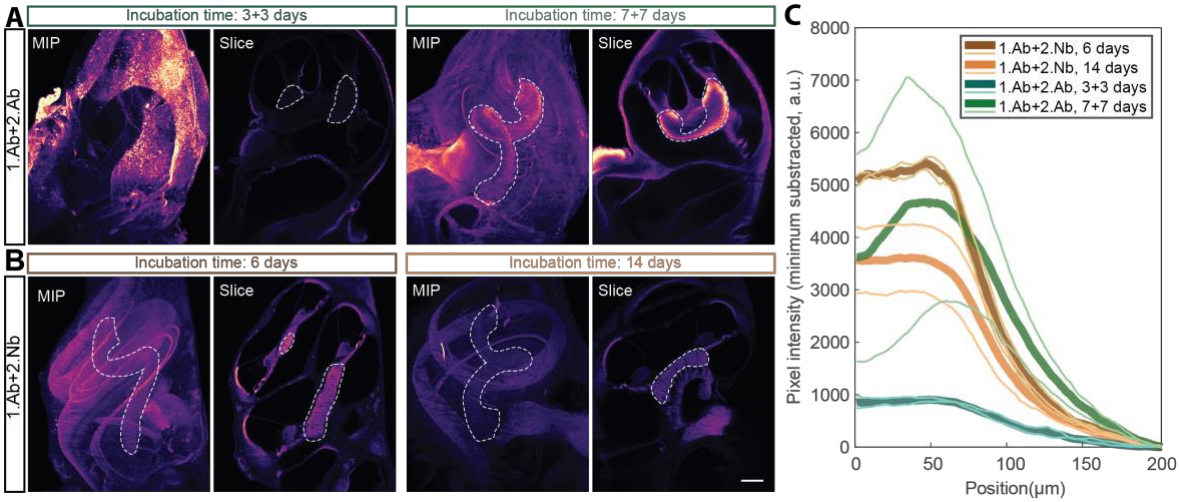

Figure 29. Preincubation of secondary nanobodies with primary antibody decrease the incubation time to obtain a homogeneous staining of the cochlea. MIP and exemplary slice of intact cochleae using different approaches and incubation times in a staining procedure against PV. **A.** Cochleae were incubated with the primary antibody for 3(left) and 7 (right) days followed by a consecutive incubation of the secondary for the same amount of time, respectively. The 3+3 incubation time showed no sufficient penetration of the staining, getting accumulated in the outer bone surface and in the edges exposed to the solution. The 7+7 yields a better staining performance, revealing the hair cells and the neurons. However, in the ganglion, it displays a staining gradient, with stronger signal on the edges, indicative of an insufficient penetration**. B.** Cochleae were incubated with the primary antibody preincubated with the secondary Nanobodies for 6 (left) and 14 (right) days. The staining revealed homogenously the neurons and hair cells, with no apparent effect on the incubation time. **C.** Mean (per sample, thin lines, and per experimental condition, thick lines) pixel line profile from radii crossing the ganglion distributed along the centerline of the ganglion (n=2, per condition). Note the plateau profile depicted by the samples stained with secondary nanobodies, in comparison to the relative flat and pronounced peak profile in the respective samples stained with secondary antibody. Scalebar: 200 µm

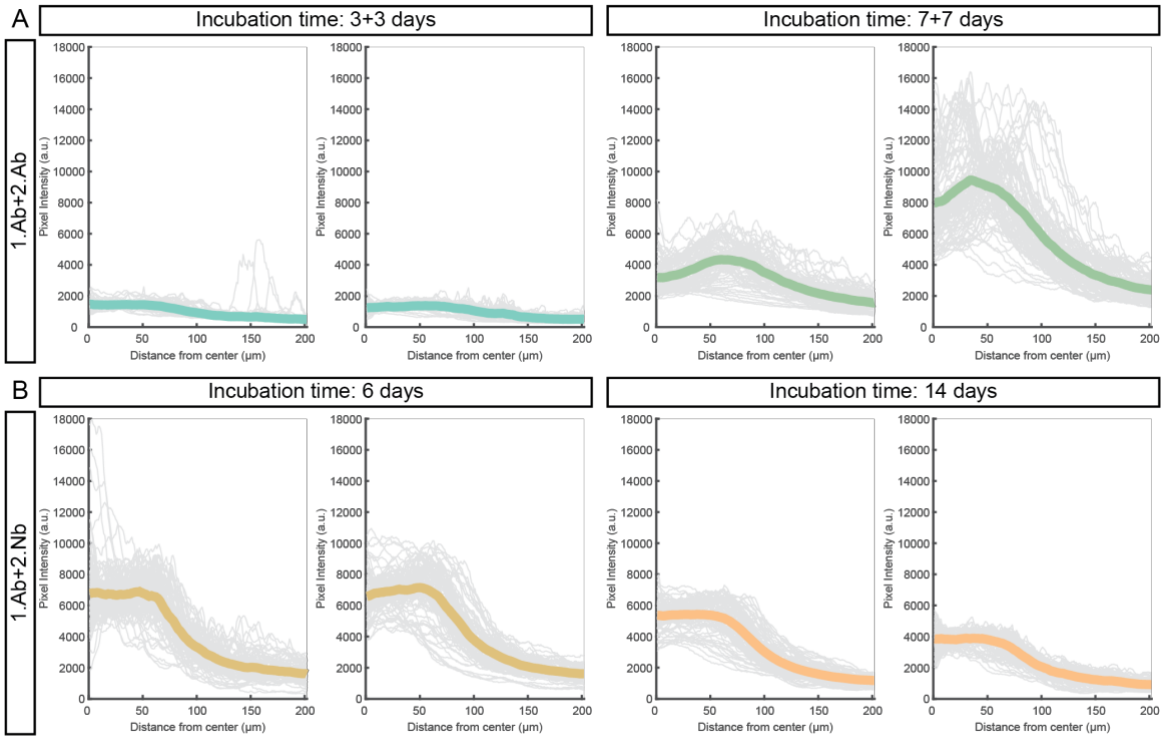

Figure 30. Line profile from individual samples. Mean profile per position (n= 100 per sample, grey thin traces) and mean profile per sample (n=2 per staining method and incubation time, color thick traces) are displayed against distance from center position from **A.** samples stained with a primary antibody against PV premixed with a secondary nanobody against guinea pig, labelled with Alexa Fluor 546, and **B.** samples stained with a primary antibody against PV revealed by a secondary antibody against guinea pig, labelled with Alexa Fluor 568.

4. DISCUSSION

Here, we have shown the compatibility of a clearing protocol, iDisco+, in its methanol-free pretreatment form, with the cochlea to allow a whole mount study of the intact organ. We have introduced some adaptations to improve its performance in the cochlea and successfully tested them in cochleae of different species for stainings of PV, CR, vGlut3, GFP, 7-AAD and lectin. Next, we developed a computational framework to 1) Define and map the tonotopic axis; 2) Count IHCs (manually) and SGNs (semiautomatically); 3) Retrieve intensity values and study them along the tonotopic axis. Finally, I have also explored novel staining strategies, including fluorophore labelled nanobodies, to decrease the time required for the immunolabeling.

To date and my knowledge, all of the experiments aimed to perform fluorescent in toto imaging of the cochlea have been based on the classical Voie et al. 1993 paper, using Spalteholz´s solution (Methyl Salicylate Benzyl Benzoate) and bulk bath in Rhodamine B isothiocyanate. Very few have include a more functional staining using antibodies (MacDonald and Rubel, 2008, 2010; Nolte et al., 2017; Risoud et al., 2017; Schmitz et al., 2014; Schulze et al., 2019) and none of them (apart from the IHC count of Schmitz et al., 2014) has used the immunofluorescence to retrieve cell-based information. The previous approaches have been limited to coarse anatomical structures, extrapolations of cell counts or estimations of cell densities and, in really upstanding, yet scarce, examples, manual counts of the neurons (Johnson et al., 2011; Schmitz et al., 2014). Many of them focused on are the development and/or application of novel imaging techniques (vg. OPFOS, sTLSIM, SLOT), rather than on biological questions. Thus, the work carried out here pursuit to contribute to the advance of the current techniques and applied to it to quantify two key parameters in preclinical gene therapeutic and optogenetic approaches to hearing restoration: counts of IHCs or SGNs and counts of transduced cells. Nevertheless, as any technique in its relative starting stage, there is a big list of limitations and also a lot of room for improvement, that I discuss in section 4.3.

4.1. IHCS AND SGNS COUNTS

The number of studies addressing the numbers of IHCs in the mouse cochlea is more limited than for SGNs. Ehret and Frankenreiter, 1977 reported a total of 765 IHCs in 6-8 weeks old NMRI mice. Schmitz et al., 2014, using sTSLIM, clearing and a Myo7a staining, estimated the

number of IHCs to be 685±10(SEM) in 15 weeks old CBA mouse. Another study, by Tong et al., 2015, found in CBA mice with 4-25 days, approximately 11 cells per 100 μm, which assuming a mean BM length of 6 mm results in 660 cells. Our estimates of 646.5 ±19.56 (p14) and 639.54 ±21.72 (3 months) do not differ substantially from those and any dissimilarity could be due to the different strains employed.

Regarding SGNs counts, Johnson et al., 2011; Richter et al., 2011 and Schettino and Lauer, 2013, in their respective publications, gathered very valuable information from the literature, which are summarized and further completed in **Table 8**, along with our current results. It reveals substantial variability in term of cell counts and methodologies followed. Thus, all the values in the literature yield an average ±SD of 7919.18 ±4232.53 SGNs in the mouse cochlea. Our values (uncorrected) are 10405.17 ±2301 (p14) and 10064.83 ±2307.83 (3 months), falling into the average range. However, when compared to the mean of only those studies using C57Bl6 and C57Bl6 hybrids (see table, mean±SD, 5572.93 ±2689.8), our estimates exceed the published ones, even when we are considering only type I SGNs (PV positive neurons). Over- or underestimation in our or their work, respectively, could result from different methodologies used or in features of different C57Bl6 colonies. A series of more complete experiments using different markers could further support or refuse our estimates.

Table 8. Spiral ganglion neuron counts across the literature. Modified after (Johnson Et Al., 2011; Richter Et Al., 2011; Schettino And Lauer, 2013)

Publication	Strain	Age (days)	Section thickness (µm)	Section sampling fraction	Structure	Staining agent	Counting method	Correction factor	Spiral ganglion neuron population	Error
Ehret, 1979	NMRI	28-70	3	25 cross-sections of cochlear nerve	Afferent fibers	Silver nitrate	Profile counts	None	10483	~ 810 SD (n = 6)
Webster, 1985	CBA/J (heterozygous deafness mice)	Adult	4	Every 10	Cell body	Toluidine blue	Profile counts	None	12577	1587 SD (n=5)
Park et al., 1990	C57BL6/6NNia mouse (diet)	540	8	4	Nucleoli	Hematoxylin/ Eosin	Profile counts	Konigsmark, 1970	3132.33	382.2 SD (n=6)
Park et al., 1990	C57BL6/6NNia mouse (no diet)	540	8	4	Nucleoli	Hematoxylin/ Eosin	Profile counts	Konigsmark, 1970	2399.5	542.1 SD(n=6)
Fariñas et al., 1994	C57Bl6	0	10	Every 6th	Nucleoli	Cresyl violet	Profile counts	None	8082	1132 SEM (n = 3)
Liebl et al., 1997	C57Bl6	0.5	5	Every 6th	Nuclei	Hematoxylin	Profile counts	None	4421	1325 SEM (n = 3)
Camarero et al., 2001	MF1x129/sv	5	50	Every 2nd	Nuclei	Cresyl violet	Stereology, optical fractionator	Jensen and Gundersen, 1993; Tandrup et al., 1997	16100	700 SD (n = 3)
Camarero et al., 2001	MF1x129/sv	20	50	Every 2nd	Nuclei	Cresyl violet	Stereology, optical fractionator	Jensen and Gundersen, 1993; Tandrup et al., 1997	16600	600 SD (n = 5)
Postigo, 2002	129xC57Bl6	7	8	Every 5th	Nuclei	Cresyl violet	Profile counts	Abercrombie, 1946	~7800	~ 300 SD (n = 3- 4)
Postigo, 2002	129 C57Bl6	70	8	Every 5th	Nuclei	Cresyl violet	Profile counts	Abercrombie, 1946	~8000	~ 100 SD (n = 3- 4)
Agerman, 2003	C57Bl6	0	14	Every 3rd	Nucleoli	Cresyl violet	Profile counts	Abercrombie, 1946	~6500	~ 500 SEM (n = 4)
Agerman, 2003	C57Bl6	17	14	Every 3rd	Nucleoli	Cresyl violet	Profile counts	Abercrombie, 1946	~6800	~ 300 SEM (n = 4)
Luikart et al., 2003	C57Bl6	0	8	Every 10th	Cell bodies	Cresyl violet	Profile counts (computer automated)	None	7148	291 SEM (n = 5)
Whitlon et al., 2006	CD-1	1	5	Every cell	Nuclei	Toluidine blue	Reconstruction	None	8240	423 SD (n = 3)
Johnson et al., 2011	CBA/JCr	28	5 (resampled at 10)	Every cell	Cell bodies	Rhodamine B isothiocyanate	Reconstruction, manual count	None	8626	96 SEM (n = 5)
Richter et al., 2011	C57Bl6/ 129Svj	70	5	Every cell	Cell bodies	Toluidine blue	Reconstruction	None	10402	Not reported
Schettino and Lauer, 2013	C57Bl6	56-77	40	Every 2nd	Cell bodies	Osmium	Stereology, optical fractionator	None	7009	996 SD (n = 4)
Schmitz et al., 2014	CBA/JCr	84	5 (resampled at 10)	Every cell	Cell bodies	Rhodamine B isothiocyanate	Reconstruction, manual count	None	8617	341 SEM (n = 3)
Present work, 2019	C57Bl6	14	4 (resampled at 2)	Every cell	Cell body	PV	Hough Transform (semiautomated)	None	10405.17	2301 SD (n = 6)
Present work, 2019	C57Bl6	90	4 (resampled at 2)	Every cell	Cell body	PV	Hough Transform (semiautomated)	None	10064.83	2307.83 SD (n =6)

4.2. GFP DISTRIBUTION IN THE INNER EAR OF INJECTED MOUSE

Our experiment on the estimation of the tonotopic distribution can serve as a proof-of-concept of the capabilities of the tools presented in this thesis. It revealed an apical-basal gradient of fast-Chrimson expression in the auditory spiral ganglion neurons at p14, 8-9 days after the injection of viral particles through the round window, in both injected and non-injected (contralateral) cochleae. From our investigations in the mouse cochlea, the data presented in Mager et al. 2018 and in Keppeler et al. 2018, shows a similar tendency. Likewise, others have reported an apical-basal gradient of the expression of the transgene in mouse by different cells in the sensory epithelium (György et al., 2019; Kim et al., 2019; Suzuki et al., 2017). One explanation could be the different permeabilities of the different cochlear components. For the cells populating the organ of Corti, Suzuki et al 2017 hypothesized that the transduction might be happening through the basilar membrane rather than the Reissner's membrane. They hypothesized that after their injection into the perilymph of the posterior canal and the entering of the injected fluid through the scala vestibuli of the basal turn, the fluid would spiral up until the helicotrema. Given that the sensory epithelium is separated from the scala vestibuli by the Reisnner´s membrane and the scala media, it is less likely that the virus can access the target cells. Thus, a basal-apical gradient in the scala vestibuli, and an apical-basal gradient in the scala tympani, of the virus concentration is generated. When the viral particles reach the scala tympani, they can penetrate through the basilar membrane and reach the basolateral surface of the hair cells.

Their elaborated explanation could be a valid one, however it would not explain the same apical-basal gradient we observed in the non-injected ear, at least partially. In that case, the reason for the pattern should lie on anatomical/physiological reasons rather than in the injection mode. Therefore, let us assume that at a given time, after the injection and before the transduction, there is a relative homogeneous distribution of the virus in the perilymph. Then, if we agree with the authors that the transduction occurs mostly through the BM (given that the ST is closer to the cells than the SV) and consider that the BM is thinner and wider in the apical region (Burda et al., 1988), we can conclude that this region facilitates the transfection of the cells, generating this apical-basal gradient. For the SGNs, given that their somas are housed in the Rosenthal's canal, flanked by bone, the likely entry pathway is through the lamina perforata, along the track followed by their peripheral processes. Thus, the same explanation for IHC and OHC could be applied to SGNs' transduction pattern too.

If injected and non-injected ear are compared, a similar transduction pattern can be observed, even though the number of positive cells was typically lower in the non-injected one. Contralateral expression of virus-delivered genes is common and has been previously documented (Keppeler et al., 2018; Li Duan et al., 2002; Staecker et al., 2001; Stöver et al., 2000). In the latter (Stöver et al., 2000), using guinea pig, as an animal model, and adenovirus, as the gene vector, the authors even achieved bilateral transduction of the transgene after injection in the CSF through a lumbar puncture, arguing that this space is the pathway that the viral particle use to reach, through the cochlear aqueduct, to the other contralateral cochlea. They argued that, when injecting in the inner ear, an increase of pressure in the scala tympani, might push perilymph and injected fluid through the cochlear aqueduct reaching the CSF space. Here, the virus gets distributed and reaches, through the contralateral cochlear aqueduct, the contralateral perilymphatic space. They also claimed that the contralateral expression was highly dependent on the volume injected. Along these lines, Gyorgy et al. 2017 reported minimal contralateral expression after injecting 250 nl of virus-containing fluid through a cochleostomy in mouse. Low volumes (vg. ~ 0.250 µl for mouse and ~25 µl for guinea pig) seems also to result in baso-apical gradients in the injected cochlea (György et al., 2017; Li Duan et al., 2002; Stöver et al., 2000), although it could also be that different serotypes and promoters have an effect on the distribution (Gu et al., 2019).

The systemic spread of the AAV- and other viruses might limit the potential for translation of our current approach, that is ameliorated by the specific neuronal promoter include in the virus and it is been currently studied through biosafety studies. Further research on more specific promoters (restricted to SGNs) or on virus serotypes with a specific tropism would be need it. Another strategy that might help limiting the expression of the transgene only in those cells exposed to light might be the use light-inducible transcription factors, such as, for example, the blue-shifted TALE-CRY2/CIB1 system (Konermann et al., 2013) or the red-shifted PhyB–PIF6 (Müller et al., 2013). These and others (reviewed in Polesskaya et al., 2018) suffer from the fact that the light-sensitive transgenes are big and therefore, sometimes difficult to pack inside of viral vectors, something that the development of more spacious virus could mitigate in the future.

4.3. LIMITATIONS OF THE APPROACH

4.3.1. LONG INCUBATION TIME

In November 2015, during a Workshop organized by Dr. Camin Dean, Dr. Christian Vogl and I conducted the first pilot clearing experiments. I still remember the excitement of the book-quality images that the staff from LaVision, who were operating the workshop´s microscope, were displaying in the computer's screen. Back then, I was not aware of all the previous work of Voie, Johnson, Santi and the rest, so in my naïveness, it was the first time that I saw fluorescent optical sections obtained from an entire cochlea. Our initial thrill was a bit blurred by the fact that the inside of the ganglion showed little or none staining. Lucky enough for us, one of the experts in the tissue clearing field, Alain Chédotal, saw our samples and he encouraged us to repeat the experiment and extend the incubation time from 7 days (what is recommended in the original publication) to 14 days. I followed his advice and the next samples I processed, I obtained a homogenous staining. However, it also had a drawback: it resulted in an extremely long protocol expanding to approximately 1 month and a half (from fixation to clearing). The problem of combining whole cochlea imaging and immunostainings have been already commented on (Johnson et al., 2011; MacDonald and Rubel, 2008) and could explain the lack of extensive studies using the combination of both. To my knowledge, we have been the first ones to use immunostaining of the spiral ganglion neurons using 2 + 2 weeks incubation time in combination with clearing and lightsheet microscopy. Given the high amount of information that can be obtained from a single experiment, it might be a condition that one can accept, although reducing the time, without losing staining quality, is certainly desired.

In the last stage of this work, we engaged in a collaboration with Shama Sograte-Idrissi and Felipe Opazo in order to test their recently developed fluorophore-coupled secondaries nanobodies with our clearing protocol. While this first approach showed promising results, since it allowed the identification of the PV positive cells in very few days, this was at the cost of obtaining a prominent background. Since high background in nanobodies staining has been reported previously (Perruchini et al., 2009), it seems that working towards a more specific probes, applying stronger washing steps or using specific reagents (vg. Image-iT™ FX Signal Enhancer ReadyProbes (MacDonald and Rubel, 2008; Nolte et al., 2017)) to decrease the background staining is highly recommendable.

Additionally, other approaches should be tested in the future to facilitate antibody penetrance and decrease the incubation time, while maintaining a decent signal-to-noise ratio. The use of the methanol-based pretreatment is the recommended method in the iDisco+ publication (Renier et al., 2016), however it requires the validation of the target antibody. The antibodies used in this dissertation were well established in the lab and have been widely used for various studies (some examples include (Keppeler et al., 2018; Mager et al., 2017; Vogl et al., 2016; Wrobel et al., 2018)). Lead by the will of using exactly the same antibodies, I therefore, implemented the methanol-free pretreatment basing on the idea that an easier transfer from other antibodies used with other protocols, such as whole-mount immunolabeling of excised organs of Corti followed by confocal microscopy, could take place, since methanol might be incompatible with many antibodies (iDisco webpage). However, the assumption of the use of methanol-free pretreatment would not interfere with the staining of antibodies shown to work previously might be not totally correct. For example, Soto-Prior et al. (1995) discussed that the lack of PV immunoreactivity in the ear the Yamagishi et al., 1993 paper might be due to the fact that the antibody they used recognized an epitope in the calcium binding site in the present of calcium. After decalcification, the folding of the protein might have changed, rendering it unrecognizable by the antibody. This could be of special consideration if stainings against proteins with calcium Ca^{2+} binding domains (for example, C2C domain in otoferlin) are not successful. Another explanation could be that if the soluble proteins are not well fixed by PFA, after the permeabilization and the removal of lipids, these soluble proteins could be potentially washed away, resulting in a false negative signal. In this case, reducing or even removing the incubation with dichloromethane could be tested.

Apart from optimizing the staining for the methanol pretreatment, other permeabilizing agents as acetone can be tested (Abcam). Another approach could be the recently developed electromagnetic focused immunohistochemistry EFIC, which according to their authors, *"could stain thick brain tissues uniformly and rapidly (up to 3 mm deep sample within 4 h) with only a limited amount of antibody (typically 50 μg/reaction)"* (Myeongsu et al., 2019) or, along the same lines, applying stochastic electrotransport of antibodies (Kim et al., 2015). In addition, the use of microwaves could be an option to consider, as recommended by (MacDonald and Rubel, 2008), either to increase the decalcification efficiency (Tinling et al., 2004) or the antibody penetration, during the incubations (Muñoz et al., 2004; Owens et al., 2013).

4.3.2. IMAGE QUALITY

The overall image quality, upon optimal penetration of the antibody, is predominantly good. However, it is not perfect. The embedding of the sample in DBE is done to reduce the RI mismatch between the cellular and tissue components and the medium in which they are suspended. As I presented in the introduction, the amount of different RI belonging to the different components (vg. decalcified bone, vasculature elements, extracellular cell matrix, the organ of Corti, myelinated and non-myelinated neuronal components, etc.) is vast. Therefore, achieving a homogenous RI throughout the cochlea is unlikely achievable. Thus, spherical aberration occurs at each RI interface, blurring the final image (Richardson and Lichtman, 2015). This, together with its high geometric complexity, causes that despite having similar imaging conditions, a perfect homogenous illumination is virtually impossible in the cochlea, obtaining areas that might receive less light or even unfocused light, which might generate an accumulation of small spherical aberration that when summed degrades the quality of the image.

One of the issues that our current imaging strategy faces is the anisotropy of the imaging, limiting the Z-resolution to the minimum thickness of the lightsheet, ie. 5µm. This is more evident when the inner hair cell row is closely analyzed, being easily resolvable when it is situated in the XY plane and less when is parallel to the acquisition axis. One of the most important challenges in lightsheet microscopy is to achieve a good section ability (i.e. good axial resolution) along a wide field of view, which implies high NA both for illumination and detection. While numerous advances are occurring at the experimental level (see (Power and Huisken, 2017)), they are far from being in a commercially available solution.

One implementation that might be worth trying is the Multiview acquisition. This imaging modality combines principles of optical tomography with the lightsheet microscope. It improved notably the sharpness, contrast, uniformity and isotropy of the optical sections, and it can achieve even subcellular resolution (Bassi et al., 2015; Swoger et al., 2007). However, our current lightsheet microscope does not provide this functionality (present, for example, in other commercial solutions as in the Zeiss Lighsheet Z.1 – although this is not compatible with organic-solvent-based clearing protocol). To overcome this, and also in the seek of a plug-and-play mounting solution, I have designed a magnetic holder that allows the rapid mounting of the sample in the microscope holder and the rotation of the sample, although not in an accurate, controlled way **Figure 31**. The sample is fixed initially to a cylindrical 3x2mm N42 Neodymium magnet (containing an alloy of nickel-cooper-nickel and neodymium/iron/boron

material, Schlößer Baustoffe®) with Loctite® 401 (ethyl-cyanoacrylate glue) by the semicircular canals. The magnet can be kept in DBE for more than 7 months without any visible signs of deterioration (further time is under testing). Prior to the imaging, the sample with the magnet is carefully placed on top of the holder magnet (of similar characteristics), with some magnetically soft forceps (some type of stainless steel or plastic). Since it is a magnetic interaction it allows a coaxial rotation of the sample. Furthermore, the presence of two orthogonally placed magnets allows an additional degree of freedom. Thus, consecutives stacks can be acquired, modifying the rotation angle in between.

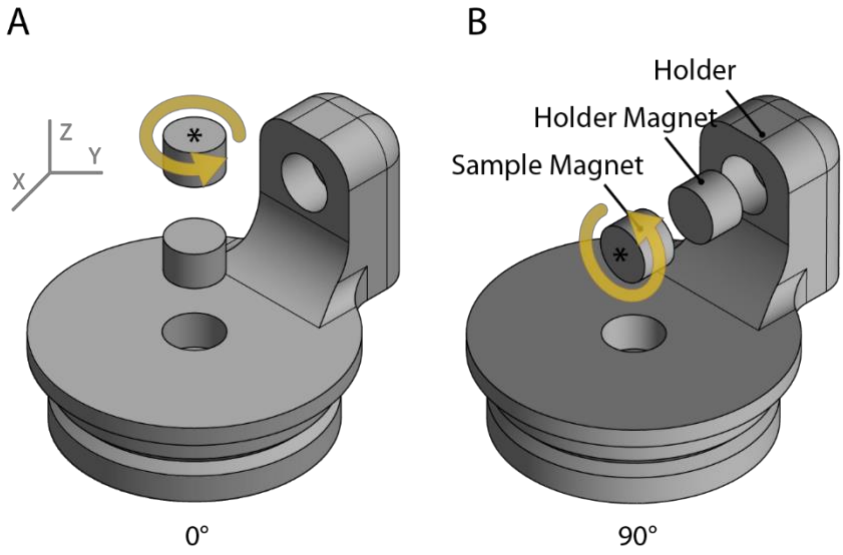

Figure 31. Custom-made magnetic holder for single- and multi-view imaging. Schematic 3D view of the designed holder and a pair of magnets. The holder magnet is permanently attached to it by pressure. The further is glued to the sample. *, depicts where the sample is glued. Yellow arrow, illustrate how it can be used for multi-view acquisition by rotating the sample. **A. and B.** Displays the two perpendicular axis in which the sample can be placed.

In my design process, I realized that the main polymers used in standard 3D printing, namely PLA or ABS, are not compatible with DBE. Therefore, I did a screening of the materials that can be used in our in-house workshop for the construction of the holder, POM being the one selected.

Table 9. Materials compatible with Dibenzylether

Material	Resistance	Reference
Polyoxymethylene (POM)	Excellent	1, 2
Teflon (FEP, PTFE)	Excellent	1,2,3,4
Stainless steel	Excellent - Very good	1,4,5
Nylon PA 12	Excellent	6,7
Polypropylene	Sufficient	2
High Density Polyethylene	Good	2

1, https://www.buerkle.de/files_pdf/wissenswertes/chemical_resistance_en.pdf
2, https://www.kartelllabware.com/m/docs/files/kartelllabware-tech-manual-spa-eng-por-.pdf
3, https://www.masterflex.de/fileadmin/user_upload/se_website/produkte/masterflex_chemical resistance_en.pdf
4, https://www.fillrite.com/dam/2335.pdf
5, https://www.haywardflowcontrol.com/images/flowcontrol/pdf/chemchart.pdf
6, https://www.professionalplastics.com/professionalplastics/chemicalresistancechartofplastics.pdf
7, http://usglobalimages.stratasys.com/main/files/material_spec_sheets/mss_fdm_materialschemicalcompatibility.pdf?v=635785201776733916

Although the Multiview capacities of this device are to be tested (for example, with the Multiview Registration plugin of FIJI), the holder itself eases the task of mounting the sample in the microscope. The mounting solution provided by LaVision consisted in a sample holder in which the specimen is fixed with a screw. My motivation to improve the sample holder system started with the initial imaging sessions, in which either the sample was too loosely fixed and lost in the middle of the imaging acquisition or cracks were appearing in the sample due to a too tight fixation. Thus, during most of my experiments, I directly glued the samples to a handcrafted epoxy block with cyanoacrylate glue. Given that this approach was not totally optimal, in the last period of my thesis, I designed the new sample holder described. With both approaches, however, there is always the risk of introducing optical aberrations in the most basal part of the specimen if an excess of glue is present (although it is removable with several acetone washes, without loss in the sample quality). The glue sometimes can even reach the cochlea, reducing the clearing performance and the further usability of the cochlea. This is due to the fact that Ethyl-Cyanoacrilate glue have a RI of 1.45 and DBE 1.56, causing a refractive index mismatch and negatively affecting the optical clearing. Therefore, one possible solution would be to survey and test adhesives with RIs closer to that of DBE that are also chemically resistant, such as the NOA 72 (Norland® Products), which is an optical adhesive with a RI of 1.56 and will be tested in the short future.

4.3.3. TONOTOPIC CLASSIFICATION

The approach presented here to assign a frequency label to specific cells is merely based on geometric constrains and does not have any physiological meaning, since it is based on arbitrary criteria, as the nearest neighbor distance and the maximum number of cells per frequency label. The initial assumption was that cells located more apically should have a lower frequency, and that the distribution towards the base should follow the Greenwood function. However, an exhaustive description of the distribution of cells in the ganglion within the same tonotopic region is missing. One aim would be to describe the presumable intensity axis (orthogonal to the tonotopic one), as in the cat cochlea (low- to med- SR in the SV side, high SR in the ST side (Kawase and Liberman, 2004; Leake and Snyder, 1989; Leake et al., 1992)). To address this question one could characterize the electrophysiology by single unit recording in the auditory nerve (characteristic frequency, dynamic range, spontaneous rates, for example), followed by loading the recorded cells with horseradish-peroxidase, a dextran fixable dye or any other kind of fixable retrograde tracer and image the whole cochlea after performing the clearing protocol. Then, the Cartesian coordinates of the cell detected should be converted in some form of ganglion self-referenced coordinate system and that could also be related to the position of the peripheral process. The downside of this approach would be the high number of animals needed to have a comprehensive description of the ganglion anatomy and its relation to the tonotopic distribution. As an alternative, a revisit to the data of previous back-tracing papers (for example, those by Markus Müller in the cochleae of different animals), including a 3D reconstruction of the ganglion, registration of the position of a SGN within the ganglion and its BM correspondence, could generate the requested model removing the need of new experiments. Another way to corroborate the BM - ganglion correspondence, could be tracing the scattered fluorescent neurons present in the $Mafb_{CreERT2}$;Ai9 transgenic line (in a similar fashion as (Shrestha et al., 2018) used for their expression analysis).

To my knowledge, only the “Cochlear Frequency Mapping in Whole Mounts” plugin from the Eaton-Peabody lab (Eaton-Peabody Lab) is available to accomplish the tonotopic labelling. However, it is not designed to work on 3D datasets and there is no documentation available regarding the origin of the mapping parameters. Given this, the tonotopic mapping tool, which is compatible with different imaging modalities and provides referenced sources for the Greenwood´s function fitting, might prove generally beneficial for the auditory research community. The only downside might be the fact that is written in Matlab, so the spreadability of the software might be limited.

4.3.4. CELL DETECTION AND QUANTIFICATION

The cell detection workflow presented in this work suffers from a relatively tedious implementation (possible less than counting manually 42,500 cells as done by Johnson et al. 2011), in which the image has to go through a series of preprocessing and processing supervised steps, with parameters manually defined by the user.

From the bench side, some he combination of nuclear stainings (TO-PRO3 or 7AAD, also suggested by Johnson 2011) with a target cell marker, and use the latter as a mask for the nuclear staining stack could potentially improve the current methodology. In this case, the input for the analysis (the segmented nuclei), as mention before, would provide a more robust sphere, which might improve the detection routine.

From the computational side, given the relative variability in cell shapes and size, a content-aware strategy probably is more desirable. The use of deep learning strategies (e.g. U-net, (Falk et al., 2019)), although they require an initial training phase with thousands of labelled datasets, could provide a more robust, accurate and automatized pipeline.

4.3.5. ANTIBODY DEPLETION

One phenomenon that was observed in the samples corresponding to the 3 months old injected mice was the absence of deep staining in the most apical part of the cochleae, more prominently in the injected ear (**Figure 32**). In the "FAQ and troubleshooting" section of the resource webpage of iDisco, the authors claimed that this pattern is more likely due to the depletion of the antibody. Since the expression of the opsin and GFP is lower at basal regions and in the contralateral cochlea, if the explanation provided would be true, the depletion effect should be more prominent in the apical part of the injected cochlea. The overexpressed GFP might have bound all the antibodies available in those areas more exposed to the liquid filled compartments. Indeed, a higher gradient of the signal, with staining very dim signal at the center of the ganglion and a strong staining at the edges, can be appreciated in the apical part of the injected ear (**Figure 32**). Thus, it can be concluded that the current concentration of antibody used is not enough to reveal robustly the expression GFP across the ganglion. For this reason, these samples were removed for the analysis of the GFP distribution. For future experiments aimed to study the changes of distribution of the transduced protein during development, a higher concentration of the antibody will be needed.

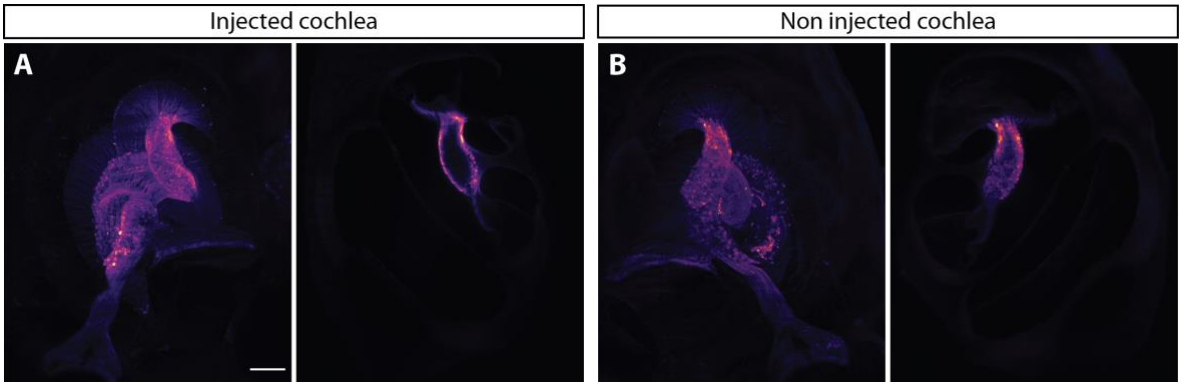

Figure 32. Example of possible antibody depletion in cochleae from an injected animal (GFP staining). A. Injected ear. **B.** Non-injected ear. Right panel shows an exemplary slice, left panel a MIP. Note the deeper level of staining reached in the non-injected cochlea, whereas in the injected one a stronger staining can be appreciated extremely confined to the edge of the ganglion. Scalebar:200µm

4.4. OUTLOOK

Although it is taking relatively long (it has passed around 26 years after Voie´s OPFOS paper) to become a routine technique in the field of auditory research, the increasing availability of lightsheet microscopes in microscopy facilities around the world and the increasing use of this methodologies in neuroscience, will presumably help to the establishment of cochlea clearing and immunostaining as a routine histological procedure.

As an optimistic outlook, I want to picture a future in which a complete open source solution allows the automatic and robust study of multimodal cochlea images in a form of a FIJI or 3D Slicer plugin or a Python library. The platform/software should include modules that permit the user the coarse description of cochlear morphology (length, volumes, centerlines, curvature, height, widths and cross-sectional areas of the scalae, Rosenthal´s canal and modiolus), count cells and map them in the tonotopic space (at least for SGN, IHC and OHC) and perform synapses counts (at least for confocal images). It would require a multidisciplinary team and collaboration across already well stablished groups since the individual components are either already developed or under development. Some of these examples include the synaptic counts using CtBP2 staining in confocal images (Meyer et al., 2009), the automatic segmentation of cochlea images from human CT and the automatic measurement of morphological descriptors in cochlea using CT (Demarcy et al., 2017) or the semiautomatic approach to count SGN presented in this work that could be potentially implemented for IHCs and OHCs. It would be useful to count with parametric models of the cochleae of the main animals used in auditory research were one could register a given sample,

as it is done in many other areas of neuroscience (ClearMap, (Renier et al., 2016)). However, this is not a new idea. Initially steps towards a mouse cochlear morphological repository was already started by Santi et al. with the development of the mouse cochlear database (Santi et al., 2008) or towards a cochlear genetic and molecular database have been also started with the gEAR portal (https://umgear.org/). Going through the literature, it seems that, not surprisingly, I have not been the only one with this thought. In 2011, Johnson et al. finished their inspiring paper with the following sentence:

> *" TSLIM also has the potential to facilitate studies of protein expression gradients in the developing and adult ganglia, which continue to be an important area of research (Rubel and Fritzsch, 2002; Whitlon et al., 2006). Using TSLIM it should be feasible to automatically count every neuron that is positive for a protein of interest in an intact cochlea by co-localizing neuron-specific antibodies and fluorescent nuclear stains. The challenge will be to label whole cochleae with antibodies. We have successfully labeled hair cells with myosin VII and prestin antibodies and all of the nuclei in a cochlea with a fluorescent DNA label (data not shown). Data from such experiments could potentially be combined into a 3D probabilistic atlas. Such data repositories are becoming increasingly common in brain research but are notably missing in the auditory field. A database and coordinate system that stores location-specific anatomical and functional data for the cochlea would greatly benefit the field."*

Thus, although the antibody staining issue seems to be a relatively solved problem (this work), there is an exciting, yet long, road towards a multimodal cochlea-focused image analysis solution, which has to be user-friendly and open-source and that, I presume, will boost the adoption in the auditory field of this and similar clearing techniques to study the whole intact cochlea.

REFERENCES

Abcam. Fixation and impermeabilization in IHC/ICC.

Abercrombie, M. (1946). Estimation of nuclear population from microtome sections. The Anatomical Record *94*, 239–247.

Adamantidis, A., Arber, S., Bains, J.S., Bamberg, E., Bonci, A., Buzsáki, G., Cardin, J.A., Costa, R.M., Dan, Y., Goda, Y., et al. (2015). Optogenetics: 10 years after ChR2 in neurons—views from the community. Nature Neuroscience *18*, 1202.

Agerman, K. (2003). BDNF gene replacement reveals multiple mechanisms for establishing neurotrophin specificity during sensory nervous system development. Development *130*, 1479–1491.

Atkinson, P.J., Wise, A.K., Flynn, B.O., Nayagam, B.A., and Richardson, R.T. (2014). Viability of Long-Term Gene Therapy in the Cochlea. Sci Rep *4*.

Bassi, A., Schmid, B., and Huisken, J. (2015). Optical tomography complements light sheet microscopy for in toto imaging of zebrafish development. Development *142*, 1016–1020.

Bear, M.F., Conners, B.W., and Paradiso, M.A. (2015). Neuroscience: Exploring the Brain. (Baltimore: Wolters Kluwer Health).

Von Bekesy, G. (1960). Experiments in hearing (McGraw-Hill).

Berglund, A.M., and Ryugo, D.K. (1987). Hair cell innervation by spiral ganglion neurons in the mouse. J. Comp. Neurol *255*, 560–570.

Bernstein, J.G., Han, X., Henninger, M.A., Ko, E.Y., Qian, X., Franzesi, G.T., McConnell, J.P., Stern, P., Desimone, R., and Boyden, E.S. (2008). Prosthetic systems for therapeutic optical activation and silencing of genetically-targeted neurons. Proc Soc Photo Opt Instrum Eng *6854*, 68540H.

Bevilacqua, F., Piguet, D., Marquet, P., Gross, J.D., Tromberg, B.J., and Depeursinge, C. (1999). In vivo local determination of tissue optical properties: applications to human brain. Applied Optics *38*, 4939.

Bi, X., Xie, T., Fan, B., Khan, W., Guo, Y., and Li, W. (2016). A Flexible, Micro-Lens-Coupled LED Stimulator for Optical Neuromodulation. IEEE Transactions on Biomedical Circuits and Systems *10*, 972–978.

Bogovic, J.A., Hanslovsky, P., Wong, A., and Saalfeld, S. (2016). Robust registration of calcium images by learned contrast synthesis. In 2016 IEEE 13th International Symposium on Biomedical Imaging (ISBI), (Prague, Czech Republic: IEEE), pp. 1123–1126.

Bosschaart, N., Edelman, G.J., Aalders, M.C.G., van Leeuwen, T.G., and Faber, D.J. (2014). A literature review and novel theoretical approach on the optical properties of whole blood. Lasers in Medical Science *29*, 453–479.

Boulland, J.-L., Qureshi, T., Seal, R.P., Rafiki, A., Gundersen, V., Bergersen, L.H., Fremeau, R.T., Edwards, R.H., Storm-Mathisen, J., and Chaudhry, F.A. (2004). Expression of the vesicular glutamate transporters during development indicates the widespread corelease of multiple neurotransmitters. The Journal of Comparative Neurology *480*, 264–280.

Boyden, E.S., Zhang, F., Bamberg, E., Nagel, G., and Deisseroth, K. (2005). Millisecond-timescale, genetically targeted optical control of neural activity. Nat. Neurosci. *8*, 1263–1268.

Braun, F.J., and Hegemann, P. (1999). Direct measurement of cytosolic calcium and pH in living Chlamydomonas reinhardtii cells. Eur. J. Cell Biol. *78*, 199–208.

Brewer, C.A. (2014). ColorBrewer.

Burda, H., Ballast, L., and Bruns, V. (1988). Cochlea in old world mice and rats (Muridae). Journal of Morphology *198*, 269–285.

Buytaert, J.A.N., and Dirckx, J.J.J. (2007). Design and quantitative resolution measurements of an optical virtual sectioning three-dimensional imaging technique for biomedical specimens, featuring two-micrometer slicing resolution. Journal of Biomedical Optics *12*, 014039.

Buytaert, J.A.N., and Dirckx, J.J.J. (2009). Tomographic imaging of macroscopic biomedical objects in high resolution and three dimensions using orthogonal-plane fluorescence optical sectioning. Applied Optics *48*, 941.

Buytaert, J.A.N., Salih, W.H.M., Dierick, M., Jacobs, P., and Dirckx, J.J.J. (2011). Realistic 3D Computer Model of the Gerbil Middle Ear, Featuring Accurate Morphology of Bone and Soft Tissue Structures. Journal of the Association for Research in Otolaryngology *12*, 681–696.

Buytaert, J.A.N., Johnson, S.B., Dierick, M., Salih, W.H.M., and Santi, P.A. (2013). MicroCT versus sTSLIM 3D Imaging of the Mouse Cochlea. Journal of Histochemistry & Cytochemistry *61*, 382–395.

Cai, Y., Edin, F., Jin, Z., Alexsson, A., Gudjonsson, O., Liu, W., Rask-Andersen, H., Karlsson, M., and Li, H. (2016). Strategy towards independent electrical stimulation from cochlear implants: Guided auditory neuron growth on topographically modified nanocrystalline diamond. Acta Biomater *31*, 211–220.

Camarero, G., Avendano, C., Fernández-Moreno, C., Villar, A., Contreras, J., de Pablo, F., Pichel, J.G., and Varela-Nieto, I. (2001). Delayed Inner Ear Maturation and Neuronal Loss in PostnatalIgf-1-Deficient Mice. The Journal of Neuroscience *21*, 7630.

Cardona, A., Saalfeld, S., Schindelin, J., Arganda-Carreras, I., Preibisch, S., Longair, M., Tomancak, P., Hartenstein, V., and Douglas, R.J. (2012). TrakEM2 Software for Neural Circuit Reconstruction. PLoS ONE *7*, e38011.

Celio, M.R. (1990). Calbindin D-28k and parvalbumin in the rat nervous system. Neuroscience *35*, 375–475.

Ceriani, F., and Mammano, F. (2012). Calcium signaling in the cochlea – Molecular mechanisms and physiopathological implications. Cell Communication and Signaling *10*, 20.

Chung, K., Wallace, J., Kim, S.-Y., Kalyanasundaram, S., Andalman, A.S., Davidson, T.J., Mirzabekov, J.J., Zalocusky, K.A., Mattis, J., Denisin, A.K., et al. (2013). Structural and molecular interrogation of intact biological systems. Nature *497*, 332–337.

Clapham, D.E. (2007). Calcium Signaling. Cell *131*, 1047–1058.

Cobeldick, S. (2018). ColorBrewer: Attractive and Distinctive Colormaps (MATLAB Central File Exchange).

Deisseroth, K. (2015). Optogenetics: 10 years of microbial opsins in neuroscience. Nature Neuroscience *18*, 1213–1225.

Deisseroth, K., and Hegemann, P. (2017). The form and function of channelrhodopsin. Science *357*.

Demarcy, T., Vandersteen, C., Guevara, N., Raffaelli, C., Gnansia, D., Ayache, N., and Delingette, H. (2017). Automated analysis of human cochlea shape variability from segmented μ CT images. Computerized Medical Imaging and Graphics *59*, 1–12.

Di Giovanna, A.P., Tibo, A., Silvestri, L., Müllenbroich, M.C., Costantini, I., Allegra Mascaro, A.L., Sacconi, L., Frasconi, P., and Pavone, F.S. (2018). Whole-Brain Vasculature Reconstruction at the Single Capillary Level. Scientific Reports *8*.

Dieter, A., Duque-Afonso, C.J., Rankovic, V., Jeschke, M., and Moser, T. (2019). Near physiological spectral selectivity of cochlear optogenetics. Nature Communications *10*, 1962.

Dodt, H.-U., Leischner, U., Schierloh, A., Jährling, N., Mauch, C.P., Deininger, K., Deussing, J.M., Eder, M., Zieglgänsberger, W., and Becker, K. (2007). Ultramicroscopy: three-dimensional visualization of neuronal networks in the whole mouse brain. Nature Methods *4*, 331–336.

Dorman, M.F., Loizou, P.C., Fitzke, J., and Tu, Z. (1998). The recognition of sentences in noise by normal-hearing listeners using simulations of cochlear-implant signal processors with 6–20 channels. The Journal of the Acoustical Society of America *104*, 3583–3585.

Douthwright, S., and Sluder, G. (2017). Live Cell Imaging: Assessing the Phototoxicity of 488 and 546 nm Light and Methods to Alleviate it: Phototoxicity Of 488 And 546 Nm Light. Journal of Cellular Physiology *232*, 2461–2468.

Duarte, M.J., Kanumuri, V.V., Landegger, L.D., Tarabichi, O., Sinha, S., Meng, X., Hight, A.E., Kozin, E.D., Stankovic, K.M., Brown, M.C., et al. (2018). Ancestral Adeno-Associated Virus Vector Delivery of Opsins to Spiral Ganglion Neurons: Implications for Optogenetic Cochlear Implants. Molecular Therapy *26*, 1931–1939.

Duran, S.I., Collins, L.M., and Throckmorton, C.S. (2012). Stream segregation on a single electrode as a function of pulse rate in cochlear implant listeners. The Journal of the Acoustical Society of America *132*, 3849–3855.

Eaton-Peabody Lab ImageJ Plugin for Cochlear Frequency Mapping in Whole Mounts (Eaton-Peabody Laboratories).

Eggermont, J.J. (2017). Chapter 5 - Types of Hearing Loss. In Hearing Loss, J.J. Eggermont, ed. (Academic Press), pp. 129–173.

Ehret, G. (1979). Quantitative analysis of nerve fibre densities in the cochlea of the house mouse (Mus musculus). J. Comp. Neurol. *183*, 73–88.

El Mestikawy, S., Wallén-Mackenzie, A., Fortin, G.M., Descarries, L., and Trudeau, L.-E. (2011). From glutamate co-release to vesicular synergy: vesicular glutamate transporters. Nat. Rev. Neurosci *12*, 204–216.

Falk, T., Mai, D., Bensch, R., Çiçek, Ö., Abdulkadir, A., Marrakchi, Y., Böhm, A., Deubner, J., Jäckel, Z., Seiwald, K., et al. (2019). U-Net: deep learning for cell counting, detection, and morphometry. Nature Methods *16*, 67–70.

Fariñas, I., Jones, K.R., Backus, C., Wang, X.-Y., and Reichardt, L.F. (1994). Severe sensory and sympathetic deficits in mice lacking neurotrophin-3. Nature *369*, 658–661.

Fedorov, A., Beichel, R., Kalpathy-Cramer, J., Finet, J., Fillion-Robin, J.-C., Pujol, S., Bauer, C., Jennings, D., Fennessy, F., Sonka, M., et al. (2012). 3D Slicer as an image computing platform for the Quantitative Imaging Network. Magnetic Resonance Imaging *30*, 1323–1341.

Fettiplace, R. (2017). Hair Cell Transduction, Tuning, and Synaptic Transmission in the Mammalian Cochlea. Compr Physiol *7*, 1197–1227.

Fettiplace, R., and Nam, J.-H. (2019). Tonotopy in calcium homeostasis and vulnerability of cochlear hair cells. Hearing Research *376*, 11–21.

Firbank, M., Hiraoka, M., Essenpreis, M., and Delpy, D.T. (1993). Measurement of the optical properties of the skull in the wavelength range 650-950 nm. Physics in Medicine and Biology *38*, 503–510.

Foster, K.W., Saranak, J., Patel, N., Zarilli, G., Okabe, M., Kline, T., and Nakanishi, K. (1984). A rhodopsin is the functional photoreceptor for phototaxis in the unicellular eukaryote Chlamydomonas. Nature *311*, 756–759.

Frank, T., Khimich, D., Neef, A., and Moser, T. (2009). Mechanisms contributing to synaptic Ca2+ signals and their heterogeneity in hair cells. Proc Natl Acad Sci U S A *106*, 4483.

Fremeau, R.T., Burman, J., Qureshi, T., Tran, C.H., Proctor, J., Johnson, J., Zhang, H., Sulzer, D., Copenhagen, D.R., Storm-Mathisen, J., et al. (2002). The identification of vesicular glutamate transporter 3 suggests novel modes of signaling by glutamate. Proc Natl Acad Sci U S A *99*, 14488–14493.

Fritzsch, B., Pan, N., Jahan, I., and Elliott, K.L. (2015). Inner ear development: building a spiral ganglion and an organ of Corti out of unspecified ectoderm. Cell and Tissue Research *361*, 7–24.

Gómez-Nieto, R., Sinex, D.G., C. Horta-Júnior, J. de A., Castellano, O., Herrero-Turrión, J.M., and López, D.E. (2013). A fast cholinergic modulation of the primary acoustic startle circuit in rats. Brain Structure and Function.

Goßler, C., Bierbrauer, C., Moser, R., Kunzer, M., Holc, K., Pletschen, W., Köhler, K., Wagner, J., Schwaerzle, M., Ruther, P., et al. (2014). GaN-based micro-LED arrays on flexible substrates for optical cochlear implants. Journal of Physics D: Applied Physics *47*, 205401.

Gottschalk, W. (1992). Ein Messverfahren zur Bestimmung der optischen Parameter biologischer Gewebe in vitro. University Dissertation. Karlsruhe.

Greenbaum, A., Chan, K.Y., Dobreva, T., Brown, D., Balani, D.H., Boyce, R., Kronenberg, H.M., McBride, H.J., and Gradinaru, V. (2017). Bone CLARITY: Clearing, imaging, and computational analysis of osteoprogenitors within intact bone marrow. Science Translational Medicine *9*, eaah6518.

Greenwood, D.D. (1961). Critical Bandwidth and the Frequency Coordinates of the Basilar Membrane. The Journal of the Acoustical Society of America *33*, 1344–1356.

Greenwood, D.D. (1990). A cochlear frequency-position function for several species--29 years later. J. Acoust. Soc. Am. *87*, 2592–2605.

Greenwood, D.D. (1991). Critical bandwidth and consonance in relation to cochlear frequency-position coordinates. Hearing Research *54*, 164–208.

Gu, X., Chai, R., Guo, L., Dong, B., Li, W., Shu, Y., Huang, X., and Li, H. (2019). Transduction of Adeno-Associated Virus Vectors Targeting Hair Cells and Supporting Cells in the Neonatal Mouse Cochlea. Front. Cell. Neurosci. *13*, 8.

Guinan, J.J. (2012). How are inner hair cells stimulated? Evidence for multiple mechanical drives. Hearing Research *292*, 35–50.

György, B., Sage, C., Indzhykulian, A.A., Scheffer, D.I., Brisson, A.R., Tan, S., Wu, X., Volak, A., Mu, D., Tamvakologos, P.I., et al. (2017). Rescue of Hearing by Gene Delivery to Inner-Ear Hair Cells Using Exosome-Associated AAV. Mol. Ther. *25*, 379–391.

György, B., Meijer, E.J., Ivanchenko, M.V., Tenneson, K., Emond, F., Hanlon, K.S., Indzhykulian, A.A., Volak, A., Karavitaki, K.D., Tamvakologos, P.I., et al. (2019). Gene Transfer with AAV9-PHP.B Rescues Hearing in a Mouse Model of Usher Syndrome 3A and Transduces Hair Cells in a Non-human Primate. Molecular Therapy - Methods & Clinical Development *13*, 1–13.

Hama, H., Kurokawa, H., Kawano, H., Ando, R., Shimogori, T., Noda, H., Fukami, K., Sakaue-Sawano, A., and Miyawaki, A. (2011). Scale: a chemical approach for fluorescence imaging and reconstruction of transparent mouse brain. Nature Neuroscience *14*, 1481–1488.

Hama, H., Hioki, H., Namiki, K., Hoshida, T., Kurokawa, H., Ishidate, F., Kaneko, T., Akagi, T., Saito, T., Saido, T., et al. (2015). ScaleS: an optical clearing palette for biological imaging. Nature Neuroscience *18*, 1518–1529.

Hamers-Casterman, C., Atarhouch, T., Muyldermans, S., Robinson, G., Hammers, C., Songa, E.B., Bendahman, N., and Hammers, R. (1993). Naturally occurring antibodies devoid of light chains. Nature *363*, 446–448.

Hardie, N.A., MacDonald, G., and Rubel, E.W. (2004). A new method for imaging and 3D reconstruction of mammalian cochlea by fluorescent confocal microscopy. Brain Research *1000*, 200–210.

Harrison, J.M., and Irving, R. (1966). Ascending connections of the anterior ventral cochlear nucleus in the rat. The Journal of Comparative Neurology *126*, 51–63.

Haverkamp, S., and Wässle, H. (2004). Characterization of an amacrine cell type of the mammalian retina immunoreactive for vesicular glutamate transporter 3: VGLUT3-Immunoreactive Amacrine Cells. Journal of Comparative Neurology *468*, 251–263.

Heiskala, J., Nissilä, I., Neuvonen, T., Järvenpää, S., and Somersalo, E. (2005). Modeling anisotropic light propagation in a realistic model of the human head. Applied Optics *44*, 2049.

Hernandez, V.H., Gehrt, A., Reuter, K., Jing, Z., Jeschke, M., Mendoza Schulz, A., Hoch, G., Bartels, M., Vogt, G., Garnham, C.W., et al. (2014). Optogenetic stimulation of the auditory pathway. J. Clin. Invest. *124*, 1114–1129.

Hofman, R., Segenhout, J.M., Buytaert, J.A.N., Dirckx, J.J.J., and Wit, H.P. (2008). Morphology and function of Bast's valve: additional insight in its functioning using 3D-reconstruction. Eur Arch Otorhinolaryngol *265*, 153–157.

Hofman, R., Segenhout, J.M., and Wit, H.P. (2009). Three-dimensional reconstruction of the guinea pig inner ear, comparison of OPFOS and light microscopy, applications of 3D reconstruction. Journal of Microscopy *233*, 251–257.

Holcombe, S.A. (2015). inpolyhedron - are points inside a triangulated volume? (MATLAB Central File Exchange).

Hormigo, S., Gómez-Nieto, R., Castellano, O., Herrero-Turrión, M.J., López, D.E., and de Anchieta de Castro e Horta-Júnio, J. (2015). The noradrenergic projection from the locus coeruleus to the cochlear root neurons in rats. Brain Structure and Function *220*, 1477–1496.

Hormigo, S., Gómez-Nieto, R., Sancho, C., Herrero-Turrión, J., Carro, J., López, D.E., and Horta-Júnior, J. de A. de C. e (2017). Morphological correlates of sex differences in acoustic startle response and prepulse inhibition through projections from locus coeruleus to cochlear root neurons. Brain Structure and Function *222*, 3491–3508.

Hormigo, S., López, D.E., Cardoso, A., Zapata, G., Sepúlveda, J., and Castellano, O. (2018). Direct and indirect nigrofugal projections to the nucleus reticularis pontis caudalis mediate in the motor execution of the acoustic startle reflex. Brain Structure and Function *223*, 2733–2751.

Hoshino, T., and Ishioka, K. (1982). Scanning electron microscopy of cochlear blood vessels in the mouse. Archives of Oto-Rhino-Laryngology *237*, 51–57.

Hough, P.V.C. (1962). Method and means for recognizing complex pattterns.

Huisken, J., Swoger, J., Bene, F.D., Wittbrodt, J., and Stelzer, E.H.K. (2004). Optical Sectioning Deep Inside Live Embryos by Selective Plane Illumination Microscopy. Science *305*, 1007–1009.

Jacques, S.L. (2013). Optical properties of biological tissues: a review. Physics in Medicine and Biology *58*, R37–R61.

Jährling, N., Becker, K., and Dodt, H.-U. (2009). 3D-reconstruction of blood vessels by ultramicroscopy. Organogenesis *5*, 227–230.

Jean, P., Lopez de la Morena, D., Michanski, S., Jaime Tobón, L.M., Chakrabarti, R., Picher, M.M., Neef, J., Jung, S., Gültas, M., Maxeiner, S., et al. (2018). The synaptic ribbon is critical for sound encoding at high rates and with temporal precision. Elife *7*.

Jensen, E.B.V., and Gundersen, H.J.G. (1993). The rotator. Journal of Microscopy *170*, 35–44.

Jeschke, M., and Moser, T. (2015). Considering optogenetic stimulation for cochlear implants. Hearing Research *322*, 224–234.

Jiang, H., Wang, X., Zhang, J., Kachelmeier, A., Lopez, I.A., and Shi, X. (2019). Microvascular networks in the area of the auditory peripheral nervous system. Hearing Research *371*, 105–116.

Johnson, S.B., Schmitz, H.M., and Santi, P.A. (2011). TSLIM imaging and a morphometric analysis of the mouse spiral ganglion. Hearing Research *278*, 34–42.

Johnson, S.B., Cureoglu, S., O'Malley, J.T., and Santi, P.A. (2014). Comparison of Traditional Histology and TSLIM Optical Sectioning of Human Temporal Bones: Otology & Neurotology 1.

Kandel, E.R., Schwartz, J.H., and Jessell, T. (2012). Principles of neural science (New York: McGraw-Hill Medical).

Kang, R., Nimmons, G.L., Drennan, W., Longnion, J., Ruffin, C., Nie, K., Won, J.H., Worman, T., Yueh, B., and Rubinstein, J. (2009). Development and validation of the University of Washington Clinical Assessment of Music Perception test. Ear Hear *30*, 411–418.

Kasahara, D., Morita, D., Kosugi, T., Nakagawa, K., Kawamata, J., Higuchi, Y., Matsumura, H., and Mukai, T. (2011). Demonstration of Blue and Green GaN-Based Vertical-Cavity Surface-Emitting Lasers by Current Injection at Room Temperature. Applied Physics Express *4*, 072103.

Kawase, T., and Liberman, M.C. (2004). Spatial organization of the auditory nerve according to spontaneous discharge rate. Journal of Comparative Neurology *319*, 312–318.

Ke, M.-T., Fujimoto, S., and Imai, T. (2013). SeeDB: a simple and morphology-preserving optical clearing agent for neuronal circuit reconstruction. Nature Neuroscience *16*, 1154–1161.

Keller, P.J., and Dodt, H.-U. (2012). Light sheet microscopy of living or cleared specimens. Current Opinion in Neurobiology *22*, 138–143.

Keppeler, D., Merino, R.M., Morena, D.L. de la, Bali, B., Huet, A.T., Gehrt, A., Wrobel, C., Subramanian, S., Dombrowski, T., Wolf, F., et al. (2018). Ultrafast optogenetic stimulation of the auditory pathway by targeting-optimized Chronos. The EMBO Journal *37*, e99649.

Kikinis, R., Pieper, S.D., and Vosburgh, K.G. (2014). 3D Slicer: A Platform for Subject-Specific Image Analysis, Visualization, and Clinical Support. In Intraoperative Imaging and Image-Guided Therapy, F.A. Jolesz, ed. (New York, NY: Springer New York), pp. 277–289.

Kim, M.-A., Ryu, N., Kim, H.-M., Kim, Y.-R., Lee, B., Kwon, T.-J., Bok, J., and Kim, U.-K. (2019). Targeted Gene Delivery into the Mammalian Inner Ear Using Synthetic Serotypes of Adeno-Associated Virus Vectors. Molecular Therapy - Methods & Clinical Development *13*, 197–204.

Kim, S.-Y., Cho, J.H., Murray, E., Bakh, N., Choi, H., Ohn, K., Ruelas, L., Hubbert, A., McCue, M., Vassallo, S.L., et al. (2015). Stochastic electrotransport selectively enhances the transport of highly electromobile molecules. Proceedings of the National Academy of Sciences *112*, E6274–E6283.

Kimura, R.S. (1966). Hairs of the cochlear sensory cells and their attachment to the tectorial membrane. Acta Otolaryngol. *61*, 55–72.

Klapoetke, N.C., Murata, Y., Kim, S.S., Pulver, S.R., Birdsey-Benson, A., Cho, Y.K., Morimoto, T.K., Chuong, A.S., Carpenter, E.J., Tian, Z., et al. (2014). Independent optical excitation of distinct neural populations. Nat Meth *11*, 338–346.

Klein, E., Gossler, C., Paul, O., and Ruther, P. (2018). High-density μLED-based Optical Cochlear Implant with Improved Thermomechanical Behavior. Front. Neurosci. *12*.

Klein, E., Kaku, Y., Paul, O., and Ruther, P. (2019). Flexible μLED-based optogenetic tool with integrated μ-lens array and conical concentrators providing light extraction improvements above 80%. IEEE MEMS 632–635.

Kleinlogel, S., Feldbauer, K., Dempski, R.E., Fotis, H., Wood, P.G., Bamann, C., and Bamberg, E. (2011). Ultra light-sensitive and fast neuronal activation with the Ca_2+-permeable channelrhodopsin CatCh. Nat. Neurosci *14*, 513–518.

Konermann, S., Brigham, M.D., Trevino, A.E., Hsu, P.D., Heidenreich, M., Le Cong, Platt, R.J., Scott, D.A., Church, G.M., and Zhang, F. (2013). Optical control of mammalian endogenous transcription and epigenetic states. Nature *500*, 472–476.

Konigsmark, B.W. (1970). Methods for the Counting of Neurons. In Contemporary Research Methods in Neuroanatomy, W.J.H. Nauta, and S.O.E. Ebbesson, eds. (Berlin, Heidelberg: Springer Berlin Heidelberg), pp. 315–340.

Kopecky, B., Santi, P., Johnson, S., Schmitz, H., and Fritzsch, B. (2011). Conditional deletion of N-Myc disrupts neurosensory and non-sensory development of the ear. Developmental Dynamics *240*, 1373–1390.

Kopecky, B., Johnson, S., Schmitz, H., Santi, P., and Fritzsch, B. (2012a). Scanning thin-sheet laser imaging microscopy elucidates details on mouse ear development. Developmental Dynamics *241*, 465–480.

Kopecky, B.J., Duncan, J.S., Elliott, K.L., and Fritzsch, B. (2012b). Three-dimensional reconstructions from optical sections of thick mouse inner ears using confocal microscopy: 3D Reconstructions From Optical Sections. Journal of Microscopy *248*, 292–298.

Korver, A.M.H., Smith, R.J.H., Van Camp, G., Schleiss, M.R., Bitner-Glindzicz, M.A.K., Lustig, L.R., Usami, S., and Boudewyns, A.N. (2017). Congenital hearing loss. Nature Reviews Disease Primers *3*, 16094.

Leake, P.A., and Snyder, R.L. (1989). Topographic organization of the central projections of the spiral ganglion in cats. The Journal of Comparative Neurology *281*, 612–629.

Leake, P.A., Snyder, R.L., and Merzenich, M.M. (1992). Topographic organization of the cochlear spiral ganglion demonstrated by restricted lesions of the anteroventral cochlear nucleus. The Journal of Comparative Neurology *320*, 468–478.

Leake, P.A., Hradek, G.T., Hetherington, A.M., and Stakhovskaya, O. (2011). Brain-Derived Neurotrophic Factor (BDNF) Promotes Cochlear Spiral Ganglion Cell Survival and Function in Deafened, Developing Cats. J Comp Neurol *519*, 1526–1545.

Lee, C. (2015). Expression of Angiogenic Molecules in Cochlear Vasculature. American Journal of Clinical and Experimental Medicine *3*, 279.

LePage, E.L. (2003). The mammalian cochlear map is optimally warped. The Journal of the Acoustical Society of America *114*, 896–906.

Lewit-Bentley, A., and Rety, S. (2000). EF-hand calcium-binding proteins. Curr Opin Struct Biol *10*, 637–643.

Li Duan, M., Bordet, T., Mezzina, M., Kahn, A., and Ulfendahl, M. (2002). Adenoviral and adeno-associated viral vector mediated gene transfer in the guinea pig cochlea: Neuroreport *13*, 1295–1299.

Liberman, M.C. (1982). The cochlear frequency map for the cat: Labeling auditory-nerve fibers of known characteristic frequency. The Journal of the Acoustical Society of America *72*, 1441–1449.

Liebl, D.J., Tessarollo, L., Palko, M.E., and Parada, L.F. (1997). Absence of Sensory Neurons before Target Innervation in Brain-Derived Neurotrophic Factor-, Neurotrophin 3-, and TrkC-Deficient Embryonic Mice. The Journal of Neuroscience *17*, 9113–9121.

Liu, W., and Davis, R.L. (2014). Calretinin and calbindin distribution patterns specify subpopulations of type I and type II spiral ganglion neurons in postnatal murine cochlea: Heterogeneous distribution of calretinin and calbindin in sgn. Journal of Comparative Neurology *522*, 2299–2318.

López, D.E., Merchán, M.A., Bajo, V.M., and Saldaña, E. (1993). The Cochlear Root Neurons in the Rat, Mouse and Gerbil. In The Mammalian Cochlear Nuclei: Organization

and Function, M.A. Merchán, J.M. Juiz, D.A. Godfrey, and E. Mugnaini, eds. (Boston, MA: Springer US), pp. 291–301.

Lue, N., Bewersdorf, J., Lessard, M.D., Badizadegan, K., Dasari, R.R., Feld, M.S., and Popescu, G. (2007). Tissue refractometry using Hilbert phase microscopy. Optics Letters *32*, 3522.

Luebke, A.E., Rova, C., Von Doersten, P.G., and Poulsen, D.J. (2009). Adenoviral and AAV-mediated gene transfer to the inner ear: role of serotype, promoter, and viral load on in vivo and in vitro infection efficiencies. Adv. Otorhinolaryngol *66*, 87–98.

Luikart, B.., Nef, S., Shipman, T., and Parada, L.. (2003). In vivo role of truncated trkb receptors during sensory ganglion neurogenesis. Neuroscience *117*, 847–858.

MacDonald, G.H., and Rubel, E.W. (2008). Three-dimensional imaging of the intact mouse cochlea by fluorescent laser scanning confocal microscopy. Hearing Research *243*, 1–10.

MacDonald, G.H., and Rubel, E.W. (2010). Three-dimensional confocal microscopy of the mammalian inner ear. Audiological Medicine *8*, 120–128.

Mager, T., Wood, P.G., and Bamberg, E. (2017). Optogenetic Control of Ca2+ and Voltage-Dependent Large Conductance (BK) Potassium Channels. Journal of Molecular Biology *429*, 911–921.

Mager, T., Lopez de la Morena, D., Senn, V., Schlotte, J., D Errico, A., Feldbauer, K., Wrobel, C., Jung, S., Bodensiek, K., Rankovic, V., et al. (2018). High frequency neural spiking and auditory signaling by ultrafast red-shifted optogenetics. Nat Commun *9*, 1750.

Maison, S., Liberman, L.D., and Liberman, M.C. (2016). Type II Cochlear Ganglion Neurons Do Not Drive the Olivocochlear Reflex: Re-Examination of the Cochlear Phenotype in Peripherin Knock-Out Mice. ENeuro *3*.

Mann, Z.F., and Kelley, M.W. (2011). Development of tonotopy in the auditory periphery. Hearing Research *276*, 2–15.

Mardinly, A.R., Oldenburg, I.A., Pégard, N.C., Sridharan, S., Lyall, E.H., Chesnov, K., Brohawn, S.G., Waller, L., and Adesnik, H. (2018). Precise multimodal optical control of neural ensemble activity. Nature Neuroscience *21*, 881–893.

Matsuno-Yagi, A., and Mukohata, Y. (1977). Two possible roles of bacteriorhodopsin; a comparative study of strains of Halobacterium halobium differing in pigmentation. Biochemical and Biophysical Research Communications *78*, 237–243.

Mattotti, M., Micholt, L., Braeken, D., and Kovačić, D. (2015). Characterization of spiral ganglion neurons cultured on silicon micro-pillar substrates for new auditory neuro-electronic interfaces. Journal of Neural Engineering *12*, 026001.

Mei, Y., Weng, G.-E., Zhang, B.-P., Liu, J.-P., Hofmann, W., Ying, L.-Y., Zhang, J.-Y., Li, Z.-C., Yang, H., and Kuo, H.-C. (2017). Quantum dot vertical-cavity surface-emitting lasers covering the “green gap”. Light Sci Appl *6*, e16199.

Meyer, A.C., Frank, T., Khimich, D., Hoch, G., Riedel, D., Chapochnikov, N.M., Yarin, Y.M., Harke, B., Hell, S.W., Egner, A., et al. (2009). Tuning of synapse number, structure and function in the cochlea. Nat Neurosci *12*, 444–453.

Mudry, A., and Mills, M. (2013). The Early History of the Cochlear Implant: A RetrospectiveThe Early History of the Cochlear Implant. JAMA Otolaryngology–Head & Neck Surgery *139*, 446–453.

Müller, M. (1991). Developmental changes of frequency representation in the rat cochlea. Hearing Research *56*, 1–7.

Müller, M. (1996). The cochlear place-frequency map of the adult and developing Mongolian gerbil. Hear. Res *94*, 148–156.

Müller, K., Engesser, R., Metzger, S., Schulz, S., Kämpf, M.M., Busacker, M., Steinberg, T., Tomakidi, P., Ehrbar, M., Nagy, F., et al. (2013). A red/far-red light-responsive bi-stable toggle switch to control gene expression in mammalian cells. Nucleic Acids Research *41*, e77–e77.

Müller, M., von Hünerbein, K., Hoidis, S., and Smolders, J.W.T. (2005). A physiological place-frequency map of the cochlea in the CBA/J mouse. Hear. Res *202*, 63–73.

Munguba, G.C., Camp, A.S., Risco, M., Tapia, M.L., Bhattacharya, S.K., and Lee, R.K. (2011). Vesicular Glutamate Transporter 3 in age-dependent optic neuropathy. Mol Vis *17*, 413–419.

Muñoz, T.E., Giberson, R.T., Demaree, R., and Day, J.R. (2004). Microwave-assisted immunostaining: a new approach yields fast and consistent results. Journal of Neuroscience Methods *137*, 133–139.

Muyldermans, S. (2013). Nanobodies: Natural Single-Domain Antibodies. Annual Review of Biochemistry *82*, 775–797.

Myeongsu, N., Kitae, K., and Sunghoe, C. (2019). Rapid and Uniform Staining of Thick Biological Tissues with Antibody using Electro-magnetic Focused Immuno-histoChemistry. (London, United Kingdom), p.

Nagel, G., Ollig, D., Fuhrmann, M., Kateriya, S., Musti, A.M., Bamberg, E., and Hegemann, P. (2002). Channelrhodopsin-1: a light-gated proton channel in green algae. Science *296*, 2395–2398.

Nagel, G., Szellas, T., Huhn, W., Kateriya, S., Adeishvili, N., Berthold, P., Ollig, D., Hegemann, P., and Bamberg, E. (2003). Channelrhodopsin-2, a directly light-gated cation-selective membrane channel. PNAS *100*, 13940–13945.

Niemz, M.H. (2007). Laser-Tissue Interactions: Fundamentals and Applications (Springer).

Nolte, L., Tinne, N., Schulze, J., Heinemann, D., Antonopoulos, G.C., Meyer, H., Nothwang, H.G., Lenarz, T., Heisterkamp, A., Warnecke, A., et al. (2017). Scanning laser optical tomography for in toto imaging of the murine cochlea. PLOS ONE *12*, e0175431.

Ntziachristos, V. (2010). Going deeper than microscopy: the optical imaging frontier in biology. Nature Methods *7*, 603.

O'Donoghue, G. (2013). Cochlear Implants — Science, Serendipity, and Success. New England Journal of Medicine *369*, 1190–1193.

Oesterhelt, D., and Stoeckenius, W. (1971). Rhodopsin-like Protein from the Purple Membrane of *Halobacterium halobium*. Nature New Biology *233*, 149–152.

Oesterhelt, D., and Stoeckenius, W. (1973). Functions of a new photoreceptor membrane. Proc. Natl. Acad. Sci. U.S.A. *70*, 2853–2857.

Ohn, T.-L., Rutherford, M.A., Jing, Z., Jung, S., Duque-Afonso, C.J., Hoch, G., Picher, M.M., Scharinger, A., Strenzke, N., and Moser, T. (2016). Hair cells use active zones with different voltage dependence of Ca2+ influx to decompose sounds into complementary neural codes. PNAS *113*, 201605737.

Okamoto Ugnell, A., and Öberg, P. å. (1997). The optical properties of the cochlear bone. Medical Engineering & Physics *19*, 630–636.

O'Leary, S.J., Richardson, R.R., and McDermott, H.J. (2009). Principles of design and biological approaches for improving the selectivity of cochlear implant electrodes. Journal of Neural Engineering *6*, 055002.

Osen, K.K., Lopez, D.E., Slyngstad, T.A., Ottersen, O.P., and Storm-Mathisen, J. (1991). GABA-like and glycine-like immunoreactivities of the cochlear root nucleus in rat. Journal of Neurocytology *20*, 17–25.

Osmanski, M.S., and Wang, X. (2011). Measurement of absolute auditory thresholds in the common marmoset (Callithrix jacchus). Hear. Res. *277*, 127–133.

Ou, H.C., Harding, G.W., and Bohne, B.A. (2000). An anatomically based frequency–place map for the mouse cochlea. Hear Res *145*, 123–129.

Owens, K., Park, J.H., and Kristian, T. (2013). Utilizing commercial microwave for rapid and effective immunostaining. Journal of Neuroscience Methods *219*, 20–26.

Oxenham, A.J. (2012). Pitch Perception. Journal of Neuroscience *32*, 13335–13338.

Pack, A.K., and Slepecky, N.B. (1995). Cytoskeletal and calcium-binding proteins in the mammalian organ of Corti: cell type-specific proteins displaying longitudinal and radial gradients. Hear. Res. *91*, 119–135.

Pan, N., Jahan, I., Kersigo, J., Kopecky, B., Santi, P., Johnson, S., Schmitz, H., and Fritzsch, B. (2011). Conditional deletion of Atoh1 using Pax2-Cre results in viable mice without differentiated cochlear hair cells that have lost most of the organ of Corti. Hearing Research *275*, 66–80.

Pangrsic, T., Gabrielaitis, M., Michanski, S., Schwaller, B., Wolf, F., Strenzke, N., and Moser, T. (2015). EF-hand protein Ca2+ buffers regulate Ca2+ influx and exocytosis in sensory hair cells. P Natl Acad Sci USA *112*, E1028–E1037.

Park, J.C., Cook, K.C., and Verde, E.A. (1990). Dietary restriction slows the abnormally rapid loss of spiral ganglion neurons in C57BL/6 mice. Hearing Research *48*, 275–279.

Patterson, M.S., Wilson, B.C., Feather, J.W., Burns, D.M., and Pushka, W. (1987). The measurement of dihematoporphyrin ether concentration in tissue by reflectance spectrophotometry. Photochemistry and Photobiology *46*, 337–343.

Peng, T., Balijepalli, A., Gupta, S.K., and LeBrun, T. (2007). Algorithms for On-Line Monitoring of Micro Spheres in an Optical Tweezers-Based Assembly Cell. Journal of Computing and Information Science in Engineering *7*, 330.

Peng, Z., Wang, G.-P., Zeng, R., Guo, J.-Y., Chen, C.-F., and Gong, S.-S. (2013). Temporospatial expression and cellular localization of VGLUT3 in the rat cochlea. Brain Res. *1537*, 100–110.

Periyasamy, V., and Pramanik, M. (2017). Advances in Monte Carlo Simulation for Light Propagation in Tissue. IEEE Reviews in Biomedical Engineering *10*, 122–135.

Perruchini, C., Pecorari, F., Bourgeois, J.-P., Duyckaerts, C., Rougeon, F., and Lafaye, P. (2009). Llama VHH antibody fragments against GFAP: better diffusion in fixed tissues than classical monoclonal antibodies. Acta Neuropathologica *118*, 685–695.

Peters, B.R., Wyss, J., and Manrique, M. (2010). Worldwide trends in bilateral cochlear implantation. Laryngoscope *120 Suppl 2*, S17-44.

Petitpré, C., Wu, H., Sharma, A., Tokarska, A., Fontanet, P., Wang, Y., Helmbacher, F., Yackle, K., Silberberg, G., Hadjab, S., et al. (2018). Neuronal heterogeneity and stereotyped connectivity in the auditory afferent system. Nat Commun *9*, 3691.

Pfingst, B.E., Bowling, S.A., Colesa, D.J., Garadat, S.N., Raphael, Y., Shibata, S.B., Strahl, S.B., Su, G.L., and Zhou, N. (2011). Cochlear infrastructure for electrical hearing. Hearing Research *281*, 65–73.

Pickles, J.O. (2015). Auditory pathways. In Handbook of Clinical Neurology, (Elsevier), pp. 3–25.

Pinyon, J.L., Tadros, S.F., Froud, K.E., Y Wong, A.C., Tompson, I.T., Crawford, E.N., Ko, M., Morris, R., Klugmann, M., and Housley, G.D. (2014). Close-field electroporation gene delivery using the cochlear implant electrode array enhances the bionic ear. Sci Transl Med *6*, 233ra54-233ra54.

Pinyon, J.L., von Jonquieres, G., Crawford, E.N., Duxbury, M., Al Abed, A., Lovell, N.H., Klugmann, M., Wise, A.K., Fallon, J.B., Shepherd, R.K., et al. (2019). Neurotrophin gene augmentation by electrotransfer to improve cochlear implant hearing outcomes. Hearing Research *380*, 137–149.

Pisanello, F., Sileo, L., and De Vittorio, M. (2016). Micro- and Nanotechnologies for Optical Neural Interfaces. Frontiers in Neuroscience *10*.

Pleiner, T., Bates, M., and Görlich, D. (2018). A toolbox of anti–mouse and anti–rabbit IgG secondary nanobodies. The Journal of Cell Biology *217*, 1143–1154.

Polesskaya, O., Baranova, A., Bui, S., Kondratev, N., Kananykhina, E., Nazarenko, O., Shapiro, T., Nardia, F.B., Kornienko, V., Chandhoke, V., et al. (2018). Optogenetic regulation of transcription. BMC Neuroscience *19*.

Postigo, A. (2002). Distinct requirements for TrkB and TrkC signaling in target innervation by sensory neurons. Genes & Development *16*, 633–645.

Power, R.M., and Huisken, J. (2017). A guide to light-sheet fluorescence microscopy for multiscale imaging. Nature Methods *14*, 360–373.

Praetorius, M., Brough, D.E., Hsu, C., Plinkert, P.K., Pfannenstiel, S.C., and Staecker, H. (2009). Adenoviral vectors for improved gene delivery to the inner ear. Hear. Res. *248*, 31–38.

Purves, D., Augustine, G.J., Fitzpatrick, D., Katz, L.C., LaMantia, A.S., McNamara, J.O., and Williams, S.M. (2004). Neuroscience (Sunderland, Mass: Sinauer Associates, Publishers).

Rappaz, B., Marquet, P., Cuche, E., Emery, Y., Depeursinge, C., and Magistretti, P.J. (2005). Measurement of the integral refractive index and dynamic cell morphometry of living cells with digital holographic microscopy. Optics Express *13*, 9361.

Renier, N., Adams, E.L., Kirst, C., Wu, Z., Azevedo, R., Kohl, J., Autry, A.E., Kadiri, L., Umadevi Venkataraju, K., Zhou, Y., et al. (2016). Mapping of Brain Activity by Automated Volume Analysis of Immediate Early Genes. Cell *165*, 1789–1802.

Reuss, S. (2011). Pineal ribbon synapses: regulated by the gland's central innervation. *25*, 9.

Richardson, D.S., and Lichtman, J.W. (2015). Clarifying Tissue Clearing. Cell *162*, 246–257.

Richter, C.-P., and Tan, X. (2014). Photons and neurons. Hear. Res. *311C*, 72–88.

Richter, C.-P., Kumar, G., Webster, E., Banas, S.K., and Whitlon, D.S. (2011). Unbiased counting of neurons in the cochlea of developing gerbils. Hearing Research *278*, 43–51.

Risoud, M., Sircoglou, J., Dedieu, G., Tardivel, M., Vincent, C., and Bonne, N.-X. (2017). Imaging and cell count in cleared intact cochlea in the Mongolian gerbil using laser scanning confocal microscopy. European Annals of Otorhinolaryngology, Head and Neck Diseases *134*, 221–224.

Ross, M.D., and Burkel, W. (1971). Electron microscopic observations of the nucleus, glial dome, and meninges of the rat acoustic nerve. American Journal of Anatomy *130*, 73–91.

Roux, I., Safieddine, S., Nouvian, R., Grati, M., Simmler, M.-C., Bahloul, A., Perfettini, I., Le Gall, M., Rostaing, P., Hamard, G., et al. (2006). Otoferlin, defective in a human deafness form, is essential for exocytosis at the auditory ribbon synapse. Cell *127*, 277–289.

Ruel, J., Emery, S., Nouvian, R., Bersot, T., Amilhon, B., Van Rybroek, J.M., Rebillard, G., Lenoir, M., Eybalin, M., Delprat, B., et al. (2008). Impairment of SLC17A8 Encoding

Vesicular Glutamate Transporter-3, VGLUT3, Underlies Nonsyndromic Deafness DFNA25 and Inner Hair Cell Dysfunction in Null Mice. Am J Hum Genet *83*, 278–292.

Russell, I., and Sellick, P. (1983). Low-frequency characteristics of intracellularly recorded receptor potentials in guinea-pig cochlear hair cells. J Physiol *338*, 179–206.

Sammut, C., and Webb, G.I. (2017). Encyclopedia of Machine Learning and Data Mining (Boston, MA: Springer US).

Santi, P.A., Rapson, I., and Voie, A. (2008). Development of the mouse cochlea database (MCD). Hearing Research *243*, 11–17.

Santi, P.A., Johnson, S.B., Hillenbrand, M., Grandpre, P.Z., Glass, T.J., and Leger, J.R. (2009). Thin-sheet laser imaging microscopy for optical sectioning of thick tissues. BioTechniques *46*, 287–294.

Schettino, A.E., and Lauer, A.M. (2013). The efficiency of design-based stereology in estimating spiral ganglion populations in mice. Hearing Research *304*, 153–158.

Schindelin, J., Arganda-Carreras, I., Frise, E., Kaynig, V., Longair, M., Pietzsch, T., Preibisch, S., Rueden, C., Saalfeld, S., Schmid, B., et al. (2012). Fiji: an open-source platform for biological-image analysis. Nat. Methods *9*, 676–682.

Schmitz, H.M., Johnson, S.B., and Santi, P.A. (2014). Kanamycin-Furosemide Ototoxicity in the Mouse Cochlea: A 3-Dimensional Analysis. Otolaryngology–Head and Neck Surgery *150*, 666–672.

Schröter, T.J., Johnson, S.B., John, K., and Santi, P.A. (2012). Scanning thin-sheet laser imaging microscopy (sTSLIM) with structured illumination and HiLo background rejection. Biomed. Opt. Express, BOE *3*, 170–177.

Schulze, J., Nolte, L., Lyutenski, S., Tinne, N., Heinemann, D., Ripken, T., Willaredt, M.A., Nothwang, H.G., Lenarz, T., and Warnecke, A. (2019). Scanning laser optical tomography in a neuropathic mouse model: Visualization of structural changes. HNO *67*, 69–76.

Seal, R.P., Akil, O., Yi, E., Weber, C.M., Grant, L., Yoo, J., Clause, A., Kandler, K., Noebels, J.L., Glowatzki, E., et al. (2008). Sensorineural Deafness and Seizures in Mice Lacking Vesicular Glutamate Transporter 3. Neuron *57*, 263–275.

Shang, J., Cong, C., Wang, Z., Peimyoo, N., Wu, L., Zou, C., Chen, Y., Chin, X.Y., Wang, J., Soci, C., et al. (2017). Room-temperature 2D semiconductor activated vertical-cavity surface-emitting lasers. Nat Commun *8*, 543.

Sharma, K., Seo, Y.-W., and Yi, E. (2018). Differential Expression of calcium buffering Protein Calretinin in Cochlear Afferent Fibers: A Possible Link to Vulnerability to Traumatic Noise. Experimental Neurobiology *27*, 397.

Shi, X. (2011). Physiopathology of the cochlear microcirculation. Hearing Research *282*, 10–24.

Shrestha, B.R., Chia, C., Wu, L., Kujawa, S.G., Liberman, M.C., and Goodrich, L.V. (2018). Sensory Neuron Diversity in the Inner Ear Is Shaped by Activity. Cell *174*, 1229-1246.e17.

Siedentopf, H., and Zsigmondy, R. (1902). Uber Sichtbarmachung und Größenbestimmung ultramikoskopischer Teilchen, mit besonderer Anwendung auf Goldrubingläser. Annalen Der Physik *315*, 1–39.

Silvestri, L., Costantini, I., Sacconi, L., and Pavone, F.S. (2016). Clearing of fixed tissue: a review from a microscopist's perspective. J Biomed Opt *21*, 081205.

Soleimanzad, H., Gurden, H., and Pain, F. (2017). Optical properties of mice skull bone in the 455- to 705-nm range. Journal of Biomedical Optics *22*, 010503.

Soto-Prior, A., Cluzel, M., Renard, N., Ripoll, C., Lavigne-Rebillard, M., Eybalin, M., and Hamel, C.P. (1995). Molecular cloning and expression of ce parvalbumin in the guinea pig cochlea. Molecular Brain Research 6.

Spalteholz, W. (1911). Über das Durchsichtigmachen von menschlichen und tierischen Präparaten (Leipzig: Hirzel).

Staecker, H., Li, D., O'Malley, B.W., Jr, and Van De Water, T.R. (2001). Gene expression in the mammalian cochlea: a study of multiple vector systems. Acta Otolaryngol. *121*, 157–163.

Steinbrink, J. (2000). Nahinfrarotspektroskopie am Kopf des Erwachsenen mit Pikosekunden-Zeitaufloeosung.

Stöver, T., Yagi, M., and Raphael, Y. (2000). Transduction of the contralateral ear after adenovirus-mediated cochlear gene transfer. Gene Therapy *7*, 377–383.

Suzuki, J., Hashimoto, K., Xiao, R., Vandenberghe, L.H., and Liberman, M.C. (2017). Cochlear gene therapy with ancestral AAV in adult mice: complete transduction of inner hair cells without cochlear dysfunction. Scientific Reports *7*, 45524.

Swoger, J., Verveer, P., Greger, K., Huisken, J., and Stelzer, E.H.K. (2007). Multi-view image fusion improves resolution in three-dimensional microscopy. Optics Express *15*, 8029.

Tandrup, T., Gundersen, H.J.G., and Vedel Jensen, E.B. (1997). The optical rotator. Journal of Microscopy *186*, 108–120.

Taylor, M., Drickamer, K., and Schnaar, R. (2015). Discovery and Classification of Glycan-Binding Proteins. In Varki A, Cummings RD, Esko JD, et Al., Editors. Essentials of Glycobiology [Internet], (Cold Spring Harbor (NY): Cold Spring Harbor Laboratory Press), p.

Thompson, A.C., Wade, S.A., Brown, W.G.A., and Stoddart, P.R. (2012). Modeling of light absorption in tissue during infrared neural stimulation. Journal of Biomedical Optics *17*, 0750021.

Tinling, S.P., Giberson, R.T., and Kullar, R.S. (2004). Microwave exposure increases bone demineralization rate independent of temperature. Journal of Microscopy *215*, 230–235.

Tinne, N., Antonopoulos, G.C., Mohebbi, S., Andrade, J., Nolte, L., Meyer, H., Heisterkamp, A., Majdani, O., and Ripken, T. (2017). Three-dimensional hard and soft tissue imaging of the human cochlea by scanning laser optical tomography (SLOT). PLOS ONE *12*, e0184069.

Tomer, R., Ye, L., Hsueh, B., and Deisseroth, K. (2014). Advanced CLARITY for rapid and high-resolution imaging of intact tissues. Nature Protocols *9*, 1682–1697.

Töpperwien, M. (2018). 3d virtual histology of neuronal tissue by propagation-based x-ray phase-contrast tomography (Göttingen: Göttingen University Press).

Töpperwien, M., van der Meer, F., Stadelmann, C., and Salditt, T. (2018). Three-dimensional virtual histology of human cerebellum by X-ray phase-contrast tomography. Proceedings of the National Academy of Sciences *115*, 6940–6945.

TracePro (2018). TracePro User´s Manual.

Tsuprun, V., and Santi, P. (1999). Ultrastructure and immunohistochemical identification of the extracellular matrix of the chinchilla cochlea. Hearing Research *129*, 35–49.

Tuchin, V.V. (2015). Tissue Optics: Light Scattering Methods and Instruments for Medical Diagnosis (Society of Photo-Optical Instrumentation Engineers (SPIE)).

Valk, W.L., Wit, H.P., Segenhout, J.M., Dijk, F., van der Want, J.J.L., and Albers, F.W.J. (2005). Morphology of the endolymphatic sac in the guinea pig after an acute endolymphatic hydrops. Hearing Research *202*, 180–187.

Van der Zee, P. (1992). Measurement and modelling of the optical properties of human tissue in the near infrared.

Vo-Dinh, T. (2003). Biomedical Photonics Handbook: Fundamentals, Devices, and Techniques (Boca Raton: CRC Press).

Vogl, C., Panou, I., Yamanbaeva, G., Wichmann, C., Mangosing, S.J., Vilardi, F., Indzhykulian, A.A., Pangršič, T., Santarelli, R., Rodriguez-Ballesteros, M., et al. (2016). Tryptophan-rich basic protein (WRB) mediates insertion of the tail-anchored protein otoferlin and is required for hair cell exocytosis and hearing. EMBO J. e201593565.

Voie, A.H. (2002). Imaging the intact guinea pig tympanic bulla by orthogonal-plane fluorescence optical sectioning microscopy. Hear Res *171*, 119–128.

Voie, A.H., and Spelman, F.A. (1995). Three-dimensional reconstruction of the cochlea from two-dimensional images of optical sections. Computerized Medical Imaging and Graphics *19*, 377–384.

Voie, A.H., Burns, D.H., and Spelman, F.A. (1993). Orthogonal-plane fluorescence optical sectioning: Three-dimensional imaging of macroscopic biological specimens. Journal of Microscopy *170*, 229–236.

Volta, A. (1800). XVII. On the electricity excited by the mere contact of conducting substances of different kinds. In a letter from Mr. Alexander Volta, F. R. S. Professor of

Natural Philosophy in the University of Pavia, to the Rt. Hon. Sir Joseph Banks, Bart. K.B. P. R. S. Philosophical Transactions of the Royal Society of London *90*, 403–431.

Wang, L., Jacques, S.L., and Zheng, L. (1995). MCML--Monte Carlo modeling of light transport in multi-layered tissues. Comput Methods Programs Biomed *47*, 131–146.

Water, T.R.V.D. (2012). Historical Aspects of Inner Ear Anatomy and Biology that Underlie the Design of Hearing and Balance Prosthetic Devices. The Anatomical Record *295*, 1741–1759.

Webster, D.B. (1985). The spiral ganglion and cochlear nuclei of deafness mice. Hearing Research *18*, 19–27.

Weiss, R., Voss, A., and Hemmert, W. (2017). Optogenetic stimulation of the cochlea—critical mechanisms and first models. p.

Weiss, R.S., Voss, A., and Hemmert, W. (2016). Optogenetic stimulation of the cochlea—A review of mechanisms, measurements, and first models. Network: Computation in Neural Systems *27*, 212–236.

Welch, A.J., and van Gemert, M.J.C. (2011). Optical-Thermal Response of Laser-Irradiated Tissue (Springer Netherlands).

West, C.D. (1985). The relationship of the spiral turns of the cochlea and the length of the basilar membrane to the range of audible frequencies in ground dwelling mammals. J. Acoust. Soc. Am. *77*, 1091–1101.

Whitlon, D.S., Ketels, K.V., Coulson, M.T., Williams, T., Grover, M., Edpao, W., and Richter, C.P. (2006). Survival and morphology of auditory neurons in dissociated cultures of newborn mouse spiral ganglion. Neuroscience *138*, 653–662.

WHO (2019). WHO.

Wichmann, C., and Moser, T. (2015). Relating structure and function of inner hair cell ribbon synapses. Cell Tissue Res.

Wilson, B.S., and Dorman, M.F. (2008). Cochlear implants: A remarkable past and a brilliant future. Hearing Research *242*, 3–21.

Wilson, B.S., Tucci, D.L., Merson, M.H., and O'Donoghue, G.M. (2017). Global hearing health care: new findings and perspectives. The Lancet *390*, 2503–2515.

Wrobel, C., Dieter, A., Huet, A., Keppeler, D., Duque-Afonso, C.J., Vogl, C., Hoch, G., Jeschke, M., and Moser, T. (2018). Optogenetic stimulation of cochlear neurons activates the auditory pathway and restores auditory-driven behavior in deaf adult gerbils. Science Translational Medicine *10*, eaao0540.

Wrzeszcz, A., Reuter, G., Nolte, I., Lenarz, T., and Scheper, V. (2013). Spiral ganglion neuron quantification in the guinea pig cochlea using Confocal Laser Scanning Microscopy compared to embedding methods. Hearing Research *306*, 145–155.

Xie, L. (2014). Spherical Hough transform for 3D images (MATLAB Central File Exchange).

Yang, D., Thalmann, I., Thalmann, R., and Simmons, D.D. (2004). Expression of α and β parvalbumin is differentially regulated in the rat organ of corti during development. J. Neurobiol. *58*, 479–492.

Yavari, N., Dam, J.S., Antonsson, J., Wårdell, K., and Andersson-Engels, S. (2005). In vitro measurements of optical properties of porcine brain using a novel compact device. Medical & Biological Engineering & Computing *43*, 658–666.

Ye, Q., Wang, J., Deng, Z.-C., Zhou, W.-Y., Zhang, C.-P., and Tian, J.-G. (2011). Measurement of the complex refractive index of tissue-mimicking phantoms and biotissue by extended differential total reflection method. Journal of Biomedical Optics *16*, 097001.

Yin, H., Kanasty, R.L., Eltoukhy, A.A., Vegas, A.J., Dorkin, J.R., and Anderson, D.G. (2014). Non-viral vectors for gene-based therapy. Nature Reviews Genetics *15*, 541–555.

Yu, F., Hao, S., Yang, B., Zhao, Y., Zhang, W., and Yang, J. (2016). Mild Maternal Iron Deficiency Anemia Induces Hearing Impairment Associated with Reduction of Ribbon Synapse Density and Dysregulation of VGLUT3, Myosin VIIa, and Prestin Expression in Young Guinea Pigs. Neurotoxicity Research *29*, 594–604.

Zagorchev, L., Oses, P., Zhuang, Z.W., Moodie, K., Mulligan-Kehoe, M., Simons, M., and Couffinhal, T. (2010). Micro computed tomography for vascular exploration. Journal of Angiogenesis Research *2*, 7.

Zemelman, B.V., Lee, G.A., Ng, M., and Miesenböck, G. (2002). Selective Photostimulation of Genetically ChARGed Neurons. Neuron *33*, 15–22.

Zeng, F.-G. (2002). Temporal pitch in electric hearing. Hearing Research *174*, 101–106.

Zeng, F.-G., Rebscher, S., Harrison, W.V., Sun, X., and Feng, H. (2008). Cochlear Implants:System Design, Integration and Evaluation. IEEE Rev Biomed Eng *1*, 115–142.

LIST OF FIGURES

LIST OF TABLES

ACKNOWLEDGEMENTS

The work reflected here would have not been possible with the support and help of the following people.

I would like to thank my supervisor Prof. Dr. Tobias Moser, for his supervision and for having gathered around him such a collaborative and supportive team, in a very resourceful environment. I am really thankful for all the support for workshops, course and scientific meeting, for all the mentoring meetings and for his availability (especially when it came to last minute deadlines). I would really thank him for the personal development that I have experienced during our collaboration. In these almost 5 years, I have known myself better and learned to develop my ideas and skills independently, reaching goals very far away from my expertise and my comfort zone. For all of that, I feel well equipped for my upcoming challenges (professional and not) and very thankful of having contributed, at least a little bit, to his team.

I would like also to thank all my committee members for the fruitful and supportive discussion in the advisory meetings. Furthermore, I would like to thank Dr. Camin Dean for all the help and support with the lightsheet microscope. Without her commitment to bring a lightsheet to Göttingen and her first workshop, this thesis would have looked totally different.

I would like to thank Christiane, Sandra and Patricia, for their more than excellent help, without which nothing that occurs in the lab would be possible. I would like to thank their infinite patience - they have taken good care of all of us and specially of the chaotic PhD students.

A special thanks goes to Christian Vogl, for being always available to discuss whatever was crossing my mind in mostly any moment, although across our special comprehension barrier. His support and motivation has meant a lot to me. Don´t forget that La bocallideria will be waiting for you!

Another special thanks goes for David, Lina and Özge. For being present during this long road (outside and inside the lab), for sharing difficult moments and for sharing very good ones. For our breaks in whatever of its form (coffee, tea, chocolate, dinner, etc) and for our totally empty and useless complain jar. Special thanks to Özge for her patience (or sometimes the absence of it) and for being able to share desk with me - our discussions have been certainly critical in many part of this work and have helped to tidy up my ideas.

Thanks also to Cristian Setz and Philippe for having provided laughs and entertainment these last months. Specially to Cristian Setz for our scientific conversation and divagations.

I also would like to thank Kai Bodensiek, for his initial supervision and for sharing with me the effort of developing the optical model. He has been one of the most inspirational and resourceful people that I met on my way, from which I have learned a lot.

I would also like to thank my formers teachers and professors. Maxi Nogales, my biology teacher, who was able to transmit his passion for biology and inspire me, back in the high school days, to develop my research career. My histology professors Bea Almolda, Berta Gonzalez, Bernardo Castellano and all their team. Through their classes and more significantly through my stay in their lab, they were able to transfer me their love for the histology, for the fine details that tissues hide and for the artisan side of science. I had you always in my mind when I was getting mesmerized by those cochlear structures that I was seeing in my experiments and that you were explaining us in those lessons at the medicine faculty. For your inspirational role, thank you both.

I would like to thank my diverse families. The one in Göttingen: for all the moments, cumbia (and no cumbia) parties, for the dinners full of gluttony, for the excursions and trips, for everything. To the one that is spread across the world, with a portion in UK, another one in Tenerife and Madrid, another in Barcelona and New Zealand and let´s see where Judit ends up. For make me feel like home, one where the time does not pass by, whenever we are together.

To my parents and siblings, for their support and the unconditional love. For all the transmitted resilience and encouragement to live and study abroad. For all the cheering-up post packages. Without them, I would not have been able to reach here. Thanks for being always there.

And last, but more importantly, to Pao. I would need probably some more pages to thank you all what I have to, but to keep it sort*, porque eres genial*. For coming to Göttingen, twisting totally your life. For being there always, unconditionally. For your constant fights with my self-esteem. For letting me explain you literally anything that pass by my head (most of them probably totally random). For your comprehension. For all the moments. And for being my pattern, my best friend (and my best flatmate, too). For all of that (and way more), thank you.

"Au moment que le cercle a été ainsi complété, j'ai reçu une secousse dans la tête; et, quelques moments après, (les communications continuant sans aucune interruption,) j'ai commencé à sentir un son, ou plutôt un bruit, dans les oreilles, que je ne saurois bien définir; c'étoit une espèce de craquement à secousse, ou petillement, comme si quelque pâte ou matière tenace bouillonnoit. Ce bruit continua sans relâche, et sans augmentation, tout le terns que le cercle fut complet. La sensation désagréable, et que je craignis dangereuse, de la secousse dans le cerveau, a fait que je n'ai pas repété plusieurs fois cette expérience."

Alessandro Volta

XVII. On the electricity excited by the mere contact of conducting substances of different kinds. 1800
(About the first description of the electric stimulation of the auditory system)